Proceedings of the
15th International Conference on Biomedical Applications of

Electrical Impedance Tomography

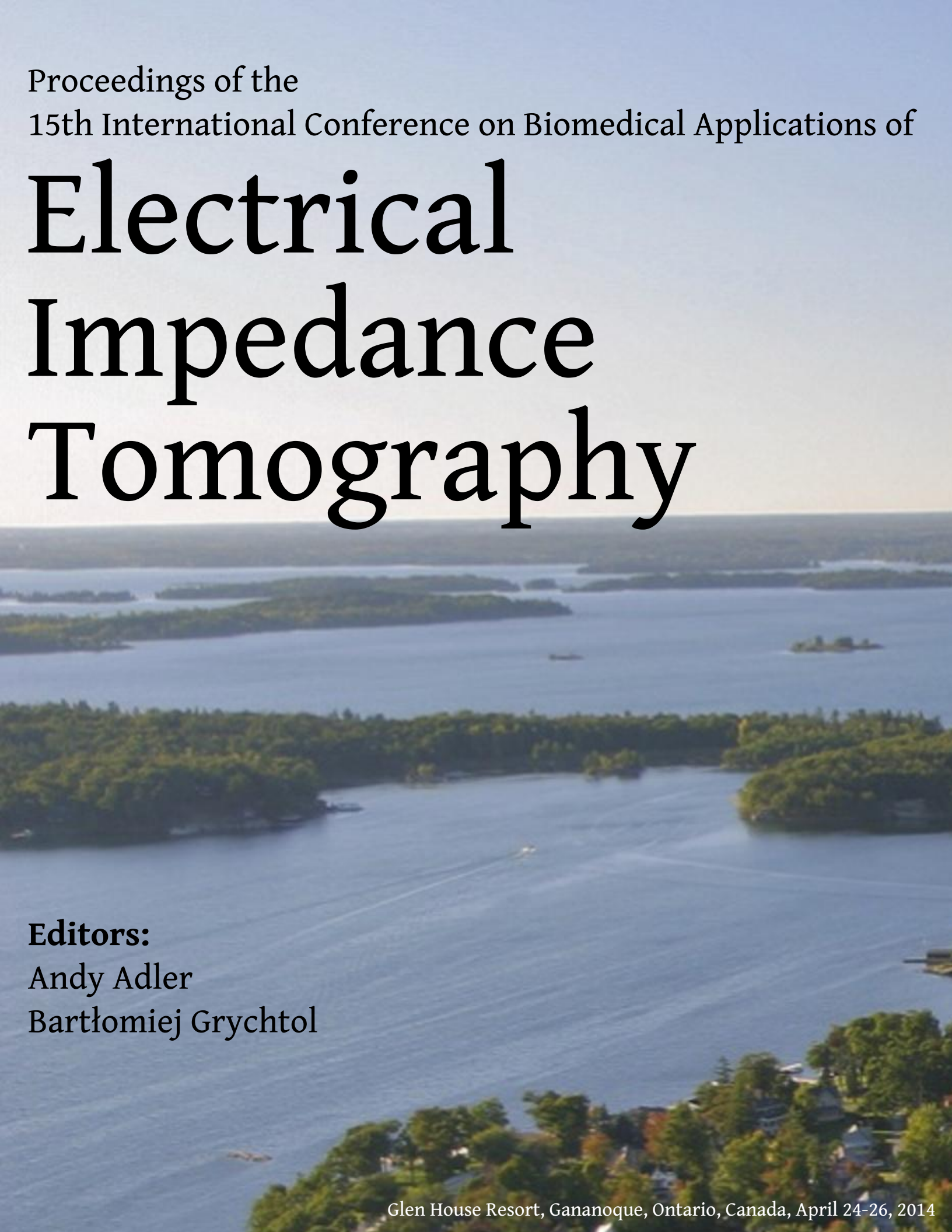

Editors:
Andy Adler
Bartłomiej Grychtol

Glen House Resort, Gananoque, Ontario, Canada, April 24-26, 2014

Proceedings
of the
15th International Conference on
Biomedical Applications of

ELECTRICAL IMPEDANCE TOMOGRAPHY

Edited by Andy Adler and Bartłomiej Grychtol

April 24-26, 2014
Glen House Resort
Gananoque, Ontario
Canada

Carleton UNIVERSITY
swisstom Now I can see.
Dräger
IOP Publishing
Rassettica Testing

Cover design: Bartłomiej Grychtol
Photo credit: ©1000 Islands Photo Art Inc. / Ian Coristine

Printed in Canada

ISBN 978-0-7709-0577-4

Systems and Computer Engineering
Carleton University, 1125 Colonel By Drive
Ottawa, Ontario, K1S 5B6, Canada
adler@sce.carleton.ca
+1 (613) 520-2600

www.eit2014.org

Table of Contents

Applications I

24 April 2014, 8:00 – 9:45

Poster Session I

24 April 2014, 9:45 – 10:00

Reconstruction I

24 April 2014, 10:30 – 12:15

Hardware I

24 April 2014, 13:30 – 15:15

Applications II

24 April 2014, 16:15 – 18:00

Special Lungs Session

25 April 2014, 8:00 – 9:30

Poster Session II

25 April 2014, 9:30 – 9:45

Lung EIT

25 April 2014, 10:45 – 12:00

Chest EIT

25 April 2014, 13:30 – 14:45

Reconstruction II

26 April 2014, 8:00 – 10:00

Applications III

26 April 2014, 10:45 – 12:00

Session 1

Applications I

24 April 2014, 8:00 – 9:45

Welcome to EIT 2014

Andy Adler[1] and Bartłomiej Grychtol[2]

[1]Carleton University, Ottawa, Canada, adler@sce.carleton.ca
[2]Project Group for Automation in Medical Engineering, Fraunhofer IPA, Mannheim, Germany

Abstract: On April 24–26 2014, the 15th International Conference on Biomedical Applications of Electrical Impedance Tomography (EIT 2014) takes place at the Glen House Resort in Gananoque, Canada. Exciting developments are taking place in EIT: developments in hardware, software, and reconstruction algorithms, and new clinical applications and better understanding of the current ones. This paper introduces this fascinating conference.

1 Introduction

Electrical Impedance Tomography (EIT) estimates the distribution of impedance within a body from electrical stimulation and measurement on the body surface. EIT shows significant promise for medical monitoring and imaging with applications to thoracic, brain, breast, abdominal and prostate imaging.

We have all written an introductory paragraph like the previous one, many, many times. And – each time – we try to compress the text, just a little more. Why? We are looking forward to the day when there is no longer a need to explain EIT; when there is no longer the need to call it a promising, "new" technology. Instead, we would like to write, "EIT devices are increasingly used in applications A, B and C, based on evidence of improved patient outcomes and safety [refs D, E, F]". At our 15th International Conference on Biomedical Applications of EIT, we look forward to this day, and review how far along this road we have come.

When discussing EIT's potential, one joke has been often made, referring to the frustrations of a technology that shows much promise, and many challenges: "I wish EIT would either work properly, or fail consistently. That way I can move on with my life." However, joking aside, there are reasons to be enthusiastic about EIT and its potential.

2 Conference

This conference gives an excellent view of the many exciting developments in EIT. Some brief comments are given, but space prevents referring to individual innovations. For this, please see the full proceedings!

- *Scientific interest* in EIT is strong and growing. Within its traditional areas of interest there is increasing interest and appreciation of the unique information it can provide. We see improving collaboration between mathematicians, engineers, physiologists and clinicians; and also interaction with the corresponding geophysical community. Novel image reconstruction and analysis approaches are proposed, incorporating deep mathematical insights and concern for the challenges of EIT data.
- *Commercial devices* are now available. Two companies (both sponsors of the conference) sell EIT devices which are approved for clinical use. This will help address a big limitation which has kept many researchers from using EIT.
- *Medical results* are promising. EIT is now beginning to move beyond the stage of validation to other gold standards, and is being used for prospective interventions, and to detect physiological conditions for which no other technology is available.

3 Discussion

In a recent review[1], a continuous increase in scientific interest in EIT was noted, which was explained by the evidence of a clinical need; this trend has continued (Figure 1).

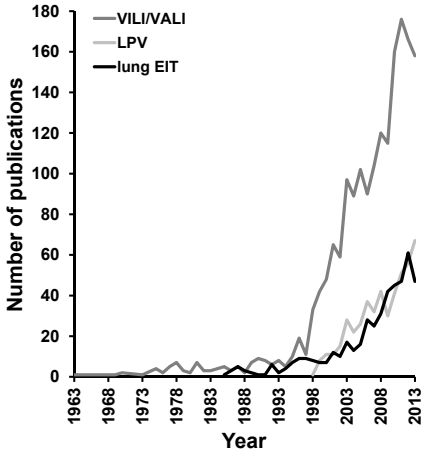

Figure 1: Number of publications vs publication date on VILI/VALI (Ventilator Induced/Associated Lung Injury), LPV (Lung Protective Ventilation) and lung EIT published in peer-reviewed journals. (Image credit: Inéz Frerichs; Source: ISI Web of Knowledge, Thomson Reuters, New York, USA.)

The review offered two suggestions: (1) think about the physiology and pathophysiology ... to provide insights which lead to therapeutic interventions and (2) analyse EIT images in creative ways. When we look at the interesting collection of papers for this conference, we feel optimistic. Many novel insights and creative ways to acquire and analyse EIT are proposed. We will soon say?

EIT is a ~~promising~~ *lifesaving* technology, ...

References

[1] Adler A, Amato MB, Arnold JH, Bayford R, Bodenstein M, Böhm SH, Brown BH, Frerichs I, Stenqvist O, Weiler N, Wolf GK, "Whither lung EIT: where are we, where do we want to go, and what do we need to get there?", *Physiol Meas*, 33:679–694, 2012.

Imaging Epileptic Seizures in a Rat Model using Electric Impedance Tomography and its Clinical Implications

Anna Vongerichten, Gustavo Sato dos Santos, Kirill Aristovich, Andrew McEvoy, Matthew Walker, David Holder

Dept. Medical Physics and Bioengineering and Inst. of Neurology, University College London, UK

Abstract: The potential of Electric Impedance Tomography (EIT) for localising seizure foci was examined in a rat model of epilepsy. The known seizure focus was successfully imaged, which appeared as a transient (~10 ms) decrease in impedance during spikes – due to the opening of ion channels, followed by a gradual increase in impedance as cells swelled.

1 Introduction

Epilepsy is the commonest neurological condition which is characterized by recurrent, unpredictable seizures due to synchronized neuronal firing. Of those with chronic epilepsy, 20-30% will not respond to antiepileptic drugs, though many can be treated surgically if a seizure focus can be localized [1]. EIT was previously used in an animal model to image the seizure focus, as accompanying cell swelling increases brain impedance [2]. Changes in impedance due to neuronal activity have been presented before [3]. Here, the first-ever impedance images of both the fast neural response (due to ion channel opening) as well as the slower impedance signal (due to movement of water from extra- to intra-cellular space) during epileptic seizures in rats are presented.

2 Methods

30-channel subdural grid electrodes were implanted over the somatosensory cortex of 9 adult Sprague-Dawley rats under general anaesthesia. Epilepsy was induced by intracortical injection of 4-aminopyridine, picrotoxin or penicillin. Impedance was recorded with a custom-made programmable current source and an amplifier (ActiveTwo AD-box, Biosemi, Netherlands). An AC current with a frequency of 1.7 kHz and 60 μA amplitude was injected between different pairs of the electrode grid. Sample results are shown (Figure 1).

3 Conclusions

Following interictal epileptic spikes, there were reproducible fast neural impedance decreases of -0.26±0.09% (mean±SD, 3562 interictal spikes) 7 ms preceding the peak of the interictal spikes, and impedance increases of 0.57±0.32 %, starting 50 ms after each interictal spike and lasting up to 2 s with no difference between seizure models. For seizures, there were significant peak impedance increases of 2.21±1.16% (201 seizures in total) but no consistent impedance decreases. The impedance changes occurred focally around the injection site and were consistently imaged with a resolution of ~0.4 mm. Impedance measurements could potentially be used to localize seizure onset zones and track seizure spread in human epilepsy patients.

References

[1] J. S. Duncan, “Selecting patients for epilepsy surgery: synthesis of data.," Epilepsy Behav., 20:230–232, 2011.

[2] T. Olsson, M. Broberg, K. J. Pope, a Wallace, L. Mackenzie, F. Blomstrand, M. Nilsson, and J. O. Willoughby, “Cell swelling, seizures and spreading depression: an impedance study.," Neuroscience, 140:505–15, 2006.

[3] T. Oh, O. Gilad, A. Ghosh, M. Schuettler, and D. S. Holder, “A novel method for recording neuronal depolarization with recording at 125-825 Hz: implications for imaging fast neural activity in the brain with electrical impedance tomography.," Med. Biol. Eng. Comput., 49:593–604, 2011.

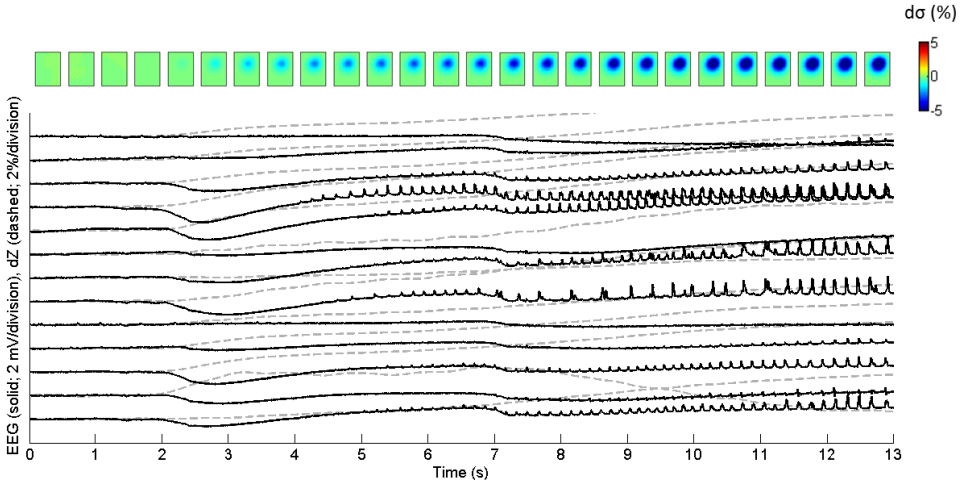

Figure 1: Example of an induced seizure. Solid line: EEG signals, dotted line: corresponding impedance changes. Top row: corresponding EIT images showing focal onset and spread of seizure (depth of slice = 1 mm).

Towards Endoscopic EIT: Ex vivo Assessment of Human Prostates

Shadab Khan[1], Aditya Mahara[1] and Ryan Halter[2]

[1]Thayer School of Engineering at Dartmouth, Hanover, NH, USA, e-mail: Shadab.khan.th@dartmouth.edu

Abstract: Following robotic assisted laparoscopic prostatectomy (RALP), surgical margins are assessed for presence of cancerous tissues. An EIS/EIT based approach to identify benign and malignant tissues was evaluated. Excised prostates were probed using a micro-endoscopic EIT probe, and impedance measurements corresponding to benign and tumorous regions are compared.

1. Introduction

Prostate cancer is one of the most commonly occurring cancers in men. Following RALP, often used for treating organ-confined disease, surgical margins of the excised prostate are microscopically assessed for presence of cancerous tissues. Unfortunately, this assessment is a time-consuming process requiring hours to days to complete. By the time this evaluation is completed, the patient has left the operating room and the surgeon is no longer able to resect additional tissues suspected of harboring cancer.

To this end, we developed an EIT system and microendoscopic EIT probe that we intend to use to intraoperatively evaluate surgical margins.

2. Methods

Hardware setup: A newly developed EIT system was used to collect data [1]. A 9-electrode microendoscopic probe was fabricated to make measurements within a 10mm diameter region. Eight of the 9 electrodes were arranged on the periphery of the probe, and one electrode was placed at the probe center. Impedances were evaluated by driving currents through pairs of electrode in contact with sectioned prostate while induced voltages were recorded and logged from all other electrodes.

Clinical protocol: Experiments were performed at the Dartmouth Hitchcock Medical Center (DHMC), Lebanon, NH under an Institutional Review Board (IRB) approved protocol. Patient consent was obtained prior to undergoing a RALP procedure. Following prostate excision, it is sent in a sealed container to the Pathology lab, where the specimen dimensions are noted. At this point, we have access to the prostate for collecting the EIT data. The EIT system is positioned near to the pathology bench, to minimize probe cable lengths.

For each case, we probe the exterior surface of the prostate at the apex, base, and on the right and left lateral surfaces of the prostate (these represent locations with high incidences of positive surgical margins). The probed site is marked with green ink to allow localization of probing site afterwards. The prostate is then sectioned into ~3mm thick tissue specimens.

Multiple locations on the internal surfaces of the prostate specimens are probed. Specifically, the left and right surfaces of 3-4 sections are selected and probed, and inked pins are inserted through the slices to identify the position and orientation of the probe during the histological assessment of the slides.

3. Results and Conclusion

Measurements taken on the exterior surface of the prostate were grouped according to their location on the prostate, i.e., apex, base and lateral surface. Figure 1(c) shows the averaged magnitude and phase values across the frequency. It can be observed that the impedance measurements vary corresponding to the prostate anatomy ($Z_{lateral} > Z_{apex} > Z_{base}$). Additionally, impedance magnitude and phase spectra shown in Fig. 1(d) indicate that, in general, $Z_{tumor} > Z_{benign}$, which is consistent with the data reported previously [2].

These results obtained from a limited pilot study are very motivating, and we intend to collect more data to statistically evaluate differences in electrical properties between regions and tissues types of the prostate.

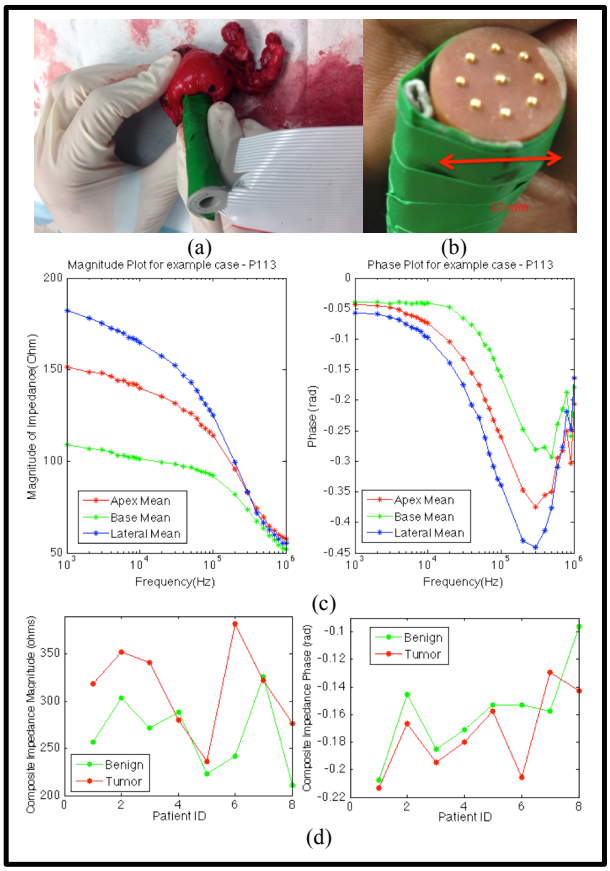

Figure 1: (a) Prostate being probed with a 9-electrode endoscopic probe, (b) Electrode arrangement on the probe head, (c) Magnitude and phase spectra for one of the prostate cases (exterior), (d) Impedance magnitude and phase spectra of internal surface measurements at 10 kHz for benign and tumorous regions.

References

1. S. Khan *et al.,* ICEBI, Germany, 2013.
2. R. Halter *et al., Journal of Urology*, **182**:1600-1607, 2009.

Use of electrical impedance tomography to monitor dehydration treatment of cerebral edema: a clinical study

Feng Fu[1], Bing Li[2], Meng Dai[1], Shijie Hu[2], Xia Li[2], Canhua Xu[1], Bing Wang[2], Bin Yang[1],Xuetao Shi[1],Meng-Xing Tang[3]， Zhou Fei[2]， Xiuzhen Dong[1]

[1]Department of Biomedical Engineering, Fourth Militar yMedical University, Xi'an, China
[2]Neurosurgical Unit of Xijing Hospital, Fourth Military Medical University, Xi'an, China
[3]Department of Bioengineering, Imperial College London, London, United Kingdom

Abstract: In this study EIT was used to monitor brain impedance changes due to variations in cerebral fluid content during dehydration treatment of edema patients. 30 patients with cerebral edema were continuously imaged for two hours after the initiation of dehydration treatment. Results show that overall impedance across the brain increased significantly 5 minutes after dehydration treatment started. And different brain tissues have different reactions towards dehydration

1 Introduction

Cerebral edema is a clinical condition with excess accumulation of fluid in the intracellular or extracellular space of the brain and a common emergency condition in neurology. In the past few decades mannitol dehydration treatment has been proven to be effective for brain edema and has been widely used clinically.

Some initial studies were conducted either with exposed brain or on neonatal brain where skull impedance is less. The group at UCL first demonstrated that the UCLH Mark EIT system could generate reproducible EIT images of epileptic seizures, functional activity, and the phenomenon of spreading depression in anaesthetized experimental animals with a ring of electrodes on exposed brain. We have demonstrated that subarachnoid hemorrhage and intracerebral hemorrhage could be detected by EIT.

In this study EIT is usedf or real-time and non-invasive imaging and monitoring of impedance changes due to variation of cerebral fluid content during dehydration treatment of edema patients.

2 Methods

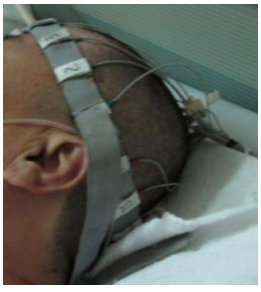

EIT data were measured in real time using an EIT monitoring system (FMMU-EIT5)developed by our group for brain imaging. The system consists of 16 electrodes. Electrodes were placed around the head. Currents were driven in turn through pairs of electrodes opposite each other and voltages on other adjacent electrode pairs were measured. The working frequency of the system ranges from 1 kHz to 190 kHz, the current from 500uA to 1250uA with a measuring accuracy at ±0.01% and the common mode rejection ratio over 80 dB. In this study 1mA-50 kHz alternating current was used.

30 patients with cerebral edema and need of dehydration treatment were included,.

For each patient 0.5g/kg of mannitol solution was administered via intravenous infusion in 20 minutes. Differential images were reconstructed with a reference measurement before mannitol administration.

3 Results

The results show that the overall impedance changes inside the brain increased significantly after mannitol injection. In Figure A, during the injection, the large areas of EIT images became increasingly blue indicating impedance increase in brain, whereas the lesion areas showed much less increase. When the impedance reached the peak after the injection, it remained at the peak for the remainder of the monitoring period. For Figure B, although the results during injection were similar, the impedance changes start to decrease after the end of injection. Two hours after the beginning of the injection, the impedance returned to its initial value.

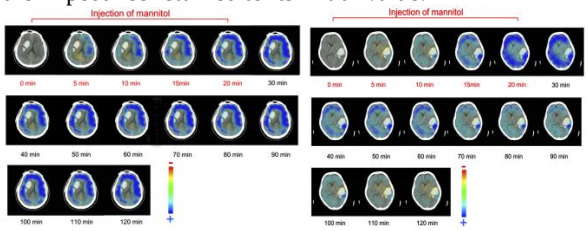

A B

4 Conclusions

The results indicated that EIT was able to reflect the impedance variation induced by loss of brain fluid content during dehydration. The results also showed that the effect of mannitol dehydration treatment was more long-lasting in some patients than in others. Furthermore, our initial results suggest that different brain tissues have different reactions towards dehydration agents---normal brain tissues had more significant dehydration than the diseased tissues.

References

[1] Dai M et al. PLoS One 2013; 8(1):e55020
[2] Sadleir RJ, Tang T. Physiol Meas 2009; 30: 63-79.
[3] D.A. De Luis R. Aller O. Izaola M.C. Terroba G. Cabezas L. Cuellar, Ann Nutr Metab 2006;50:7–10
[4] Manwaring PK, Moodie KL, Hartov A, Manwaring KH, Halter RJ, Anesthesia and Analgesia 2013, 117(4):866-875

Cancer Identification during Breast Surgery Using Electrical Impedance Spectroscopy Analysis

Qifan Wang, Yang Pu, Fei Xiang and Tao Dai

Sealand Technology (Chengdu), Ltd., Chengdu, China. qfwang@eitchina.net

Abstract: In this paper, electrical impedance spectroscopy (EIS) analysis was employed to evaluate the dielectric property of breast tissues. The complex impedance was recorded by a bio-impedance meter in the frequency range of 3 kHz to 1000 kHz. Non-linear Least squares regression was implemented to fit the measured data into Cole-Cole model. It was observed that significant differences existed between breast cancer and benign tissues.

1 Introduction

Breast cancer is the most common malignant tumour among women worldwide. It has been discovered that malignant breast tumors have significantly different impedivity than normal tissues [1-3]; therefore electrical impedance spectroscopy analysis has emerged as a promising indicator for breast cancer detection [4-5]. During a breast cancer excision surgery with ambiguous malignance judgment, the result of frozen biopsy during operation is adopted as a vital reference of the final surgery route (mastectomy or Breast-conserving operation). However, the method involves visual inspection and tissue pathology ('frozen sections') and fails to detect 12-25% of cancer during breast surgery, which means inaccurate tumour identifications lead to under- or over- treatments [6]. As the complimentary method of the frozen biopsy, EIS detector has the potential to be adopted as a hand-held real-time device which will undoubtedly facilitate clinical decision and help reduce erroneous decisions. Moreover, understanding the fundamental electrical property of breast tissues is vital important for some non-invasive impedance imaging techniques, such as electrical impedance tomography (EIT). In this paper, EIS analysis was applied to measure the electrical property of breast tissues in order to obtain some valuable *a priori* information for further research.

2 Methods

In vitro breast tissues were collected from 300 women under mastectomy. Tissue specimens identified by biopsy were categorized in three groups: breast cancer (CaB), benign fibro-adenoma (BFib) and non-hyperplastic mammary glandular tissue (MG). The complex impedance was recorded by a bio-impedance meter in the frequency range of 3 kHz to 1000 kHz. Non-linear Least squares regression was implemented to fit the measured data into Cole-Cole model:

$$R^* = R_\infty + \frac{R_0 - R_\infty}{1+(jf/f_c)^\alpha} \quad (1)$$

Three parameters were statistically obtained including characteristic frequency f_c, fractional power α and static/infinite impedance ratio R_0/R_∞.

Student's t-test was applied in this paper, which is appropriate for statistically analysing on small number groups with Gaussian distribution. Moreover, it is one of the standard and popular methods in medical statistics. Up to present, the sample quantity is still quite limited. For one specific sample, the measurement is affected by random noises which satisfy Gaussian distribution. Therefore, *t-test* can be applied to determine if two sets of data are significantly different from each other.

3 Results

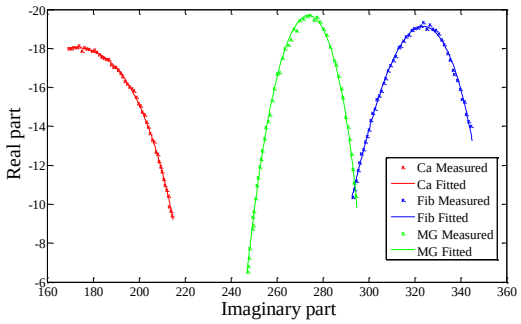

Figure 1: The typical bio-impedance spectroscopes of breast tissues. Spectroscopes are fitted to the Cole-Cole model.

4 Conclusions

In this paper, EIS technique was implemented to analyse the electrical property of breast tissue (Fig. 1). We found that the Cole characteristic frequency f_c is an excellent indicator of the presence of breast cancer since it has much higher value than normal tissues (Tab. 1). *Student's t test* showed that significant difference (p<0.05) existed between CaB and BFib for f_c and R_0/R_∞; while difference was observed between BFib and MG for R_0/R_∞ as well.

References

[1] B. H. Brown, *Lancet* 355: 892–5, 2000
[2] S. Abdul, *Int. J. Gynecol. Cancer* 16: 1823–32, 2006
[3] R. J. Halter, *IEEE Trans. Biomed. Eng.* 54: 1321–7, 2007
[4] J. da Silva, *Med. Biol. Eng. Comput.* 38: 26–30, 2000
[5] R. J. Halter, *Physiol. Meas.* 30: S121–S136, 2009
[6] Nguyen FT, *Cancer Res.* 69(22): 8790-8796, 2009

Table 1: The mean average and standard deviation of tissue Cole-Cole parameters

Tissues	f_c (kHz)	α	R_0/R_∞
CaB	209.9 ± 144.6	0.57±0.16	1.80 ± 0.89
BFib	39.8 ± 30.6	0.53 ± 0.12	1.41 ± 0.17
MG	14.3±14.8	0.54±0.11	1.47±0.28

Wearable sensors for patient-specific boundary shape estimation

Andrew Tizzard[1] Joo Moy Khor[1] Andreas Demosthenous[2] and Richard Bayford[1]

[1] Middlesex University, London, UK
[2]University College, London, UK

Abstract: It has been shown that accurate boundary form of the forward model is important to minimise artefacts in reconstructed EIT images. This paper presents a proposal for a wearable device based on a network of flexible sensors to evaluate patient-specific boundary form of the forward model for lung EIT. Simulation of approaches using ideal sensors are presented that reconstruct boundaries with low shape error.

1 Introduction

The rapid generation of accurate forward models of subject-specific human thorax for EIT still presents a challenge. Despite the fact that some numerical methods e.g. [1], mechanical methods e.g. [2] and computational methods e.g. [3] have been proposed, these are either computationally demanding or impractical for the pediatric clinical environment.

At present, there is no sensor-net available for dynamic measurement of boundary shape for EIT. Use of line-of-sight measurements for monitoring paediatrics is impractical for continuous monitoring within the ICU.

Conductive bend sensor technology [4] has received considerable attention in health rehabilitation applications with advantages of being low cost, flexible, light, wearable and require simple interfacing circuitry. Bend sensors have been investigated for use in geometry reconstruction [5] but no records have been found for patient-specific model reconstruction.

2 Methods

The proposed boundary shape evaluation system is comprised of a series of bend sensors to measure curvature of boundary section and reconstruct a B-spline curve. Perimeter can be further estimated by the inclusion of a stretch sensor. Work was undertaken to select and calibrate a suitable sensor, test reconstruction algorithms, establish optimum number of bend sensors and validate reconstruction algorithms.

Of the commercially available resistive type bend sensors compared one provided acceptable repeatability and consistent linear resistance-curvature relationship. This was the Abrams Gentile sensor (www.ageinc.com).

A geometric *rotational* transformation algorithm proposed by [5] was modified and used to simulate reconstruction using ideal bend sensors:

$$P_1^i = O_1 + r_1 \quad (1)$$

$$P_1^f = O_1 + \begin{bmatrix} cos(s\kappa_1) & -sin(s\kappa_1) \\ sin(s\kappa_1) & cos(s\kappa_1) \end{bmatrix} \left(P_1^i - O_1\right) \quad (2)$$

$$O_{i+1} = P_i^{final} - \kappa_i / r\kappa_{i+1} \left(P_i^{final} - O_i\right) \quad (3)$$

$$P_{i+1}^f = O_{i+1} + \begin{bmatrix} cos(s\kappa_{i+1}) & -sin(s\kappa_{i+1}) \\ sin(s\kappa_{i+1}) & cos(s\kappa_{i+1}) \end{bmatrix} \left(P_i^f - O_{i+1}\right) \quad (4)$$

Where P^i is the initial point, O, the centre of bend radius, P^f, the final point, s the sensor length and κ_i the curvature.

An alternative algortihm is also proposed where the cumulative sum of subtended angle $s\kappa_i$ is used to evaluate the *derivative* of the curve at each sensor end-point. A degree 2 B-spline is interpolated through these values and the curve is reconstructed by integrating the derivative spline over its length and scaling by the sum of sensor lengths resulting in a degree 3 curve.

In both cases errors can be reduced by evaluating the difference of the sum of angles and 2π rads, dividing by the number of sensors give mean angular error to apply to each angle before reconstruction.

Two approaches to reconstruction were used: the whole curve in one direction (uni), and two halves starting from one point and reconstructing in CW and CCW directions and averaging the two final points (bi).

The rotational algorithm was used to reconstruct an ellipse using 4 to 20 sensors in steps of 2 and the mean error defined as distance of reconstructed points from the true curve to determine if an optimum number of sensors could be found

Both algorithms were used on a B-Spline section from a neonatal CT by calculating mean curvatures over a sensor length and reconstructing. Errors were measured as distances from true parametric point and projected distance to true curve for different numbers of sensors.

3 Results

When the rotational algorithm was used to reconstruct and ellipse using 4 to 20 sensors then mean error ($\bar{\varepsilon}$) vs no. of sensors (n) displayed the relationship $\bar{\varepsilon} \approx \frac{750}{n^3}$ ($R^2 = 0.99$). Using 8 sensors, $\bar{\varepsilon}$ is a little more than 1 mm, 6 sensors almost doubles the error. With the neonate boundary, there was insignificant difference between the uni-directional and bi-directional errors, though this was not so for the 16 sensor reconstruction, where the bi-directional approach showed significant improvements.

The derivative algorithm appears not to yield greater accuracy for 8 sensors, but initial indications are that with 16 sensors there are significant improvements.

4 Conclusions

There are initial indications that the use of bend sensors within a wearable device could provide boundary shape reconstruction. This has been demonstrated using a 2D boundary and further work is required for increasing accuracy and establishing methods for 3D boundary to improve the forward model.

References

[1] Soleimani M et al. *XII Int. Conf. on Electrical Bioimpedance and V Electrical Impedance Tomography* 475-478, 2004
[2] Seydnejad SR, Fahimi H *EMBS1994. Proc.16. IEEE*, 1994
[3] Tang MX et al. *IEEE Trans.Med.Imaging* **21:** 2002
[4] Simone LK, Kamper D G *J.Neuroengineering.Rehabil* **2:** 2005
[5] Starck JR et al. *Med.Eng.Phys.* **21:** 1999

Session 2

Poster Session I

24 April 2014, 9:45 – 10:00

In Vivo Estimation of the Scalp and Skull Conductivity

Taweechai Ouypornkochagorn, Nick Polydorides and Hugh McCann

University of Edinburgh, Edinburgh, UK, t.ouypornkochagorn@sms.ed.ac.uk

Abstract: The scalp and skull conductivities (σ_{sc}, σ_{sk} respectively) are determined from Electrical Impedance Tomography (EIT) data using the Gauss-Newton method (GN). Our best estimates of σ_{sc} and σ_{sk} are 0.58 S/m and 0.008 S/m respectively. It is necessary to use the true head geometry.

1 Introduction

Although many authors have reported in vivo values for σ_{sc} and σ_{sk}, most of them refer only to particular regions of the head. For example, it is reported in [1] that σ_{sc} in a selected region is 0.43 S/m, and in [2-4] that σ_{sk} in various regions is in the range 0.0078-0.0801 S/m. In EIT, where the whole head is modelled, it is typical to set all regions of each tissue to a single conductivity value. Here we determine σ_{sc} and σ_{sk} by comparing experimental EIT data with such a model. Our approach is to fit a geometrically accurate head model having two unknowns, σ_{sc} and σ_{sk}, to a set of real measurements by performing a few iterations of the Gauss-Newton method to regress the measurement into the model. The GN formula to evaluate σ is shown in (1) where σ is $[\sigma_{sc};\sigma_{sk}]$, J is the 2-parameter Jacobian, V_{meas} is the measurement vector, and V_i is the model prediction for σ_i, and i is the iteration index.

$$\sigma_{i+1} = \sigma_i + \left(J^T J\right)^{-1} J^T \left(V_{meas} - V_i\right) \qquad (1)$$

2 Methods

Three measurement trials on a single human subject were carried out on three different dates. EIT measurements were recorded at 100 frames per second with 32 electrodes. Three head models (called Model1, 2, and 3) having 338k, 396k, and 53k elements respectively were used. Model 1, the geometrically accurate head model for the subject, was available from MRI scans. In this model, both isotropic and anisotropic (σ_{radial}: $\sigma_{tangential}$ ratio of 1:10) skull conductivities were implemented for comparison. The sensitivity of the method to various effects was tested and found to be small: by simulation, the dependence of the results on electrode shape and position, and on contact impedance, was found to be small, of order 1%; experimentally, the results obtained from multiple installations on the same subject on different days also varied by about 1%.

By carrying out a large number of simulations with a wide variety of conductivity values for CSF, grey matter and white matter, and studying the resulting correlation with scalp and skull conductivity results, we conclude that there is no significant dependence of our results upon the accuracy of the CSF, grey matter and white matter conductivity values.

Equation (1) was employed to evaluate σ with 15 iterations (both σ are finally converged). The estimated σ_{sc} and σ_{sk} are 0.58 S/m and 0.008 S/m, respectively, for both the isotropic and anisotropic versions of Model1 (see table). Compared to the reported values [1], σ_{sc} is significantly larger, while σ_{sk} is at the low end of the range of previously reported values [2-4]. It should be noted that the σ values determined here are effectively from the whole head, in contrast to the small selected regions used in [1-4]. The surface plot of the error term in our iteration procedure is shown in Fig.1, showing a distinct trough in the region of the preferred values. The dependence on σ_{sc} is weak in the range 0.4-0.8 S/m, while being much more strongly dependent on σ_{sk} in the region 0.008-0.010 S/m.

Table: The evaluated σ (S/m)[1] and prediction relative error[1]

	Model1 (reference)		Model2	Model3
	Isotropic	Anisotropic	Isotropic	Isotropic
σ_{scalp}	0.58±.026	0.58±.026	0.23±.007	0.45±.019
σ_{skull}	.008±.0005	.008±.0005	.017±.0011	.006±.0007
Err.	0.28±.008	0.28±.008	0.32±.005	0.33±.012

[1] The value represents in the format of mean±standard deviation

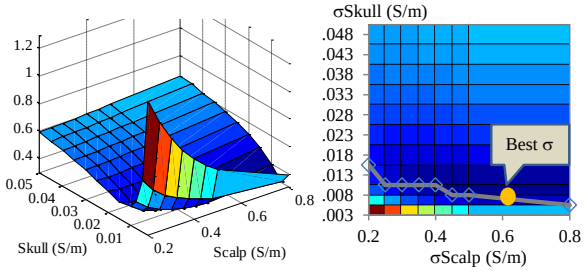

Figure 1: The relative error from the variation of σ_{sc} and σ_{sk}

The evaluated σ values from Model2 and 3, non-subject specific models, are different to Model1 and the errors are higher. The estimation from Model3 is closer to that from Model1, probably since their geometry is quite similar (despite the relatively poor mesh refinement of Model3). Model2 is geometrically different to both of the other models; even when it was scaled to the same size as Model1, the estimated σ_{sc} and σ_{sk} values are 0.29 and 0.0137 S/m, close to the results in the table.

3 Conclusions

We find that the determination of the scalp and skull conductivities by using EIT are strongly dependent on the true head geometry, necessitating the use of subject-specific anatomical scans, by MRI and CT. The results obtained using such a subject-specific model are consistent with values in the literature [5,6].

References

[1] Burger, H. C., Milaan J. B. *Acta Medica Scandinavica CXIV*, 1943
[2] Akhtari, M., et al. *Brain Topography* **14**(3): 151-167, 2002
[3] Hoekema, R., et al. Brain Topography 16(1): 29-38, 2003
[4] Tang, C., et al. *IEEE Trans on Biomedical Engineering*, **55**(9): 2286-2292, 2008
[5] Gonçalves, S. I., et al. *IEEE transactions on Biomedical Engineering*, **50**(6):754:767, 2003
[6] Baysal, U., Haueisen J., *Physiol. Meas*. **25**:737-748, 2004

Real-time monitoring of tissue property in a liver phantom using an internal electrode and weighted frequency difference conductivity during microwave ablation

Hun Wi[1], D T Nguyen[2], Alistair Lee McEwan[2], Tong In Oh[1,*] and Eung Je Woo[1]

[1]Department of Biomedical Engineering, Kyung Hee University, Yongin, Republic of Korea.

[2]The School of Electrical and Information Engineering, The University of Sydney, Australia. * tioh@khu.ac.kr

Abstract: We measured the time difference and weighted frequency difference conductivity images to monitor the changes of temperature and tissue property in a liver phantom due to the microwave ablation. Pixels in regions of interest were compared between conventional boundary surface electrode method and focused configuration with an internal electrode.

1 Introduction

Image-guided thermal therapy has been used for treating of focal metastatic hepatic tumours instead of the standard surgical resection because it is minimally invasive. In order to improve the safety and predict the local recurrence, it requires real-time monitoring method for temperature changes and the tissue property changes *via* successive images. MRI is a good candidate to monitor the internal temperature and property of the tissue with a high resolution. However, it is limited by MR compatible ablation method and cannot confirm the status of tissue after treatment immediately [1]. Ultrasound has a merit for applying ablation and monitoring together, but it required well-trained operator and interpretation [2]. Since the time series of bio-impedance and its spectrum can present temperature changes and tissue property changes together, time-difference and frequency-difference conductivity imaging method may be proposed to monitor them during ablation [3]. In this study, we used an internal electrode and weighted frequency difference conductivity images to improve the sensitivity and estimation for ablated region during microwave ablation.

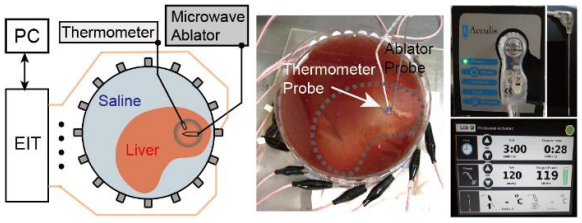

Figure 1: Liver phantom for experiment.

2 Methods

The experimental setup for EIT monitoring with a liver tissue during microwave ablation is shown in Figure 1. Ablation was performed with a frequency of 2.45 GHz (Sulis VpMTA generator, Microsulis Medical Ltd, Denmead, UK) and delivered using a 1.8 mm diameter needle-shaped applicator (Accu2i pMTA applicator, Microsulis Medical Ltd, Denmead, UK). We inserted microwave applicator tip into *ex-vivo* porcine liver (~500g), situated in a cylindrical tank filled with physiological saline (0.9%). 16-channel KHU Mark2.5 EIT system was connected to electrodes surrounding the tank [4]. A thermometer tip was placed beside of applicator tip to record the temperature of heating zone. We applied the ablation as 60W power in 2mins. Data was acquired at 10 and 100 kHz in a scan using dual frequency projections. Time difference and frequency difference images were reconstructed with EIDORS and weighted frequency difference algorithm. We compared the sensitivity and region estimation from the reconstructed images with and without using an internal electrode.

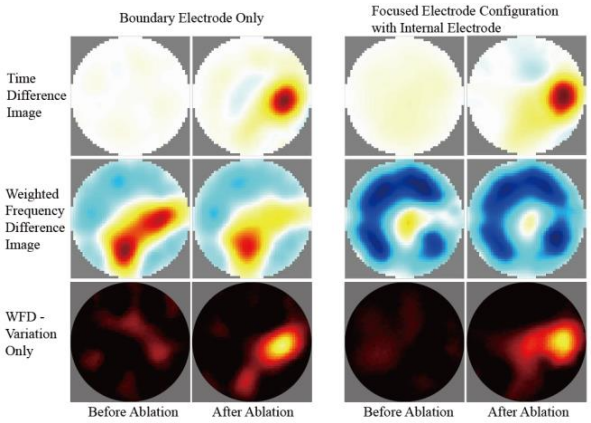

Figure 2: Time difference and weighted frequency difference conductivity images with and without using an internal electrode.

3 Conclusions

We performed the experiment using dual frequency EIT during microwave ablation in *ex-vivo* porcine liver. Time difference image provide conductivity changes due to the temperature changes. On the other hand, weighted frequency difference images showed conductivity change associated with cellular changes better. And when we use focused electrode configuration with an internal electrode, SNR is better in the regions of interest.

References

[1] Goldberg et al *Radiology* "Image-guided tumor ablation: Standardization of terminology and reporting criteria" **235** 728-39, 2005.

[2] Rémi Souchon et al *Ultrasound Med. Biol.* "Monitoring the formation of thermal lesions with heat-induced echo-strain imaging: A feasibility study" 31, 251-9, 2005.

[3] Gersing E. *Ann N Y Acad Sci* "Monitoring temperature-induced changes in tissue during hyperthermia by impedance methods." **873**: 13-20, 1999.

[4] Wi H, Sohal H, McEwan *AL, Oh TI., Biomedical Circuits and Systems, IEEE Transactions on* "Multi-Frequency Electrical Impedance Tomography System With Automatic Self-Calibration for Long-Term Monitoring,", PP(99), 1-1, 2013.

Nanoweb fabric pressure sensor using complex impedance variation

Youssoufa Mohamadou[1], Sol Jee Lee[2], Young Eun Kim[1], Tong In Oh[1], Eung Je Woo[1] and Kap Jin Kim[2]

[1]Department of Biomedical Engineering, Kyung Hee University, Yongin, , Republic of Korea , tioh@khu.ac.kr
[2]Department of Advanced Materials Engineering for Information & Electronics, Kyung Hee University, Yongin, Republic of Korea

Abstract: We developed fabric based pressure sensors with PU or PVDF nanoweb to improve the sensitivity. Sandwiched structure of new fabric sensor with PVDF provided the high sensitivity when using complex impedance variation. It also showed better hysteresis, creep and relaxation property. The new fabric sensor will be used to measure pressure distribution *via* impedance imaging .

1 Introduction

For a gait analysis and pressure sore imaging, there is a demand to measure the pressure distribution on a large area. Plenteous single cell based pressure sensors have been used as an array type. However, this kind of array pressure distribution sensor is required a complex manufacturing process and has a large crosstalk among multiple signals, thick, heavy and too costly. In order to integrate with wearable healthcare monitoring system, we considered conductive fabric materials for costless and flexibility and resistance changes depending on the amount of pressure. Unfortunately, the resistance variation is determined by the intrinsic property of commercial conductive fabric materials and its variation is small.

Recently, we developed the fabric pressure sensor combined with nanoweb to increase the complex impedance variation for pressure change. In the preliminary test, we present the basic properties of the new fabric pressure sensor for a gait analysis and pressure sore imaging.

2 Methods

2.1 Materials

We prepared three types of pressure sensors using commercialized conductive fabric, polyurethane (PU), and polyvinylidene fluoride (PVDF) in Figure 1(a). A conductive fabric of 15×5 cm^2 was cut for the first sensor. The second sensor was made up of a piece of PU nanoweb sandwiched in two pieces of same conductive fabric. The third sensor was the same as the second sensor except of exchanging the PU to PVDF. The PU and the PVDF were prepared by electro-spinning process. The thickness of all sensors were less than 300 μm. Since all of them has a large air space inside, they are good for air permeability.

2.2 Evaluation methods

We evaluated the sensitivity of pressure sensors when applying the 25 gm weight to the sensors up to 300 gm in the measurement configuration as shown in Figure 1(b) and (c). For testing the creep and relaxation of the fabric sensors, 300 gm weight applied at the centre of fabric for 100 seconds and removed it for another 100 seconds, repeatedly. We acquired impedance values for 20 minutes. We tested hysteresis of sensors and timing response in the same configuration.

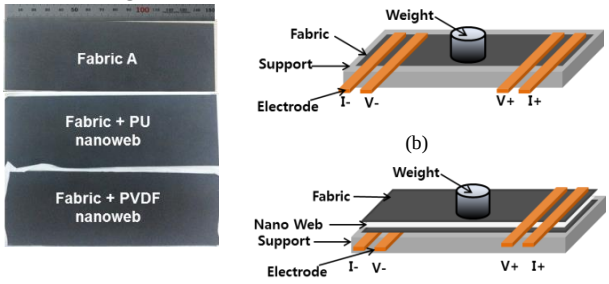

Figure 1: (a) Three kinds of fabric pressure sensors and measurement configuration for impedance of (a) conductive fabric and (b) fabric with nanoweb sensors.

3 Results and conclusions

From the sensitivity evaluation for three different sensors, the variation of impedance in fabric with PVDF nanoweb had the largest changes due to the applied pressure because of large amount of changes in imaginary part. Also, the selection of sensing frequency was important and it provided the characteristic for fabric material and weaving methods. There was a creep and relaxation of fabric sensors when applying pressure continuously and after removing the weight. To reduce them, we applied age forming with high pressure. The new fabric sensor with PVDF produced better hysteresis and timing response than intrinsic commercial conductive fabric sensor. We may produce high sensitive impedance images with the new fabric sensor.

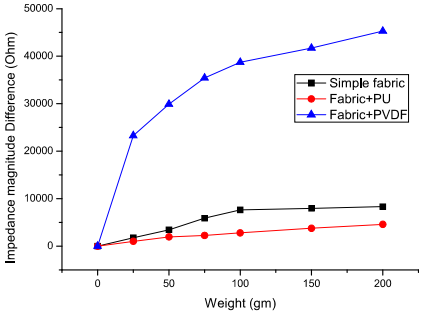

Figure 2: Magnitude of complex impedance variation of three different fabric sensors according to increasing weights.

References

[1] Yangyong W, Tao H, Bo Z, Qiao L, Weijing Y and Xiaoming T *Novel fabric pressure sensors:design, fabrication, and characterization Smart Mater*. Struct. 20, 2011.
[2] Carpi F and De Rossi D. *Electroactive polymer-based devices for e-textiles in biomedicine* IEEE Trans. Inf. Technol. Biomed. 2005.
[3] Yao A and Soleimani M, *A pressure mapping imaging device based on electrical impedance tomography of conductive fabrics*, Sensor Review, 2012

Parametric Reconstruction for Impedance Cystovolumetry

Thomas Schlebusch[1], Steffen Leonhardt[1], Bartłomiej Grychtol[2]

[1]Philips Chair for Medical Information Technology, RWTH Aachen University, Germany, schlebusch@hia.rwth-aachen.de
[2]Department of Medical Physics in Radiology, German Cancer Research Center, Heidelberg, Germany

Abstract: A low-parametric reconstruction method for human bladder volume estimation has been developed and compared to the conventional image-based global impedance method. Main advantages of the new method are conductivity invariant volume estimate and increased accuracy for medium to high bladder volumes.

1 Introduction

In most applications of electrical impedance tomography (EIT), a tomographic image is sought. In some applications, however, the resulting images are processed to estimate a small set of parameters. One example is bladder volume estimation, where the reconstructed image is secondary and an accurate volume estimate is of greater importance. Previously, the linear correlation of global impedance (GI) calculated from reconstructed EIT images has been used to estimate volume [1]. However, this approach conflates changes in bladder volume with varying urine conductivity [2]. In this work, a new low-parametric reconstruction approach for EIT is presented and compared with the established GI method in terms of accuracy, influence of urine conductivity and noise stability.

2 Methods

Simulated EIT data for various bladder volumes and urine conductivities were generated in Matlab based on a simplified, anatomically inspired FEM-model using EIDORS and Netgen. Image reconstruction was carried out with EIDORS adapted for low-parametric reconstruction.

The model consists of a cylinder ø 30 cm containing an eccentrically placed sphere representing the bladder. Two rings of 32 electrodes are placed on the surface. Unit conductivity was assigned to the background. Parametric sweeps for bladder volume from 50 ml to 550 ml, bladder contrast from 1 to 3 and SNR from 10^1 to 10^4 were calculated. Bladder position was a function of radius.

For the GI method, images were reconstructed using the GREIT algorithm [3], and their total value summed (global impedance, GI). A cubic function relating GI and bladder radius was fitted to the results of the sweep at contrast 2 and SNR 10^4 and used for all radius estimations.

Direct low-parametric reconstructions were obtained with EIDORS's iterative Gauss-Newton solver with Tikhonov prior adapted such that the sought solution was limited to two parameters, the Jacobian was approximated with the perturbation method, and the forward solution was calculated using a 3D FEM. The sought parameters were the radius and conductivity contrast (w.r.t known background) of a single spherical target, whose position was a function of the radius.

3 Results

Table 1 shows the relative errors of the GI method (upper value in each cell) and the proposed parametric reconstruction (PR) (lower values). At low bladder volumes, both methods show high errors, but GI outperforms PR. For medium and high volumes, PR shows a clear advantage. Volume estimates based on PR show much lower sensitivity to varying urine conductivity (represented in terms for different image contrasts), but higher sensitivity to noise than those based on GI. While the error of GI is relatively constant at a high level, PR shows excellent results only if little noise is present (SNR 10^3–10^4).

4 Conclusions

Our results indicate that low-parametric reconstruction is a promising approach to bladder volume estimation in the face of unknown urine conductivity. For the purpose of preventing reflux to the kidneys and overflow incontinence, the poor performance at low volumes is not a severe drawback. The high sensitivity to noise – and therefore to such practical difficulties as inexact modelling of abdominal shape, electrode positioning and movement, as well as contact quality – is a drawback which we hope to address in the future by better regularization.

References

[1] Leonhardt S, Cordes A, Plewa H, et al. *Biomed Tech (Berl)* **56**(6):301–307, 2011
[2] Schlebusch T, Cordes A, Pikkemaat R, et al. In *Proc 5th International Workshop on Impedance Spectroscopy*. 2012
[3] Adler A, Arnold JH, Bayford R, et al. *Phys meas* **30**(6):S35–55, 2009

Table 1: Comparision of relative radius errors in % for conventional GI (upper value) and new parametric approach (lower value).

contrast		1				1,5				2				2,5				3			
SNR dB		10	20	30	40	10	20	30	40	10	20	30	40	10	20	30	40	10	20	30	40
bladder volume [ml]	50	93	32	35	35	57	36	37	37	19	40	39	39	87	45	40	40	41	45	41	41
		267	-190	148	81	68	93	302	272	64	-64	518	-151	57	41	33	32	-183	36	43	43
	150	-36	0	0	0	51	13	4	4	18	12	7	8	33	10	11	11	62	18	12	13
		2	-1	-3	0	54	3	0	1	45	1	1	0	44	8	2	2	-11	-2	1	2
	250	14	-4	-10	-10	14	-7	-4	-5	-47	2	0	0	25	4	3	3	29	11	6	6
		-19	-3	0	0	15	-3	0	0	14	-1	0	0	-11	-6	1	0	17	-1	0	0
	350	-23	-14	-15	-15	5	-11	-9	-9	21	-9	-4	-4	7	-1	-1	0	13	6	3	3
		10	4	0	0	0	4	0	0	-22	1	0	0	-15	0	0	0	8	-2	0	0
	450	-10	-18	-19	-19	-4	-9	-12	-12	-11	-4	-7	-7	12	-4	-3	-3	5	1	0	0
		10	1	0	0	-3	-1	0	0	-18	-1	0	0	10	0	0	0	-18	0	0	0
	550	-10	-21	-22	-22	-1	-13	-15	-15	-1	-10	-10	-10	-2	-5	-7	-6	-19	-2	-3	-3
		-14	1	0	0	-5	-1	0	0	1	-1	0	0	-9	-1	0	0	2	1	0	0

Temporal Reconstructions in EIT

Andy Adler[1], Hervé Gagnon[1], Jörg Dittmar[2], Bartłomiej Grychtol[3]

[1]Carleton University, Ottawa, Canada, adler@sce.carleton.ca
[2]Universitätsmedizin Göttingen, Germany
[3]German Cancer Research Center, Heidelberg, Germany

Abstract: EIT shows potential for monitoring fast changing conductivity profiles, such as heart and lung physiology and chemical processes. In such cases, the measurements which constitute an EIT frame are not taken simultaneously. Several approaches have been proposed to interpret such data, but have not been systematically compared. We formulate and compare temporal EIT solvers on simulation data.

1 Introduction

Electrical Impedance Tomography (EIT) has relatively low spatial resolution; however, it has a high temporal resolution, which offers the possibility to capture rapid physiological changes [1]. Thus EIT is used in applications where the underlying conductivity change is rapid compared to the frame rate. In this case, the data within a single EIT frame will not represent the same conductivity distribution. Measurement data $\mathbf{d}_i$ is measured at time t:

$$\mathbf{d}_i = \mathbf{J}_i \mathbf{m}(t) + \mathbf{n} \tag{1}$$

where $\mathbf{J}_i$ is the i^{th} row of the Jacobian (sensitivity) matrix, $\mathbf{m}(t)$ is the conductivity matrix at time t, and $\mathbf{n}$ is additive zero-mean noise, with covariance $\Sigma_{\mathbf{n}}$. Measurements made at nearby points – in both space and time – will "see" a more similar conductivity distribution than those further apart, and this is represented by a space-time covariance matrix, $\Sigma_{\mathbf{m}}$.

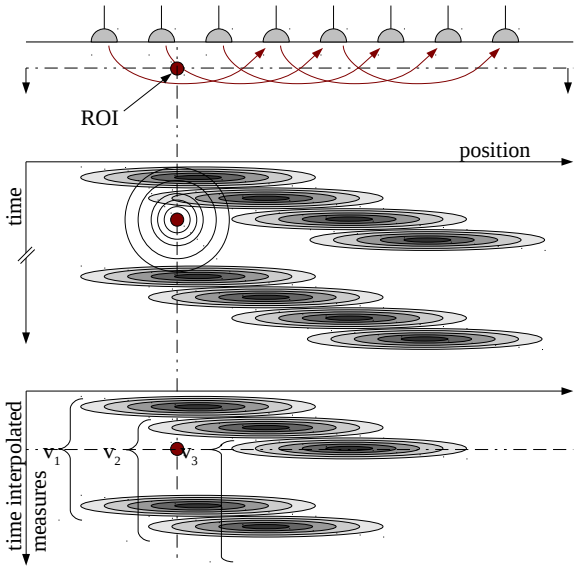

Figure 1: Block diagram of a geophysical EIT system with a temporal effect. *Top:* a ROI in a horizontal plane underneath a series of surface electrodes is imaged. *Middle:* a repeated set of measurements is made, and the sensitivity in space and time is illustrated. Temporal reconstruction uses a covariance matrix in space and time around the ROI (shown). *Bottom:* time interpolation reconstruction first calculates interpolated data (shown) before a traditional reconstruction.

2 Methods

Several approaches to account for temporal effects have been proposed, but have not been systematically compared. Our goal is to develop a framework for such comparison.

Using a Wiener filter formulation, EIT image reconstruction seeks to estimate an image $\hat{\mathbf{m}}$ where

$$\hat{\mathbf{m}} = \Sigma_{\mathbf{m}} \mathbf{T}^t \mathbf{J}^t (\mathbf{J}\mathbf{T}\Sigma_{\mathbf{m}}\mathbf{T}^t\mathbf{J}^t + \Sigma_{\mathbf{n}})\mathbf{F}\mathbf{d} \tag{2}$$

where $\mathbf{T}$ and $\mathbf{F}$ represent the temporal and interpolation filters. Fig. 1 illustrates a simple case of EIT measurements in one spatial dimension and time. Proposed approaches are:

- *Temporal ignorance* (not shown). Assuming that temporal effects are negligable. ($\mathbf{T}$ and $\mathbf{F}$ are both identity)
- *Temporal reconstruction* [2], in which the regularization prior is modelled based on the temporal and spatial effects in $\Sigma_{\mathbf{m}}$. ($\mathbf{T}$ represents the temporal covariance, while $\mathbf{F}$ is identity)
- *Temporal interpolation* [3], in which measurements are interpolated (using Fourier or linear schemes) to the reconstruction time of interest and then reconstructed using an algorithm without temporal information. ($\mathbf{F}$ is the interpolating filter, $\mathbf{T}$ is identity)
- *Kalman filtering* [4] (not shown).

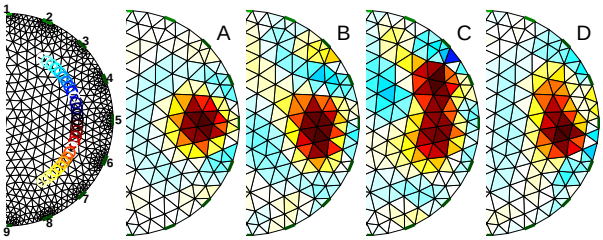

Figure 2: Simulation and Reconstruction images (on circular domain, half shown). *Left*: Simulation matrix, with an object moving from top (blue) to bottom (red) during three acquisition frames; the first acquisition of each frame is marked white; *A:* Reconstruction of a frame of data with the object still at 90° (reference image); *B:* Temporal ignorance; *C:* Linear temporal interpolation; *D:* Temporal reconstruction [2].

3 Discussion

When changes are fast, the EIT measurement frame conflates data from differing distributions. We seek to develop a framework to compare approaches to compensate for this effect. We simulate a relatively fast moving target, and, in this test scenario, images C and D correctly position the target, while B and D have the best spatial localization.

References

[1] Adler A, *et al*, *Physiol Meas*, 33:679–694, 2012.
[2] Adler A, Dai T, Lionheart WRB, *Physiol Meas*, 28:S1–S11, 2007.
[3] Yerworth R, Bayford R, *Physiol Meas*, 34:659–669, 2013.
[4] Vauhkonen M, Karjalainen PA, Kaipio JP, *IEEE T Biomed Eng*, 45:486–493, 1998.

Monitoring Steam-Assisted Gravity Drainage (SAGD) with EIT

Hervé Gagnon[1], Alistair Boyle[1], Michal Okoniewski[2], Andy Adler[1]

[1]Carleton University, Ottawa, Canada
[2]Acceleware Ltd., Calgary, Canada

Abstract: Steam-assisted gravity drainage (SAGD) is a technique that has been developed to efficiently extract bitumen from deep reservoirs. We propose using electrical impedance tomography (EIT) for real-time monitoring of SAGD wells to maintain optimal operating conditions. Several electrode configurations along the pipelines and measurement strategies are presented and compared.

1 Introduction

In Canada, about 80% of bitumen are located in deep reservoirs where only a small fraction has low enough viscosity to be recovered using conventional crude oil pumping techniques [1]. The steam-assisted gravity drainage (SAGD) method has been developed to successfully recover such bitumen [2]. The SAGD method uses continuous injection of high-pressure steam to reduce the viscosity of the bitumen by increasing its temperature and water content (Figure 1). This low-viscosity bitumen drains (via gravity) to a lower pipe where it is collected and pumped to the surface. Several parameters affect SAGD production rate and longevity: spacing between pipes, steam injection pressure, thickness of bitumen layer, soil types above and below the bitumen layer, physical properties of bitumen, and heterogeneity of all these properties. Good monitoring is essential to maintain optimal SAGD operating conditions [3].

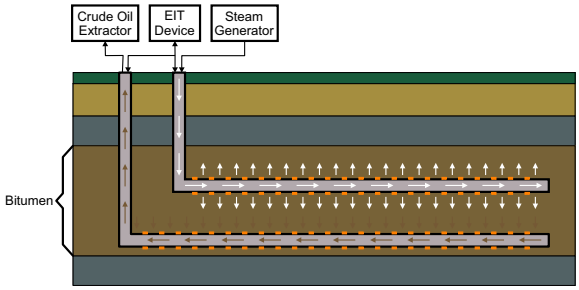

Figure 1: Diagram of steam-assisted gravity drainage. Steam is injected through top pipe while crude oil is recovered through bottom pipe. Proposed EIT sensors are shown as orange rectangles.

To improve SAGD well monitoring, we propose using electrical impedance tomography (EIT) to provide detailed and localized information about the geometry and properties of the soil whose electrical properties are sensitive to composition, water content, temperature, and oil content. Such information would be available in real time as oil is extracted from the reservoir and would be useful to optimize and predict the production rate and longevity of SAGD wells. We propose placing EIT electrodes at regular intervals along both pipelines to image the bitumen reservoir, measure whether conditions are heterogeneous, and how they evolve as oil is extracted and steam is injected. We simulated several electrode configurations and measurement strategies to assess how sensitivity and resolution of EIT images are affected and propose best candidates.

2 Methods

Several 3-D finite element models representing realistic SAGD geometries were built to assess the imaging performance of EIT using five different electrode configurations and three possible measurement and stimulation strategies. The following electrode configurations were considered: 1) ring electrodes uniformly distributed along the pipelines, 2) composite dual ring electrodes where each electrode is subdivided in halves either in the a) vertical or b) horizontal orientations, and 3) composite quad ring electrodes where each electrode is subdivided in quarters either a) orthogonal or b) diagonal to the x, y, z axes.

For each of the above electrode configurations, three measurement strategies were considered: exclusive use of pairs of electrodes parallel (#1) or perpendicular (#2) to the pipelines or a combination of both (#3). Sensitivity images were produced as well as PSF-like images of a moving small target on a horizontal and a vertical axis. For instance, Figure 2 shows four different views of a sensitivity image obtained with quad ring electrodes using a combination of both parallel and perpendicular pairs of electrodes.

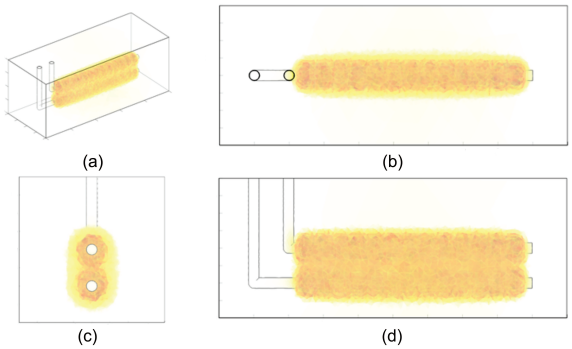

Figure 2: a) 3-D, b) top, c) front, and d) side views of a 3-D image representing areas of maximum sensitivity for a configuration using quad diagonal composite ring electrodes.

3 Discussion

Simpler electrode configurations do not allow distinguishing targets that are located left or right of the pipelines because of the implicit axial symmetry of their geometry. Quad diagonal composite ring electrodes seem to provide the best sensitivity and image resolution among the five tested configurations. Measurement strategies involving pairs of electrodes that are both parallel and perpendicular to the pipelines provide best performance. However, poor signal to noise ratio is to be expected for measurements using pairs of electrodes spanning the gap between the pipes.

References

[1] Rahanama F, Elliott K, Marsh RA, et al. In *Future energy: improved, sustainable and clean options for our planet.* 2008
[2] Chung T, Bae W, Lee J, et al. *Energ Source Part A* **34**:219–226, 2011
[3] Al-Bahlani AM, Babadagli T. *J Pet Sci Eng* **68**:135–150, 2009

Long term scalp EIT recordings for noise modelling to use in intracranial bleeding monitoring

Nir Goren, James Avery and David S Holder
University College London, London, UK

Abstract: Detection of delayed intracranial haemorrhage (ICH) following head trauma or stroke could benefit many patients worldwide [1]. The purpose of this study was to determine the feasibility of monitoring with time difference EIT. This was assessed by addition of noise from actual scalp recording to simulated data for ICH. Reasonably faithful images were produced with realistic recorded drifts.

1 Introduction

Noise in recorded boundary voltages over time, such as drift caused by contact impedance changes during an EIT measurement, can severely degrade the resultant images [2]. As this drift is inevitable in human recordings, its quantification would be an essential part of analysing the data before image reconstruction.

2 Methods

Long term EIT recordings at 2 KHz were taken in one normal human subject with two industry standard EEG electrode types: conventional EEG Ag/AgCl cup electrodes (the current gold standard) and an Easycap EEG recording cap for rapid application. Changes in signal across 3 time bands were calculated: fast (up to 10 seconds, system attributed), medium (up to 10 minutes, subject movement attributed), and slow (over hours, electrodes-skin contact attributed. Samples from recorded noise were added to computer simulated boundary voltages (BV) of intracranial bleeding with volumes of 9-43 ml, to simulate bleeding occurring over different time frames from 10 minutes to 3 hours [3]. Simulated BV with realistic noise component were then used for image reconstruction with Tikhonov regularization algorithm. Resulting images were compared to simulations without noise.

3 Results

3.1 Drifts quantification

Variance was 0.7±1.8, 1.6±3.6 and 15±85.7% (mean ±1SD) across channels of the initial standing BV for the 10 sec, 10 min and 3.5 hour time bands respectively.

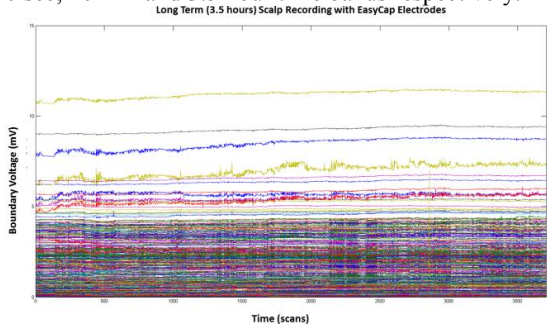

Figure 1: Boundary voltages recorded at 2 KHz over 3.5 hours with EasyCap applied on a healthy subject scalp.

3.2 Imaging

Images were reconstructed for a large extra-dural haematoma (~40ml in volume) located in the right tempo-parietal area for the cases of development over 10, 45, 75, 120 and 190 mins. Images reconstructed with noise were very similar in size, location and shape to the simulated perturbation and to the one reconstructed without noise.

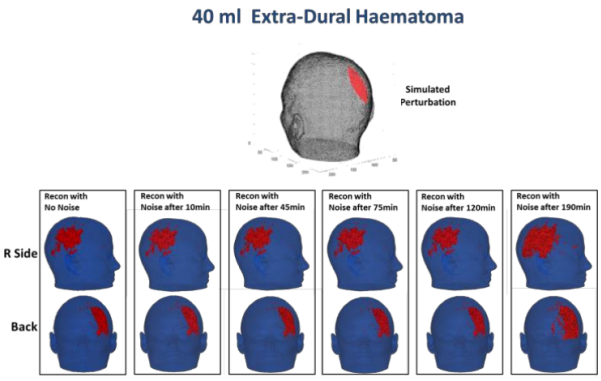

Figure 2: Upper side of demonstrate the original perturbation mesh. Lower part demonstrates reconstructed images of the original perturbation without nose and with realistic noise recorded at 10, 45, 75, 120 and 190 minutes.

4 Conclusions

These initial results suggest that EIT could indeed be used to image intracranial bleeding in head trauma and stroke. Image quality would benefit from more advanced data processing and EIT protocols. This could be a first step toward using EIT as a reliable, accessible, portable and affordable bedside or field monitoring tool in brain trauma and stroke. Work is in progress to collect additional data on multiple subjects to build a more representative sample, determine the drift threshold to enable imaging, and improve the protocol and signal processing.

5 References

[1] Kolias A, M Guilfoyle, A Helmy et al, *Traumatic brain injury in adults*, Practical neurology, 2013
[2] Boone K, Holder DS, *Effect of skin impedance on image quality and variability in electrical impedance tomography: a model study.* Medical & biological engineering & computing, 1996.
[3] Clarke C, Howard M, Rossor M, Shorvon S. Disorders of Consciousness, Intensive care neurology and sleep. A Queen Square Textbook chapter 19, 2009.

A Custom EIT System Based On Off-The-Shelf Equipment

Thomas Dowrick[1], Camille Blochet[1], Nicolas Chaulet[1] and David Holder[1]

[1]Department of Medical Physics, University College London, London, United Kingdom, t.dowrick@ucl.ac.uk

Abstract: The construction of an EIT system using a commercially available current source and EEG amplifier is discussed. The Keithley 6221 current source offers functionality equivalent to that of existing bespoke systems, alongside the ease of use of a commercial system. When combined with a BioSemi EEG amplifier, a full EIT system is produced. Analysis of the signal quality of the source and imaging experiments on a saline tank verify the feasibility of the approach.

1 Introduction

The main components of an EIT system are a current source and a voltage measurement unit. Both are typically constructed from discrete components, or manufactured as custom PCBs/ICs [1-3]. Such approaches work well, especially in instances where the system requirements are well defined. However, such systems can be heavily reliant on the end user, who may not be an engineer, being familiar with the intricacies of the underlying electronics. There can also be significant lead times relating to the design and manufacture of such equipment.

Advantages are available if flexible EIT systems can be built using commercially available equipment. To this end, the suitability of the Keithley 6221 current source for EIT imaging is investigated.

2 Hardware & Results

The Keithley 6221 Current Source is most commonly used for the test and evaluation of semiconductors and nanotechnology devices. However, its ability to accurately source small AC currents (2pA – 100mA) up to a frequency of 100kHz, coupled with a very large output impedance ($10^{14}\Omega$), excellent stability, simple interface and the ability to produce composite waveforms make it highly suited for use in an EIT system.

Key requirements of an EIT current source are low noise and stability across variations in load, current magnitude and frequency The noise magnitude and variations across different current amplitudes and frequencies are shown in Figure 1. It can be seen that the noise level has a maximum of ~0.06%, which is comparable to that of existing EIT systems [4]. The noise is largely invariant with the applied current magnitude, and decreases as the frequency is increased. The large output impedance of the current source gives an extremely stable signal across different loads; variations of approximately one part in a million were seen when the load was varied between 100Ω and 100kΩ.

To test the ability of the current source to produce EIT images, the 6221 was used in conjunction with an EEG system [5] for measurement, to image a Perspex rod in a 32 channel, saline filled tank. A simple switching system, based on the ADG714 and controlled via an Arduino was used to control the injection pattern. The entire system was controlled serially though a MATLAB interface. Figure 2 shows the result of the imaging experiment.

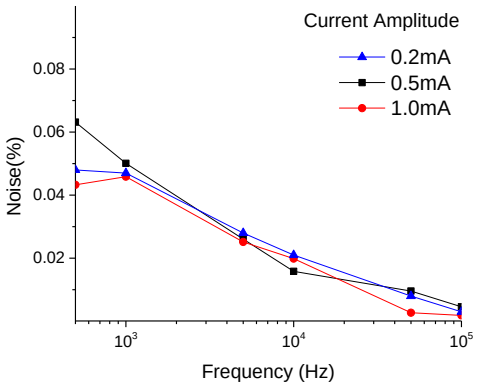

Figure 1: Noise levels, as a percentage of the mean voltage at the frequency of interest, measured across a 1kΩ resistor over 1000 cycles.

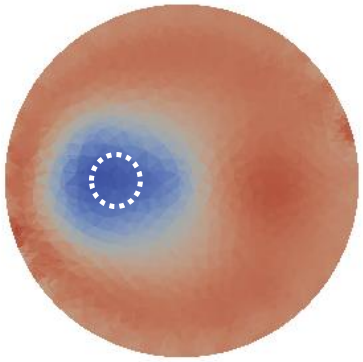

Figure 2: EIT image of a saline tank. The white dashed line indicates the position of the Perspex rod.

3 Conclusions

An EIT system has been presented that uses an off the shelf current source, which offers advantages in terms of flexibility and ease of use when compared to existing systems, while maintaining comparable, or better, functionality. The noise in the system is comparable to existing EIT current sources and the load regulation is excellent. Having established the feasibility of the approach, the system can be used for a broader range of imaging experiments, including more challenging tank imaging, animal studies and human trials.

References

[1] Oh TI, Wi H et al, *Physiol Meas* **32**:pp835-849, 2011
[2] Khalighi M, Vosoughi Vahdat B et al, *in IEEE I2MTC* 2012.
[3] Yerworth RJ, Bayford RH et al, *Physiol Meas* **32**:pp149-158, 2--2
[4] Fabrizi L, McEwan A et al,, *Physiol Meas* 28:S217-36, 2007
[5] http://www.biosemi.com

Segmental Spectral Decomposition as a Time Persistent Method of BioImpedance Spectroscopy Feature Extraction

Isar Nejadgholi[1], Izmail Batkin[1], Miodrag Bolic[1], Andy Adler[2], Shervin Shirmohammadi[1]

[1] School of Electrical Engineering and Computer science, University of Ottawa, Ottawa, Canada

[2]Department of Systems and Computer Engineering, Carleton University, Ottawa, Canada, inejadgh@uottawa.ca

Abstract: BioImpedance Spectroscopy (BIS) have been investigated in many research areas as a method to detect changes in living tissues. However, BIS measurements are known to be hardly reproducible in clinical applications. This article proposes segmental spectral decomposition as a method of extracting reproducible parameters from raw BIS. The efficiency of this method is then compared to conventional Cole-Cole parameter extraction in a classification task.

1 Introduction

BioImpedance Spectroscopy (BIS) is a safe, non-invasive method to explore various changes of the composition or functionality of a living tissue. In spite of widespread range of methods and models introduced by researchers, BIS measurements don't seem to be reproducible enough to be considered as a diagnosis tool [1]. Practically, researchers fit each measured spectrum, $Z(f)$ to Cole-Cole model, using a nonlinear regression algorithm. Four fitting parameters are then used to represent the information content of BIS measurements. These parameters are informative and useful for explaining the physiology of tissues. However, they can be easily affected by experiment setup and condition, which is difficult to control over time, especially from one experiment session to another. In a set of longitudinal BIS data, the information contents related to tissue response at different frequencies are highly correlated, while noise information could be viewed as uncorrelated to tissue's frequency response. Therefore, applying Principal Component Analysis (PCA) in frequency domain could be a promising candidate to cancel the effect of variations of experiment conditions and extract time persistent features from measured spectra. Although PCA has been employed to analyze BIS data in a few specific applications [2], it has never been considered as a general BIS feature extraction method to represent the information content of a set of longitudinal BIS measurements. In this paper, the measured spectra are decomposed and mapped on most significant eigenvectors. Moreover, this decomposition is modified to be delimited in specific frequency ranges to decrease the computational cost. A BIS classification task over different experiment sessions is also investigated to show the advantage of proposed method over Cole-Cole parameter extraction in representing BIS data.

2 Method and Results

We performed a set of measurements using a Solartron 1255 Frequency Response Analyser and 1294 Impedance Interface, with tetra-polar system and frequency range of 5-200 kHz with 5 kHz steps. Four subjects were involved in three different experiment sessions, and their forearm BIS was measured in three different positions: horizontal, vertical pointing downward and vertical pointing upward. Cole-Cole parameters were extracted based on the state-of-the-art method introduced in [3]. For the sake of testing the reproducibility of extracted features in this longitudinal data, each arm position is considered as a class and a classification task is implemented. Different classifiers were tested using 1-leave-out validation method. Using Cole-Cole parameters, best classification accuracy was obtained by a KNN (n=3).

In order to decompose the BIS spectra, the total covariance of spectral data is estimated as sum of the covariance matrices of real and imaginary parts. Eigenvectors are then computed from this covariance matrix. In this experiment, more than 97% of the total variance lies on the first principal component. Therefore, each 80-dimentional vector (real and imaginary in 40 frequencies), is reduced to a 2-dimensional one by mapping real and imaginary parts onto the first eigenvector. In addition, by assessing the coefficients of the first eigenvector for each arm position, we found that different frequencies don't have equal impact on this mapping. So, we delimited the measurements and feature extraction to the frequency range with highest coefficients in the first eigenvector. Restricting the frequency segments decreases the computational cost of analysis which is very important in clinical use. When the above mentioned classifier is fed with the features extracted with proposed method, the classification accuracy improves, which is shown in Table 1. Therefore, this method is extracting the reproducible information from raw data of different experiment sessions more effectively than Cole-Cole method.

3 Conclusions

This paper proposes that segmental spectral decomposition can be considered as an effective feature extractor to overcome the reproducibility issue of BIS measurements. This method is carried out by mapping the measurements on the eigenvectors with highest variance. This mapping is delimited in frequency segments corresponding to highest coefficients of most significant eigenvectors, resulting in a far lower computational cost than nonlinear curve fitting. The proposed method has the potential to be generalized in future works as a general BIS and EIT feature extraction method.

References

[1] Lukaski HC, *European Journal of clinical Nutrition* **67**:S2-S9, 2013
[2] Mughal M, Krivoshei A, et.al, In *CEIT*, 2013.
[3] Yang Y, Ni W, et.al, *Physiol. Meas.* **34**: 1239–1252, 2013

Table 1: Comparing different BIS feature extraction methods in arm position classification task

Feature extraction method	Cole-Cole parameter extraction [3]	Spectral decomposition	Segmental spectral decomposition
Classification Accuracy	75%	87.5%	95.5%

Per Pattern-based Calibration Method for EIT Systems

Shadab Khan[1] and Ryan Halter[1]

[1]Thayer School of Engineering at Dartmouth, Hanover, NH, USA, e-mail: shadab.khan.th@dartmouth.edu

Abstract: A calibration approach has been developed for use with the EIT systems that are significantly influenced by parasitic impedances associated with switches, multiplexers and channel-to-channel coupling. Calibrated data acquired from saline tank experiments is compared with the data obtained from a forward simulation of the experiment.

1. Introduction

EIT systems often use multiplexers and switches to limit the number of signal sources (current or voltage) in a system. While this approach keeps the electronics simple, it introduces significant parasitic impedances to the system, which must be accounted for during calibration.

Previous approaches have used an inter-channel and intra-channel calibration method [1],[2]. This approach works well for systems that either do not rely on multiplexed signal output or use a differential amplifier based approach to measure voltages. However, in single source, single-ended voltage measurement systems, the higher order effects arising out of channel coupling, and increased current shunting, limits the use of these calibration approaches, in which each channel is calibrated individually. Our proposed approach reduces the influence of these coupling effects on the impedance measurements. Specifically, our approach produces a set of calibration factors for *each* frequency and current pattern applied.

2. Methods

The EIT system [4] is first configured to use as many channels as are required for an experiment (i.e. N=8 channels). A wheel-type resistor phantom [3] with N channel connections on the ring is used during calibration. Circuit simulation software (SIMetrix, UK) is used to obtain the voltage at each node in the calibration phantom for each excitation pattern, i.e., each combination of source and sink channels/nodes. These nodal voltages are stored as calibration reference data.

The phantom is then connected to the EIT system, and voltages at each electrode are recorded for each excitation pattern and frequency. Magnitude and phase calibration factors (CF) for each channel, excitation pattern, and signal frequency are calculated as:

$$CF.Mag(i,pat,freq)\angle CF.Phase(i,pat,freq) = \frac{V(i,pat,freq,sim)}{V(i,pat,freq,exp)} \quad \ldots\ldots\ldots\ldots(1)$$

where the *CF.Mag(i,pat,freq)* is the voltmeter magnitude scaling factor and *CF.Phase(i,pat,freq)* is phase correction factor for channel *i,* excitation pattern *pat*, and frequency *freq*. $V(i,pat,freq,sim)$ represents the simulated complex voltage at channel *i* for pattern *pat* and frequency *freq* and $V(i,pat,freq,exp)$ represents the measured voltage at channel *i* for pattern *pat* and frequency *freq* obtained from a phantom experiment. Let $Mag_{\mathrm{V(i,pat,freq,exp)}}$ and $\phi_{\mathrm{V(i,pat,freq,exp)}}$ represent the magnitude and phase respectively, of $V(i,pat,freq,exp)$. Then, the complex calibration factors can be used to obtain calibrated voltage measurements using:

$$V(i,pat,freq,sim)_{calibrated} = Mag_{\mathrm{V(i,pat,freq,exp)}} \times CF.Mag(i,pat,freq) \angle \left[CF.Phase(i,pat,freq) + \phi_{\mathrm{V(I,pat,freq,exp)}}\right] \quad \ldots\ldots\ldots\ldots(2)$$

3. Discussion, Results and Conclusion

Calibration data is obtained for each excitation pattern using a resistor phantom with *all* the channels connected to the phantom. This approach is similar to the inter and intra-channel calibration approach, but takes into account the effects of pattern-dependent channel coupling (increased current shunting, higher order parasitic impedance effects), which is often ignored.

To quantify the accuracy of this calibration approach, we collected data in current drive mode using an 8.5cm diameter tank filled with saline solution having a conductivity of 0.1Sm^{-1}. We compared impedances obtained using calibrated data with impedances computed using a forward simulation of the experimental configuration. Our EIT system [4] was configured to measure 1560 tetrapolar impedances from 16 channels. Scaling factors $\left(SCF = \frac{|Z(sim,10kHz)|}{|Z(exp,10kHz)|}\right)$ were computed to quantify the comparison, where *Z(sim)* represents the complex impedance computed using the forward model at 10kHz. The spread of scaling factors defines how well the calibrated data matches the forward simulation. A narrow spread signifies that all calibrated impedances are close to the expected values (based on a forward model). Of the 1560 tetrapolar impedances recorded, 30 (~2%) of the most extreme SCF values were discarded to limit the range of the histogram. The majority of scaling factors are close to 1.1 (Fig. 1). In addition, measurement patterns corresponding to scaling factors distant from 1.1, had small voltage differences (<20 mV) where noise has a more significant impact. In conclusion, this approach can be used for calibrating EIT systems that have moderate parasitic impedances between channels, and potentially helps to account for issues arising out of channel coupling.

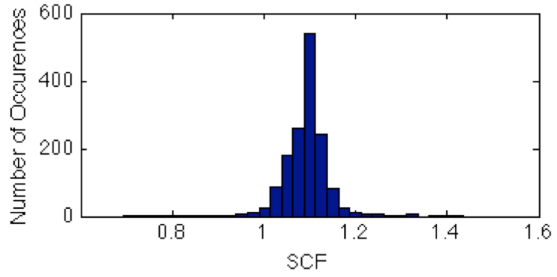

Figure 1: Histogram of SCF with 30 extreme values discarded.

References

1. Oh, T. I., Lee, K. H. *et al.* in *Phys. Meas.* ***28***:1175–88, 2007
2. Halter, R. J., *et al.* in *IEEE Trans. BME* ***55***:650–9, 2008
3. Hahn, G. *et al.* in *Phys. Meas.* **21**: 53–60, 2000
4. S. Khan *et al.*, in *ICEBI,* Germany, 2013

Open Electrical Impedance Tomography (OEIT) File Format

Colin Jones[1], Bartłomiej Grychtol[2], Hervé Gagnon[1], Alistair Boyle[1], Chengbo He[3], Andy Adler[1], Pascal O. Gaggero[4]

[1]Carleton University, Ottawa, Canada, colin.jones@carleton.ca
[2]German Cancer Research Center, Heidelberg, Germany
[3]University of Toronto, Toronto, Canada
[4]Bern University of Applied Sciences, Bienne, Switzerland

Abstract: Electrical impedance tomography (EIT) creates tomographic images from surface electrical stimulation and measurement. Many research and commercial devices have been made, with correspondingly many data formats, which negatively impacts the ability to share data. To address this issue, we have developed the OEIT data format, an XML-based flexible container format for EIT data. We describe its features and structure.

1 Introduction

Electrical impedance tomography (EIT) is a tomographic imaging technique that makes use of electrical currents injected into a body and of the resulting potential field to calculate the spatial distribution of electrical conductivity/impedivity. Over the last decade, EIT has witnessed a dramatic increase in the number of studies produced and commercial implementations[1], leading to an increase in data formats to store EIT, which negatively impacts the ability to share data. We propose a common file structure and XML data description to encapsulate EIT data in order to promote data sharing.

2 File Structure

The OEIT file makes use of the ZIP format with the following directory structure:

/auxiliary Data from auxiliary devices.
/eit Data related to the EIT stimulation and measurement.
/info Descriptive elements of the EIT device, stimulations, and measurements.
/info/sensitive Data of a sensitive nature that may be stripped if the file is shared.
/log Log files related to data acquisition.
/oem Any user-defined data.
/oeit.xml The XML parsing entry point.

While the directory structure is recommended, the XML contains links to all portions of data. Therefore, the only necessary items are the /oeit.xml file for initial parsing and sections required to complete the XML data description.

3 XML Data Description

The oeit.xml file describes the location of all other relevant pieces of information, making use of XInclude[2]:

```
<?xml version="1.0" encoding="UTF-8"?>
<oeit xmlns:xi="http://www.w3.org/2001/XInclude"
      xmlns="http://www.open-eit.org/schema">
    <xi:include href="info/subject.xml"/>
...
```

The recommended location for the data description elements is **/info** with file names and contents as follows:

subject.xml Describes the subject under test.
devices.xml Describes the EIT and other physical devices used during data capture.
electrode_types.xml Describes the physical electrode types used during data capture.
electrodes.xml Describes the logical electrodes used during data capture.
stim_types.xml Describes the types of stimulations used during data capture.
meas_types.xml Describes the types of measurements used during data capture.
frame_types.xml Describes the coupling and temporal arrangements of stimulations and measurements.
streams.xml Describes the internal layout and locations of the data streams in terms of repetitions of frames and describes associated log files.

The XML data description allows a user to describe all fields within a data stream, the stimulations (if any) that produced each field, and the measurement associated with each field (from an example frame_types.xml):

```
...<acquisition duration="369.82us" start="0us">
...     <stim type="CurrentInjection">
            <elec ref="e1" multiplier="1"/>
            <elec ref="e2" multiplier="-1"/>
        </stim>
...
        <meas type="Voltage">
            <elec ref="e3" multiplier="1"/>
            <elec ref="e4" multiplier="-1"/>
        </meas>
...</acquisition>
```

This means the user is free to change the arrangements of stimulations and measurements to best suit their purpose, and consumers of the data can reconstruct the events of data acquisition. Since no assumptions are made as to what is included in the data stream, legacy streams may be described by the XML data description. The complete schema definition can be found online at http://www.open-eit.org/schema.

4 Conclusions

By making no assumptions about data stream contents, providing mechanisms to describe data streams, and containing one entry point, the OEIT file format provides a flexible mechanism to describe EIT acquisitions in a fashion that can be consumed by other parties without *a priori* knowledge of the data acquisition process.

References

[1] Adler, A, MB Amato, JH Arnold, R Bayford, M Bodenstein, SH Boehm, BH Brown, I Frerichs, O Stenqvist, N Weiler, GK Wolf, "Whither lung EIT: Where are we, where do we want to go and what do we need to get there?", Physiological Measurement (2012), 33:679-694.

[2] http://www.w3.org/TR/xinclude/

A High speed, high bandwidth Versatile DAS for breast cancer detection

Jinling Xing, Nan Li, Wang Wei, Mingqian Wang, Danyang Jiang, Hui Xu, Xiaolin Zhang

National University of Defense Technology, Changsha, China, xjl@nudt-esss.com

Abstract: The data acquisition system (DAS) developed aims to get the 3D breast cancer tomography with 8 current injection channels and 117 voltage measurement channels, capable of generating and measuring voltages and currents. By adopting special electrode and careful circuit layout, the initial bandwidth without calibration can reach 5 MHz. Electrical test results show that the system has a SNR greater than 67dB at 5MHz without digital enhancement method.

1 Introduction

Electrical impedance tomography (EIT) is a medical imaging technique which displays the spatial distribution of the complex conductivity inside a body [1]. For previous EIT system [2][3], the main problem is the speed limitation on the data transport path between the tomography computer and DAS, which affects image construction speed and later digital progress. By contrast, the system adopts PXI-Express protocol as the data transport path whose data transferred speed can reach 400MB/s, thus the measurement rate of the systems can easily reach 100 frame/s. In addition, high flexibility can be got by applying the PXI-E structure. The system diagram is illustrated in Fig.1. NI signal data acquisition subsystem consists of a NI-PXI-E case, a versatile DAS card, a multi-channel DAC card and a NI computer controller. The system principle is as follows. First of all, Electrode driving circuits inject current excitation into human body through electrodes, and then the versatile DAS cards get the feedback electrical potential signals and transmit the signals to the NI computer controller. The actual system is illustrated as Fig.1 and Fig.2 respectively.

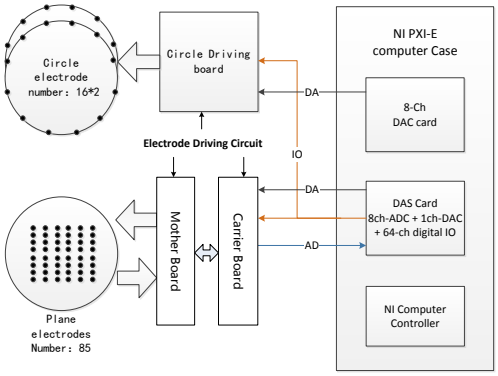

Fig.1 overall design diagram

2 Methods

Versatile DAS card contains features: 8-channel ADC, 1-channel DAC, 64-channel digital I/O ,as shown in Fig.3.

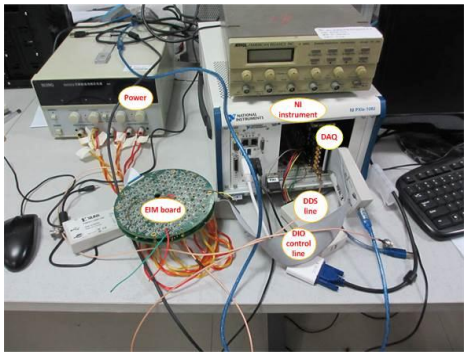

Fig .2 photo of actual DAS system

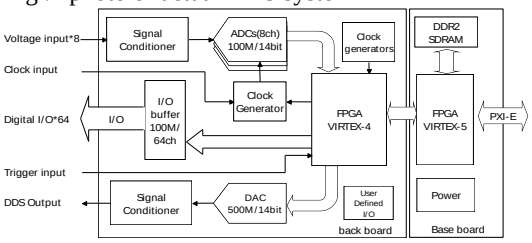

Fig.3 Versatile DAS card diagram

Multichannel DAC card is designed for outputting 8-channel analog signals with minimum voltage precision of 0.12mV, as shown in Fig.5.

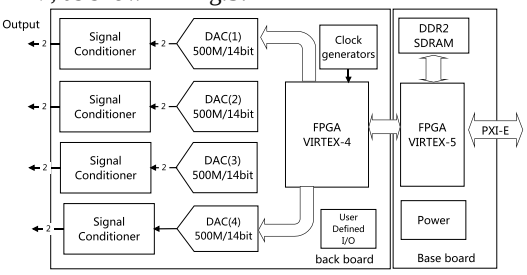

Fig.5 multichannel DAC card diagram

3 Conclusions

The paper presents the design of the data acquisition system briefly. By adopting FPGA as data processing, the system can be easy to be reconfigured, so the system can not only satisfy the need for breast cancer detection, but also can be used for other EIT applications.

References

[1] Holder, D. S. (2005). Electrical impedance tomography-Method, history and applications, Institute of Physics Publishing Bristol and Philadelphia.

[2] MEHRAN G OHARIAN and MANUCHEHRS OLEIMANI, et al. (2008). "A DSP Based Multi-Frequency 3D Electrical Impedance Tomography System." Annals of Biomedical Engineering 36(9): 1594-1603.

[3] J Kourunen, T. S. A. L. and A. L. M. Heikkinen (2009). "Suitability of a PXI platform for an electrical impedance tomography system." MEASUREMENTSCIENCE ANDTECHNOLOGY(20).

The Channel Switch Method of the Cambridge MK4 EIT System

Mingqian Wang, Nan Li, Jinling Xing, Wei Wang, Hui Xu, Xiaolin Zhang

National University of Defence Technology, Changsha, China, wmq@nudt-esss.com

Abstract: With electrical impedance tomography (EIT) system's development, more electrodes is required to get better detection performance. In this paper, we proposed a circuit design to switch channels to different electrodes quickly and stably.

1 Introduction

Various EIT systems have been developed for 3D imaging[1-3].Cambridge MK4 EIT is a 3D medical imaging system for breast cancer detection. It permits visualization of the inner structure of the breast by measuring its impedance distribution.[4] The EIT hardware system is consisted of planar electrode sampling circuit, planar electrode driving circuit, multi-functional sampling card, 64-channel digital IO card, National Instrument(NI) chassis/controller. This system uses current excitation (1mAp-p) and voltage measurement covering frequency from 10kHz to 5MHz.

2 Methods

1. Planar electrode sampling circuit

The upper computer is in charge of the switching control.

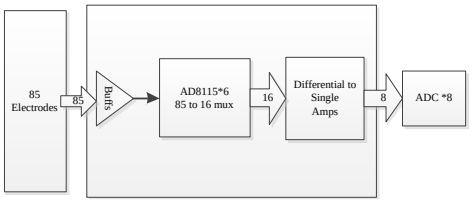

Fig 1. Planar electrode sampling circuit

As show in Fig 1, signals from 85 electrodes can be collected by planar electrode sampling circuit: analog voltage signals enters the DAQ board through a buffer amplifier, the buffered signals transformed into 16-lane voltage signals after a 85×16 switching matrix, it becomes 8-lane analog voltage signals after passing by a differential to single amplifier. Finally, voltage signals are sampled by the 8-channel AD card before the sampled data are transferred to the upper computer to form EIT images.

2. Planar electrode driving circuit

This sub-circuit can complete the switch from a pair of injecting current to 85 electrodes freely. The planar electrodes formed 2×85 switching matrix, in this way, 1-channel voltage signal can be produced by one DAC while another DAC can output a signal with same amplitude but reversed phase. These two signals have a phase difference of 180° and developed into I+,I- via Howland circuit. User can obtain a pair of pumping signals by switching matrix which illustrated as shown in Fig 2.

The function of planar electrode driving circuit is to realize the switching process between a pair of current sources to 85 electrodes. Single to differential amplifier, Howland V/I transform circuits and switching matrix constitute the driving circuit. At last, the two way Howland circuits get two way differential current respectively.

The types of chips are as follows:

1) Switching matrix: ADG2128. Which has double-buffered input logic and 300 MHz bandwidth. It's on resistance is 35 Ω maximum
2) Switching matrix: AD8115, which is a 16 × 16 high speed non-blocking switch array with 225 MHz −3 dB bandwidth.

As the chips we selected, the switching channel method of our system has many advantages. In our practical use, Its bandwidth can reach 5KHz to 10MHz, which is good enough to meet the system's requirement (10KHz to 5MHz). What's more, the new switch matrix we adopted also have outstanding performance in power dissipation, SNR and can allow more electrodes (up to 96) to be employed in future systems.

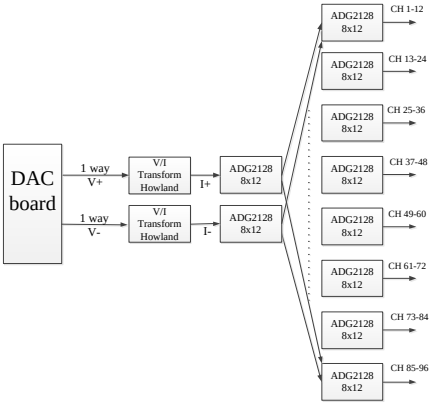

Fig 2. Planar electrode driving circuit

3 Conclusions

The testing results indicate that, for the Cambridge MK4 EIT system, the bandwidth of the channel without I/V circuit is 5KHz to 10MHz. In our design, the switching matrix is controlled by FPGA, hence the switch channel is stably during data acquisition. The test results proves the design is an outstanding scheme for channel switching of EIT System.

References

[1] S. Zhang, G. Z. Xu, X. Y. Zhang, B. Zhang, H. B. Wang, Y. Y. Xu, et al., "Computation of a 3-D Model for Lung Imaging With Electrical Impedance Tomography," IEEE Transactions On Magnetics, vol. 48, pp. 651-654, Feb 2012.

[2] Q. Liu, T. I. Oh, H. Wi, E. J. Lee, J. K. Seo, and E. J. Woo, "Design of a microscopic electrical impedance tomography system using two current injections," Physiological Measurement, vol. 32, Sep 2011.

[3] A. Borsic, R. Halter, Y. Wan, A. Hartov, and K. D. Paulsen, "Electrical impedance tomography reconstruction for three-dimensional imaging of the prostate," Physiological Measurement, vol. 31, pp. S1-S16, Aug 2010.

[4] B. Nevis, S. Gerald, H. Nick, and W. Wei, "The flexible and configurable Sussex EIM MK4 using PCI eXtensions for Instrumentation (PXI)," Journal of Physics: Conference Series, vol. 224, p. 012164, 2010.

Factors affecting Sensitivity Maps in Magnetic Induction Tomography

Yasin Mamatjan[1], Ali Roula[2], Stuart Watson[3], Kurban Ubul[4], Robert J. Williams[2]

[1]Zirve University, Gaziantep, Turkey [2]University of South Wales, UK [3]Salford Royal NHS Foundation Trust, UK,
[4]Xinjiang University, China, Mamatjan.yasin@zirve.edu.tr

Abstract: Image reconstruction in Magnetic Induction Tomography (MIT) depends on a sensitivity distribution in a conducting volume, rather than a free-space background. The consideration of factors affecting sensitivity map generation is essential to optimise image reconstruction. The aim of this paper is to investigate such factors and to simulate sensitivity maps while varying conductivity contrast levels and perturbation dimensions.

1 Introduction

In Magnetic Induction Tomography (MIT), a sensitivity matrix maps the changes of conductivity distribution on to the changes of the voltages induced in a receiver coil. Korjenevsky *et al* [1] used filtered backprojection to reconstruct images (of plastic bottles containing saline solution both in free space and placed inside a larger saline filled tank), arguing that the regions of high sensitivity corresponded to 'flux tubes' linking the excitation and detection coils. Scharfetter *et al* [2] computed the sensitivity maps for low-contrast perturbations in a conducting background and concluded that the sensitivity was not confined to flux tubes; rather, they found that areas of maximum sensitivity lay on the periphery of the object and were strongly influenced by its conductivity contrast and the geometry. To optimise image reconstruction, it is essential to systematically analyse key factors affecting the sensitivity map. These include coil metrics and object geometry, the number of voxels, conductivity contrast and excitation frequency.

2 Methods

In this study, sensitivity maps were first computed for the coil design and application employed in the Cardiff MIT system [3], termed opposed coils, for a cylindrical sample volume (radius 10 cm, height 20 cm) with homogeneous non-zero conductivity, applying varying conductivity contrast and perturbation dimensions. In the perturbation method, the conductivity of all voxels in the modelled volume was set to 1 Sm^{-1}. A cubic group of voxels (*image voxel*) were then perturbed from 1 Sm^{-1} by a selected percentage in the range of 1% - 1000000%. The voxels were then reset to 1 Sm^{-1} and a new group of voxels were selected. This was repeated to produce N × N × N image voxels covering the modelled volume for each coil combination, with the sensitivity matrix in this case having the dimensions of 240 (coil combinations) × 8000 (image voxels). The perturbation method allows sensitivity matrices to be derived for both the low contrast case with low percentage perturbations, and the high contrast case using high percentage perturbations. The modelled volume was discretised into 80 × 80 × 80 cubic voxels, each of side 0.25 cm.

3 Results

Figure 1 shows the sensitivity maps of various conductivity and perturbation dimensions for an *opposed coil* arrangement. The columns show the sensitivity maps produced by applying perturbations of 1%, 10000%, 50000%, 100000% and 1000000%, corresponding to conductivities of 1.01 Sm^{-1}, 100 S m^{-1}, 500 Sm^{-1}, 1000 Sm^{-1} and 10000 Sm^{-1} respectively with a 1 Sm^{-1} background. The 2nd to 4th rows show sensitivity maps derived using perturbations of 4×4×4, 8×8×8, 16×16×16 voxels. The last row shows a freespace sensitivity map derived for a 4×4×4 perturbation of 1 Sm^{-1} in a 0 Sm^{-1} background. In each case, the map shows the sensitivity distribution at a cross-section of the mid-point of the volume, which corresponds to layer 40.

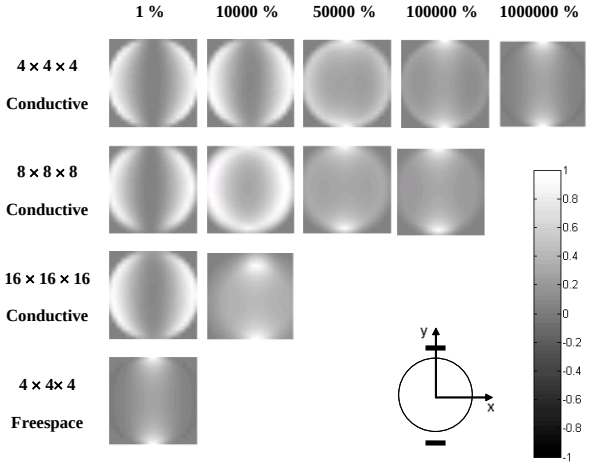

Figure 1: Sensitivity maps produced by applying perturbations of different percentage contrast levels and dimensions.

4 Conclusions

Several publications report MIT image reconstructions implemented when using metal objects. Such high contrast conductivity distributions may have localised zones of sensitivity, with eddy currents, and hence sensitivity localised within these zones. They appear to produce sensitivity distributions equivalent to the freespace condition. By comparison, lower contrast distributions produce a greater spatial range, appearing primarily at the periphery of the object. In conclusion, conductivity values and contrast greatly influence the sensitivity distribution of MIT systems, and these should be carefully selected as relevant to the application when developing algorithms and phantoms. Results obtained using metals objects, for instance, would not be expected to be relevant to most biomedical applications, and could be misleading.

References

[1] A. Korjenevsky, *et al*., *Physiol. Meas*., **21** 89-94, 2000
[2] H. Scharfetter, *et al*., *Physiol. Meas*., **23** 195-202, 2002
[3] S. Watson, *et al*., Meas. Sci. Technol., **19** 045501, 2008

Session 3

Reconstruction I

24 April 2014, 10:30 – 12:15

A Finite Difference Solver for the D-bar Equation

Peter Muller[1], David Isaacson[2], Jonathan Newell[2], Gary Saulnier[2]

[1]Rensselaer Polytechnic Institute, Troy, NY, mullep@rpi.edu
[2]Rensselaer Polytechnic Institute, Troy, NY

Abstract: A finite difference scheme is introduced to solve the D-bar equation. The D-bar equation arises in electrical impedance tomography (EIT) when using the complex geometrical optics solutions to recover the conductivity within a body. This scheme is second-order and is first used on a test equation for error analysis and then used to reconstruct EIT images using the D-bar method.

1 Introduction

In 1996, A. Nachman [1] developed the D-bar method, which proved that the inverse conductivity problem in 2-D, described by A. Calderón [2], has a unique solution. This method reduces to finding the solutions to the D-bar equation

$$\bar{\partial}_k \mu(z,k) - \frac{1}{4\pi\bar{k}} \mathbf{t}(k) e^{i(kz+\bar{k}\bar{z})} \bar{\mu}(z,k) = 0 \qquad (1a)$$

$$\lim_{|z|,|k|\to\infty} \mu(z,k) = 1, \qquad (1b)$$

where $z \equiv x+iy$, $k \equiv k_1 + ik_2$, $\bar{\partial}_k \equiv \frac{1}{2}(\frac{\partial}{\partial k_1} + i\frac{\partial}{\partial k_2})$ and $\mathbf{t}(k)$ is the non-physical scattering transform, which contains all data information. The conductivity, γ, can be recovered by the relation $\gamma^{\frac{1}{2}}(x,y) = \lim_{|k|\to 0} \mu(z,k)$. Nachman suggests solving an equivalent integral equation to find μ. Current numerical implementations of the D-bar method solve these integral equations as is done in [3–5]. We seek to solve the D-bar equation (1a) as a partial differential equation using finite differences.

2 Methods

To account for the complex conjugate operator on μ in (1a), we solve the equivalent system of equations found by equating the real and imaginary parts of (1a). Thus, we seek to solve

$$\frac{1}{2}(\frac{\partial}{\partial k_1}u - \frac{\partial}{\partial k_2}v) - (au+bv) = 0 \qquad (2a)$$

$$\frac{1}{2}(\frac{\partial}{\partial k_2}u + \frac{\partial}{\partial k_1}v) - (bu+av) = 0 \qquad (2b)$$

where $\mu(z,k) \equiv u(z,k) + iv(z,k)$ and $\frac{1}{4\pi\bar{k}}\mathbf{t}(k)e^{i(kz+\bar{k}\bar{z})} \equiv a(z,k) + ib(z,k)$. We approximate the first derivatives in the D-bar operator using centered finite differences. This leads to an $O(h^2)$ truncation error for a uniform mesh spacing, h. We truncate the complex domain to a finite domain $\Omega = [-R,R]^2$ for implementation, and impose the numerical boundary condition approximation $\mu(z,k)|_{\partial\Omega} = 1$. The resulting scheme reduces to solving a $2N^2$x$2N^2$ linear system, as in [3–5], where $h = 2R/(N+1)$. Here the system is sparse with $O(N^2)$ non-zero entries.

3 Results

To test our solver, we use the test function $\mu_1(z,k) = e^{-|k|^2-|z|^2-2i(k_1k_2+xy)} + 1$ for fixed z and assume no scattering, resulting in the equation $\bar{\partial}_k\mu_1 = f$ with boundary condition $\mu_1|_{\partial\Omega} = g$. Thus, we solve (2) but with the right hand sides of (2a) and (2b) replaced by $\alpha(z,k)$ and $\beta(z,k)$, respectively, where $f = \alpha + i\beta$ and $a = b \equiv 0$. A plot of the relative errors when solving (1a) can be found in 1a. Note the plateau in error that occurs for $R = 2$. This is caused by the imposed Dirichlet boundary condition on the finite domain, the approach also taken by [3–5]. For small enough h, the other error plots will also plateau, but will decrease with order two until that point. This suggests that the scheme converges with order two, but further analytic work is required to prove this. Figure 1b shows cross-sections of reconstructions of a concentric circle target with radius 0.3 inside a unit circle. The error plateau is evident since the reconstructions are almost identical for larger values of N. Despite this plateau, the conductivity is reconstructed. Improvements in the reconstruction can be made by adjusting R and a regularization parameter in the D-bar method. This solver also works when reconstructing images using experimental data.

References

[1] Nachman A. *Ann Math 2* **143**:71–96, 1996
[2] Calderón A. *ATAS of SBM* 65–75, 1980
[3] Isaacson D, Mueller J, Newell J, et al. *IEEE Trans Med Imag* **23**:821–828, 2004
[4] Knudsen K, Mueller J, Siltanen S. *J Comput Phys* **198**:500–517, 2004
[5] Siltanen S, Mueller J, Isaacson D. *Inv Prob* **16**:681–699, 2000

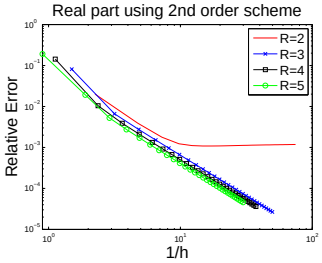

(a) Plateaus in the error occur because of the boundary approximation.

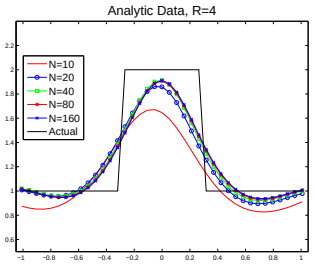

(b) Reconstruction of a concentric target with analytically calculated scattering transform.

Figure 1

Reconstructions of conductivity and permittivity from EIT data on a human chest by D-bar methods

Claudia Natalia Lara Herrera[1], Miguel Fernando Montoya Vallejo[2], Jennifer L. Mueller[3], Raul Gonzalez-Lima[4]

[1]Universidad Antonio Nariño, Bogotá, Colombia
[2]Universidad Antonio Nariño, Bogotá, Colombia
[3]Colorado State University, Fort Collins, CO USA 80523, mueller@math.colostate.edu
[4]University of São Paulo, Brazil

Abstract: A direct D-bar reconstruction algorithm is presented for reconstructing a complex conductivity from 2-D EIT data. The method is applied to simulated data and archival human chest data. Permittivity reconstructions with this new method and conductivity reconstructions with the fully nonlinear D-bar method based on [1] depicting ventilation and perfusion in the human chest are presented.

1 Introduction

In this work a direct nonlinear reconstruction algorithm using the D-bar method is presented for the computation of conductivity and permittivity on a chest-shaped domain. The conductivity and permittivity are modeled as a complex coefficient $\gamma = \sigma + i\omega\varepsilon$ in the generalized Laplace equation where ω represents the angular frequency of the applied current, σ the conductivity, and ε the permittivity.

There are two D-bar methods shown here. To obtain reconstructions of the real part of the admittivity for the human data, the D-bar method based on the global uniqueness proof by Nachman [2] is employed. Here, the fully nonlinear scattering transform is used for the first time with human data. To compute reconstructions of the permittivity, a direct method introduced in [3] was utilized. The method is based on the uniqueness proof by Francini [4], but equations relating the Dirichlet-to-Neumann to the scattering transform and the exponentially growing solutions are not present in that work. Such equations are derived in [5], and an alternative formulation with a different formula for the scattering transform from [3] is used here.

2 Methods

2.1 Algorithms

The conductivity was computed using the fully nonlinear D-bar method based on [1, 2, 6]. The permittivity was computed using a new D-bar method based on the elliptic system of complex geometrical optics (CGO) solutions introduced in the global uniqueness proof of Francini [4]. As in other D-bar methods, there is a direct relationship between the CGO solutions, and the coefficient in the generalized Laplace equation, which in this case is the admittivity. In this method, the scattering transform is a 2×2 matrix of functions with nonzero off-diagonal entries, related to the CGO solutions by a boundary integral equation. Here, a linearized scattering transform is used, which partially linearizes the method. The lengthy equations are omitted for brevity.

2.2 Data Collection

We consider two sets of 100 frames of archival data collected at 18 frames/s on the chest of an adult male sitting upright, using the ACT3 system at RPI [7]. One set was collected during breathholding to image perfusion, and the other set consisted of a deep slow inhalation followed by slow exhalation to image ventilation. In both cases, the trigonometric current patterns with current amplitude 0.85 mA were applied on 32 electrodes placed around the circumference of the chest.

2.3 Results

In Figure 1 a selection of five difference images of the conductivity and permittivity distributions in a healthy human subject during a slow ventilation maneuver. The first frame was chosen as the reference frame. Close agreement between the conductivity and permittivity images is observed, as may be expected in a healthy subject, and changes due the to increased resistivity during inhalation are clearly visible.

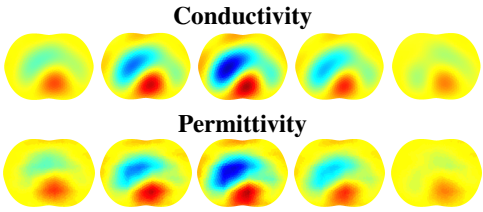

Figure 1: Top row: Red is high conductivity and blue low conductivity. Bottom row: Red is high permittivity and blue low permittivity.

3 Conclusions

We have presented a direct D-bar method for computing reconstructions of both conductivity and permittivity from human chest data on a 2-D cross-sectional domain. This constitutes the first fully nonlinear D-bar reconstructions of human chest data and the first D-bar permittivity reconstructions of experimental data. Difference images of ventilation and perfusion in a healthy human subject do not exhibit boundary artefacts and clearly show changes due to blood flow between the heart and lungs and gas exchange.

References

[1] Knudsen K, Lassas M, Mueller JL, and Siltanen S, *Inverse Problems and Imaging*, 3:599–624, 2009.
[2] Nachman AI, *Ann. of Math.*, 143:71–96, 1996.
[3] Herrera CNL, *PhD thesis, University of São Paulo, Brazil*, 2012.
[4] Francini E, *Inverse Problems* 6:107–119, 2000.
[5] Hamilton SJ, Herrera CNL, Mueller JL and Von Herrmann A, *Inverse Problems*, 28:095005, 2012.
[6] Siltanen S, Mueller JL, and Isaacson D, for the 2D inverse conductivity problem. *Inverse Problems*, 16:681–699, 2000.
[7] Edic PM, Saulnier GJ, Newell JC, and Isaacson D, *IEEE Trans. Biomed. Eng.*, 42:849–859, 1995.

Fine-tuning of the Complete Electrode Model

Robert Winkler[1], Stratos Staboulis[2], Andreas Rieder[1], Nuutti Hyvönen[2]

[1]Karlsruhe Institute of Technology, Karlsruhe, Germany, robert.winkler@kit.edu
[2]Aalto University, Helsinki, Finland, stratos.staboulis@aalto.fi

The work of the authors was supported by the German Research Foundation (DFG) and the Academy of Finland.

Abstract: The Complete Electrode Model (CEM) is a realistic measurement model for Electrical Impedance Tomography. We present a non-uniform discretization of the conductivity space based on its sensitivity to boundary data and an adaptive adjustment of electrode parameters leading to improved reconstructions of Newton-type solvers. We demonstrate the performance of this concept when reconstructing with incorrect geometry assumptions from noisy data.

1 Sensitivity-based conductivity discretization

The Neumann-to-Dirichlet (ND) map Λ_σ of the CEM with L electrodes is an $L \times L$ matrix that maps the applied currents to the resulting (measured) potential vectors, where σ is the conductivity on a domain $\Omega \subset \mathbb{R}^2$, cf. [1]. By

$$\lambda_\sigma = \|\Lambda_\sigma - \Lambda_1\| / \|\Lambda_1\|,$$

we define the *sensitivity* for distinguishing a conductivity $\sigma \in L^\infty_+(\Omega)$ from the homogeneous case $\sigma \equiv 1$ by boundary measurements. For $\Omega = B_1(0)$, we can determine λ_σ analytically for conductivities of the form $\sigma = 1 + \delta\chi_D(x)$, where D is a disk inside Ω. With this information, we discretize the conductivity space such that the ND map is equally sensitive to perturbations δ in each segment. This is achieved by filling the disk with non-overlapping circles resulting in equal sensitivity for perturbations and applying Voronoi tessellation afterwards to get a partition of the entire disk. Motivated by the similarities between the CEM and the continuum boundary model of EIT, we derive a simple heuristic to generate sensitivity-based conductivity discretizations for non-circular domain geometries. A sensitivity-based discretization for a setting with 16 electrodes and a heuristic approximation for a non-circular domain are shown in fig. 1.

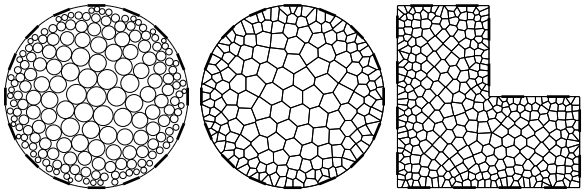

Figure 1: Left: Sizes of circular perturbations resulting in a sensitivity $\lambda_\sigma = 0.02$. Center: Corresponding Voronoi tessellation. Right: Heuristic approx. of a sensitivity-based discretization.

The advantage over generic triangulations is that each conductivity coefficient is equally sensitive to measurement noise, thus regularization during inversion can effectively be applied by a single parameter, i.e. the estimated noise level of the data, free of additional priors. Fig. 2 shows reconstructions on uniform and sensitivity-based discretizations with the same number of coefficients for simulated data Λ_σ with 1% artificial noise.

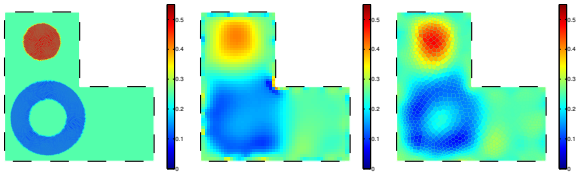

Figure 2: Left: True setting. Center: Reconstruction on a uniform mesh, convergence after 33 Newton-iterations with 23% rel. error. Right: Reconstruction on a sensitivity mesh (13 it., 18% error).

2 Adjustment of the electrode parameters

Most EIT applications involve non-circular domain geometries. Even for circular domains, the electrode parameters (location, contact impedance) are usually not known exactly which can cause severe reconstruction artifacts. To account for these model uncertainties, we incorporate the reconstruction of the electrode parameters into the reconstruction process of the conductivity. This is done by adding the Fréchet derivative of the ND map with respect to the contact impedance, see e.g. [2], and the Fréchet derivative with respect to the electrode location, see [3], to the inexact Newton-type algorithm REGINN [4]. Moreover, the adaptive adjustment of the electrode locations can be helpful in dealing with non-circular domain geometries. According to the Riemann mapping theorem, any simply connected domain in $\mathbb{R}^2$ can be mapped onto the unit disk conformally. For the CEM, this means that the electrode parameters change. When the original domain is not too far from a circle (e.g. an ellipse), we observe that the reconstructed image is a conformally mapped solution of the true domain without additional artifacts. This is shown in fig. 3.

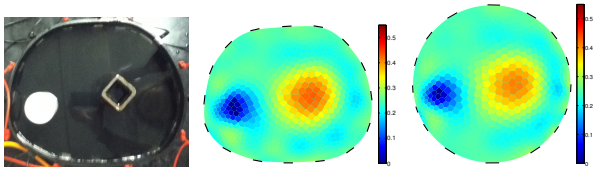

Figure 3: Left: Measurement setting with a resistive inclusion (left) and a conducting inclusion (right). Data kindly provided by Aku Seppänen, University of Eastern Finland. Center: Reconstruction on the estimated domain. Right: Reconstruction on a disk.

3 Conclusions

With a sensitivity-based conductivity discretization and an adaptive adjustment of the domain geometry, we introduced a reconstruction scheme for EIT which considers effects of measurement noise and is robust to geometry inaccuracies, resulting in improved reconstructions over generic solvers.

References

[1] Somersalo E, Cheney M, Isaacson D. *SIAM J Appl Math* 1992
[2] Vilhunen T, Kaipio JP, Vauhkonen PJ, et al. *Measurement Science and Technology* **13**(12):1848, 2002
[3] Darde J, Hakula H, Hyvönen N, et al. *Inverse Problems and Imaging* **6**:399–421, 2012
[4] Rieder A. *Inverse Problems* **15**(1):309–327, 1999

An efficient transport back-transport framework for EIT

Alexandre Fouchard[1,2], S. Bonnet[1], L. Hervé[1] and Olivier David[2]

[1]CEA, Leti, 17 rue des Martyrs, 38000 GRENOBLE, France, alexandre.fouchard@centraliens-lyon.net
[2]Univesité Joseph Fourier, Grenoble Institute of Neuroscience, Bât. E.J. Safra, Chemin Fortuné Ferrini, 38700 La Tronche, France

Abstract: Implementation of efficient methods to handle calculations in EIT is a key issue to address 3D electrical property reconstructions. Following a transport back-transport method, we develop in this work an adjoint approach and define explicit forward and back-projection operators. It allows reducing the size of matrices involved in reconstruction. This framework has been tested on experimental data acquired *in vitro* on a saline phantom.

1 Introduction

Forward problem solution and sensitivity computations are the fundamentals of Electrical Impedance Tomography (EIT) [1]. Standard approach is to use Finite Element Methods (FEM) to derive both admittance matrix and Jacobian from an elemental discretization of conductivity. Calculation parallelization [2] and deduction of nodal Jacobian [3] offer ways to enhance calculus efficiency.

In most EIT systems, the same measurement configuration is used per injection configuration. Then, following a transport back-transport method [4], we explicitly define forward and back-projection operators from potential gradients. It allows using inversion algorithms without explicit Jacobian assembly. Matrix size involved in reconstruction is proportional to the number of electrodes E instead of the number of measurements.

2 Methods

We elaborate our framework supposing the electric potential $\mathbf{v} \in \mathbb{R}^{N_n}$ linear per element and considering a piecewise constant conductivity discretization $\boldsymbol{\sigma} \in \mathbb{R}^{N_e}$.

2.1 Sensitivity calculations, adjoint framework

Classical estimation of Jacobian coefficient is based on the perturbation approach [5]. Two configurations are considered: the actual measurement configuration, and a virtual measurement configuration in which source and detector have been interchanged. In this work, the Jacobian matrix is factorized with matrices containing elemental potential gradients. They can be determined by standard FEM formulation [6]. Using only the gradient matrices, a forward operator is defined and solves a direct transport problem. A back-projection operator is also defined and transports back residuals into the imaging domain. The profit of such a formulation relies upon the size of gradient matrices $\mathbf{G} \in \mathbb{R}^{N_e \times E}$ used in inversion, versus the larger size of standard Jacobian matrix, typically $\mathbf{J} \in \mathbb{R}^{N_e \times E^2}$. Inversion is then done with a standard preconditioned conjugate gradient (PCG).

2.2 Experimental device

Experimental measurements are performed on a saline phantom of 4cm diameter featuring 14 equally-spaced copper electrodes with a custom-built EIT system [7].

2.2.1 Reconstruction approach

The implementation of the framework, adapted from the EIDORS library [8], is first validated on simple test cases in 2D before exploring reconstructions from noisy simulated measurements. Reconstructions are then performed against experimental data.

3 Results

Reconstructions from simulated data (Figure 1) exhibit a correct behaviour of the framework and PCG algorithm used for inversion. The framework performs also well in experimental situation (Figure 2).

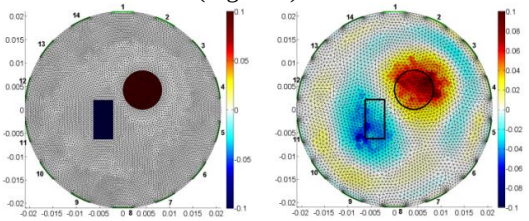

Figure 1: 2D difference reconstructions from simulated data with 5% additive Gaussian noise

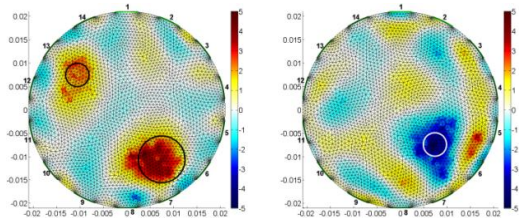

Figure 2: 2D difference reconstruction from experimental data, with estimated 5% noise

4 Discussion

The framework presented in this work allows inversion without explicit Jacobian calculations, working only with potential gradient matrices for injection and measurement configuration. It has been validated against both simulated and *in vitro* experimental measurements.

Further investigation might consider reconstructions that favour sparse solutions and make use of non-linear inversion algorithms.

References

[1] Lionheart W R B, *Physiol Meas*, **25**(1):125, 2004
[2] Borsic A, Attardo E A, Halter R J, *Physiol Meas*, **33**(10):1703, 2012
[3] Graham B M, Adler A, *Int J Inf Syst Sci*, **2**:453–68, 2006
[4] Dorn O, *Inverse Problems*, **14**:1107-30, 1998
[5] Geselowitz D B, *IEEE Trans Biomed Eng*, **18**(1):38–41, 1971
[6] Vavasis S A, *SIAM J. Numer. Anal.*, **33**(3):890-916, 1996
[7] Fouchard A, Noca A, Bonnet S, Pham P, Clarençon D, David O, submitted in *IEEE EMBC*, 2014
[8] Adler A, Lionheart W R B, *Physiol Meas*, **27**:S25-42, 2006

Resolution guarantees in EIT including random and systematic errors

Bastian Harrach[1] and Marcel Ullrich[1]

[1]Department of Mathematics, University of Stuttgart, Stuttgart, Germany, harrach@math.uni-stuttgart.de and marcel.ullrich@mathematik.uni-stuttgart.de

Abstract: To improve the practical applicability of electrical impedance tomography is a great ongoing challenge. Theoretical identifiability results exist for noiseless continuous boundary measurements. However, little is known about what can be achieved with a finite number of realistically modelled electrodes in a setting including modelling and measurement errors. In this paper, we sketch how to derive rigorous resolution guarantees for such settings.

1 Introduction

Notation: χ_M denotes the characteristic function of a set M and $\mathrm{eig}(A)$ the set of eigenvalues of a square matrix A.

We consider a conductive object $\Omega \subseteq \mathbb{R}^n$ ($n \in \{2,3\}$) with a conductivity distribution

$$\sigma : \Omega \to \mathbb{R}, \quad \sigma(x) = \sigma_B(x)\chi_{\Omega\setminus D}(x) + \sigma_D(x)\chi_D(x), \quad (1)$$

where $\sigma_B(x)$ is the background conductivity and $\sigma_D(x)$ the inclusion conductivity of an inclusion $D \subseteq \Omega$. The inclusion is characterized by a contrast to the background with

$$\inf_{x\in D} \sigma_D(x) \geq \sigma_{D\min} > \sup_{y\in\Omega\setminus D} \sigma_B(y), \quad \sigma_{D\min} \in \mathbb{R}. \quad (2)$$

Furthermore, let $(\omega_1, \omega_2, \cdots, \omega_N)$ be a resolution partition of Ω (see Figure 1). In Section 3, we sketch how to verify if a realistically modelled measurement setting (see Section 2) yields enough information to design an inclusion detection method that fulfils the following guarantee.

Resolution guarantee (RG):

(a) A resolution element ω_i will be marked if $\omega_i \subseteq D$.
(b) No resolution element will be marked if $D = \emptyset$.

2 The measurement setting

The setting is given by current-voltage measurements on a finite number of (almost perfectly conductive) electrodes $E_1, E_2, \ldots, E_L$. We assume that a contact layer between each electrode E_i and Ω leads to a contact impedance $z^{[i]}$.This setting is mathematically modelled by the complete electrode model (CEM), cf. [1]. For a conductivity distribution σ and contact impedances given by the components of $z \in \mathbb{R}^L$, the measurement matrix is defined by

$$R(\sigma,z) = \left(R^{[i,j]}(\sigma,z)\right)_{i,j=1}^{L-1} \in \mathbb{R}^{L-1\times L-1}, \quad (3)$$

where the components $R^{[i,j]}(\sigma,z)$ are given by the measurements as in Fig. 1. The matrix $R(\sigma,z)$ is symmetric, cf. [1].

To allow for **modelling and measurement errors**:

(a) The background conductivity $\sigma_B(x)$ is given approximately by $\sigma_0(x)$ with $\|\sigma_B - \sigma_0\|_\infty \leq \varepsilon \in \mathbb{R}$.
(b) The vector z (contact impedances) is given approximately by z_0 with $\|z - z_0\|_\infty \leq \gamma \in \mathbb{R}$.
(c) There are noisy measurements $R_\delta(\sigma,z)$ given with an absolute noise level $\delta \geq \|R(\sigma,z) - R_\delta(\sigma,z)\|_2$, $\delta \in \mathbb{R}$. Possibly replacing $R_\delta(\sigma,z)$ by its symmetric part, we can assume that $R_\delta(\sigma,z)$ is symmetric.

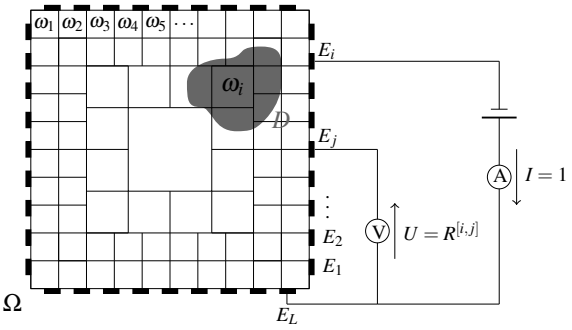

Figure 1: Setting with a sample resolution for $\Omega = [-1,1]^2$.

3 Verification of the resolution guarantee

Let $\sigma_0(x)$, z_0, ε, γ, δ and $\sigma_{D\min}$ be given. We define

$$\sigma_{B\min}(x) := \sigma_0(x) - \varepsilon, \quad \sigma_{B\max}(x) := \sigma_0(x) + \varepsilon, \quad (4)$$

$$z_{\min} := z_0 - \gamma(1,\ldots,1), \quad z_{\max} := z_0 + \gamma(1,\ldots,1), \quad (5)$$

$$\tau_i(x) := \sigma_{B\min}(x)\chi_{\Omega\setminus\omega_i}(x) + \sigma_{D\min}\chi_{\omega_i}(x) \quad (6)$$

for $i \in \{1,2,\ldots,N\}$. Then the **RG is possible** if

$$\max_{i=1}^{N} \min \mathrm{eig}\left(R(\tau_i, z_{\max}) - R(\sigma_{B\max}, z_{\min})\right) < -2\delta. \quad (7)$$

The proof is based on the monotonicity relation

$$\sigma_1 \leq \sigma_2,\ z_1 \geq z_2 \quad \Rightarrow \quad R(\sigma_1,z_1) - R(\sigma_2,z_2) \geq 0. \quad (8)$$

The main idea is to consider (7) as a worst-case scenario test for Algorithm 1 (cf. [2] for $\gamma = 0$).

Algorithm 1: Mark element ω_i if

$$\min \mathrm{eig}\left(R(\tau_i, z_{\max}) - R_\delta(\sigma,z)\right) \geq -\delta. \quad (9)$$

3.1 Numerical results

Let Ω be given with a resolution partition as in Fig. 1. Furthermore, let $\sigma_0 \equiv 1$ and $z_0 = (1,\ldots,1) \in \mathbb{R}^L$ be approximations of the background conductivity $\sigma_B(x)$ and the vector z (contact impedances), respectively. Additionally, let $\sigma_{D\min} = 2$ be a lower bound of the inclusion conductivity.

Then (7) is fulfilled for a background error of $\varepsilon = 1\%$, an absolute measurement noise level of $\delta = 0.9\%$ and exactly given contact impedances ($\gamma = 0$). Hence, the RG is possible. In particular, Algorithm 1 fulfils the RG.

The results can be extended to the case of approximately known contact impedances.

4 Conclusion

This paper presents the possibility of a rigorous resolution guarantee for a realistically modelled electrode measurement setting including modelling and measurement errors. The resolution guarantee can be verified by a simple test.

References

[1] Somersalo E, Cheney M, Isaacson D. *SIAM J Appl Math* **52**(4):1023–1040, 1992

[2] Harrach B, Ullrich M. In *Journal of Physics: Conference Series*, vol. 434, 012076. IOP Publishing, 2013

EIT Spatial Filtering in realistically shaped head models

Mariano Fernández-Corazza[1,2], Nicolás von Ellenrieder[1,2], Carlos Muravchik[1,3]

[1]Laboratorio de Electrónica Industrial, Control e Instrumentación (LEICI), Universidad Nacional de La Plata (UNLP), Argentina.
[2] CONICET, Argentina. [3] CICpBA, Argentina. marianof.corazza@ing.unlp.edu.ar

Abstract: We demonstrate the use of Spatial Filtering in EIT (EIT-SF) to estimate the time course and position of localized conductivity changes in the brain, when modelling ischemic stroke and neuronal activation. We compare the solutions obtained for three head models. Results support the use of EIT-SF to localize and characterize dynamic conductivity changes in the human brain.

1 Introduction

We showed in a previous study [1] that Electrical Impedance Tomography Spatial Filtering (EIT-SF) is able to localize a conductivity change within the brain. In this work we extend the results to estimate the time evolution of the conductivity change and analyze the use of approximate head models.

2 Methods

2.1 Simulated Signals

We simulated two different, dynamic, conductivity changes: a linear decrease up to 30% of the baseline conductivity (simulating ischemic stroke) [2], and a gaussian shaped pulse with a maximum of 10% of the baseline conductivity (simulating neuronal activity) [3]. Signals were simulated on a head model built from Magnetic Resonance images of a subject. The conductivity changes $\delta\sigma(t)$ were assigned to a $1cm$ radius sphere (Vol $\approx 4.22cm^3$) near the motor cortex (P1), the superior temporal gyrus (P2), and the insula (P3) (see Fig. 1a). We assumed 64 electrodes and 63 alternating current injection pairs (the Cz electrode fixed), resulting in a signal vector $y(t)$ of 3906 elements per each of the 21 simulated snapshots. The forward problems, i.e the computation of the electric potentials at the sensor positions, were calculated using the Finite Element Method, for a current of $100\mu A$. White additive gaussian noise (WGN) $n(t)$ with different standard deviations (Std Dev) was added to the signals to simulate noisy measurements. The model for a conductivity change $\delta\sigma(t)$ at position $\vec{x}_i$ is:

$$y(t) = l(\vec{x}_i)\delta\sigma(t) + n(t), \tag{1}$$

where $l(\vec{x})$ is the forward problem solution for a unitary conductivity change at position $\vec{x}$.

2.2 Linearly Constrained Minimum Variance (LCMV) filter

From the simulated signals, we performed the localization and time course estimation with three different head models: individual-specific (M1), atlas-based (M2), and three-shell concentric spherical (M3) models. The LCMV filter multiplies the signal by a weight vector $w(\vec{x})$ such that the output $w(\vec{x})^T y(t)$ is the unbiased estimator of $\delta\sigma(t)$ at position $\vec{x}$ with minimum variance. The LCMV filter is [1, 4]:

$$\widehat{\delta\sigma(t,\vec{x})} = w(\vec{x})^T y(t) = \frac{l(\vec{x})^T C_y^{-1} y(t)}{l(\vec{x})^T C_y^{-1} l(\vec{x})}, \tag{2}$$

where C_y stands for the sample covariance matrix of $y(t)$. For each situation we computed the Conductivity Change Index (CCI) (based on [4]) to study the localization, as the norm of $l(\vec{x})$ is a function of the position $\vec{x}$:

$$\mathrm{CCI}(\vec{x}) = \frac{w^T(\vec{x}) C_y w(\vec{x})}{w^T(\vec{x}) w(\vec{x})}. \tag{3}$$

For M1 and M3, we performed a 9 parameter linear registration (translation, rotation, and scaling) to M2, adopting the electrode positions as the registration marks.

2.3 Results

The results are shown in Fig. 1. The localization errors were below $8.5mm$ for the M1 model ($0.1\mu V$ noise Std Dev), and the error when localizing with an approximate model was below $16mm$. The dispersion depends on the noise as depicted in Fig. 1a.

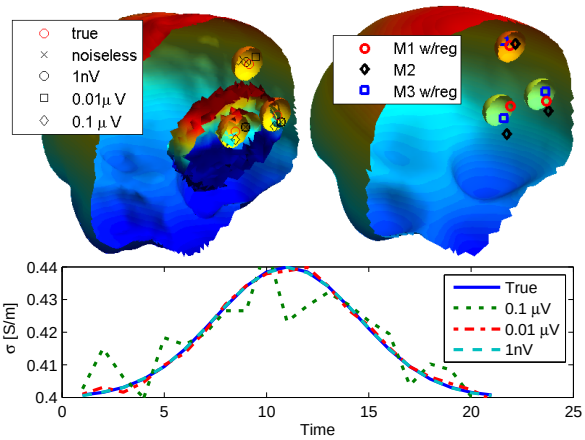

Figure 1: (a) Localization of the linear conductivity change using M1 for different noise levels. Two isosurfaces indicating dispersion are also displayed for the $0.1\mu V$ and $0.01\mu V$ noise Std Devs. (only P3). (b) Same localization but using the three models with registration to M2 and noiseless signals. (c) Normalized outputs for the gaussian pulse at P2 and with M2.

3 Conclusions

EIT-SF was used to successfully locate a conductivity change and to estimate its time course, even without using the individual-specific geometry. This suggests that EIT-SF is a promising technique to study ischemic stroke and neuronal activity.

References

[1] Fernández-Corazza M, von Ellenrieder N, Muravchik CH. *J Phys Conf Ser* **407**(1), 2012. Pp. 012023

[2] Horesh L. *Some Novel Approaches in Modelling and Image Reconstruction for Multi-Frequency Electrical Impedance Tomography of the Human Brain*. Ph.D. thesis, University College London, 2006

[3] Abascal JFP, Arridge SR, Atkinson D, et al. *NeuroImage* **43**(2):258 – 268, 2008

[4] Sekihara K, Nagarajan SS. *Adaptive Spatial Filters for Electromagnetic Brain Imaging*. Springer, Berlin, 2008

Session 4

Hardware I

24 April 2014, 13:30 – 15:15

120-channel electrode arrays for rat brain: Towards 3D EIT imaging

MA Koronfel[1], K Aristovich[1], A Vongreichten[1], G Dos Santos[1] and DS Holder[1]

[1]University College London, London, United Kingdom

Abstract: EIT has much potential in many brain imaging applications demonstrated through animal experiments with a small epicortical 30-channel array. Spatial resolution can be improved by using a larger array to cover most of brain. A 120-channel electrode system was fabricated and successfully implanted covering c.90% of brain, and EIT data was successfully recorded.

1 Introduction

EIT has the potential to provide a radically new portable inexpensive way to image brain function in conditions like stroke or epilepsy, blood volume changes during evoked responses or even millisecond neural depolarisation during normal activity. EIT has been successfully used in our group previously to image impedance changes related to these conditions on the rat brain using a 5 x 7 mm 30-channel epicortical planar electrode array, custom made from stainless steel foil on silicone rubber [1]. This gave a resolution of 200µm in cerebral cortex but modelling indicated that more electrodes were needed to achieve satisfactory resolution throughout the entire brain (Fig. 1). The purpose of this work was to develop and test electrode arrays able to apply 120 electrodes to cover most of the rat brain. We evaluated their suitability for surgical insertion and impedance recording.

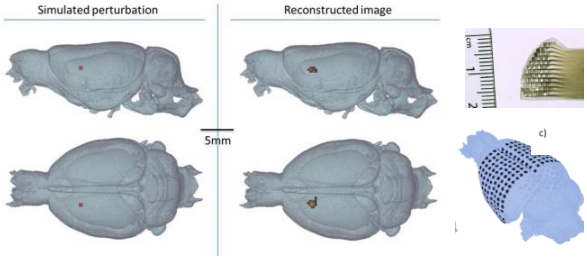

Figure 1: Simulated images reconstructed for a 1% impedance decrease, in the hippocampus using a 6M element mesh for the forward and 500k for inverse problem. Changes throughout the rat brain using 120 electrodes could be reconstructed with an accuracy of <500µm.

2 Methods

2.1 Electrodes

Electrodes were fabricated using laser-cut stainless-steel foil sandwiched between two silicone rubber layers, which was our preferred technique after a previous study comparing two different methods for electrode fabrication [2]. Electrodes were 0.6mm in diameter and 1.3mm apart. One array consisted of 60 channels and used for one hemisphere on the rat brain while its mirrored copy used on the opposite hemisphere.

2.2 EIT recordings

Impedance change recordings associated with evoked potentials were undertaken in an anaesthetised rat with forepaw and whisker stimulations. Two of the 60-channel arrays were implanted directly on exposed cortex. EIT was recorded using a Keithley 6221 current source and Biosemi A/D EEG system.

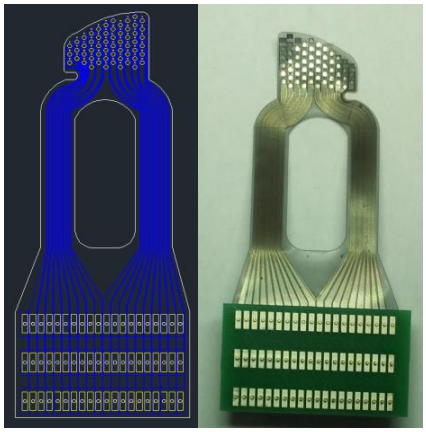

Figure 2: Image of CAD drawing of the 60 channel array (left) and a photograph of fabricated array (right)

3 Results

Electrodes were suitable for surgical application and covered c.90% of the brain. Electrode impedances were all < 800Ω at 100Hz. Satisfactory impedance changes and evoked potentials could be recoded on all channels.

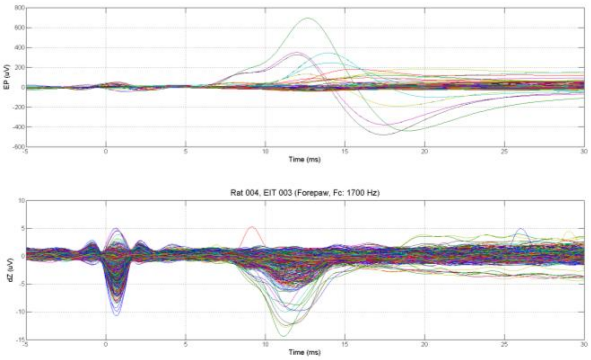

Figure 3: Top panel: recorded evoked potentials, Bottom panel: the corresponding impedance change; Different channels are represented by the different coloured lines.

4 Discussion

A 120-channel electrode system was successfully fabricated and design was optimised for successful and easy surgical implantation. Impedance changes were successfully recorded. Work in progress is to obtain 3D images from recorded impedance changes.

References

[1] Oh et al. *Medical & biological engineering & computing*, 49(5), pp.593–604. 2011.

[2] Koronfel MA et al. Submitted to *Physiological measurements* special issue 2014.

The Data Acquisition Method of the Sussex MK4 EIM System

XiaolinZhang[1], Wei Wang[2] and Chris Chatwin[1]
[1]University of Sussex, Brighton, UK, xz68@sussex.ac.uk
[2]Micro Image UK Ltd, UK, w97wang@yahoo.co.uk

Abstract: The Sussex MK4 electrical impedance mammography (EIM) is an EIT system dedicated to breast cancer detection. The novel electrode configuration with its data acquisition method has significantly enhances the system performance by improving the signal-to-noise ratio (SNR).

1 Introduction

The Sussex MK4 EIM system is a 3D imaging system for breast cancer detection. It permits visualization of the inner structure of the breast by measuring its impedance distribution. The Sussex MK4 is equipped with a planar electrode array. The appearance of the system is a bed with a measurement tank in an appropriate position (Fig. 1a). The diameter of the tank is 18cm. The maximum depth of the tank is 5cm. The planar electrode array is fixed at the bottom of the tank and it is adjustable in the vertical direction. During examination, a patient can lie still in the prone position with a breast in the saline filled tank. This system uses current excitation (1mA peak to peak) and voltage measurement covering frequency from 10kHz to 5MHz. The measurement circuits consist of a switching network, low noise amplifiers and 14-bit ADCs sampling at 100MS/s, the maximum voltage input range is 5V peak to peak[1].

2 Methods

There are 85 electrodes deployed in a hexagonal pattern (Fig. **1**b). The distance between any adjacent electrodes is 17mm. The current excitation and voltage measurements are only focused and achieved in a small hexagonal area (Fig. 1c). In each hexagonal measurement area, there are a maximum of 3 excitation events at 0° , 60° and 120°, (Fig. 2) and in each excitation, there are maximum of 12 voltage measurements, which are collected strictly parallel to the driving pair. With this special type of electrode configuration method, there are 123 excitation events corresponding to 1416 measurements. In all the figures of this paper,the yellow dots indicate the excitation pair; the blue dots connected by red arrows indicate measuring pairs [2] in one excitation.

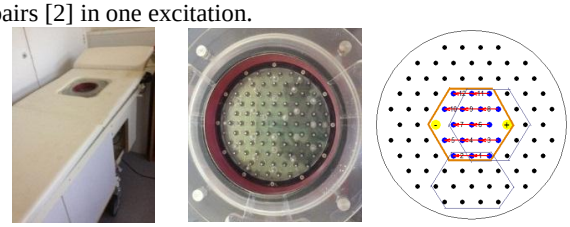

Fig. 1. Sussex MK4 EIM system and planar electrodes. (a) MK4 EIM system. (b) the planer electrodes. (c)the electrode drive and receive hexagon pattern.

The advance of this data acquisition method is gaining the strongest measurements for each excitation to guarantee a much smaller dynamic range (DYR) between the maximum and the minimum measurements in each excitation. Compared with the traditional DAS system in EIT with large DYR, it has achieved a much better overall SNR . Here we provide an example shown in Fig. 3 based on the planner electrode array of the MK4. We name the 12 measurements within the hexagonal measurement area as the inner measurements (IMs) (Fig. 3 (a)) and the 14 additional measurements outside the hexagonal measurement area as the outer measurements (OMs) (Fig. 3 (b)). Fig.4 displays the total 26 measurements shown in Fig**. 3**, which are simulated for a 4.5 cm height of saline with a conductivity of 0.5 mS/cm in the tank. We find that the DYR of the IMs is about 10 times smaller than that of all the 26 measurements including both the IMs and the OMs. Therefore for a 60dB SNR DAS system, the IMs based MK4 data acquisition method has successfully avoided the additional 20dB SNR lost compared with the IMs and OMs based data acquisition method, for a fixed programmable gain amplification (PGA) system.

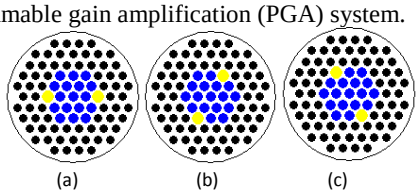

Fig. 2. Three current excitations in a hexagonal area.

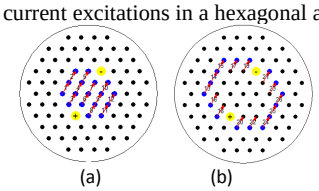

Fig. 3. Measurement pairs.(a) shows the measurements within the hexagonal measurement (IMs) area (b) shows the measurements outside the hexagonal measurement (OMs) area.

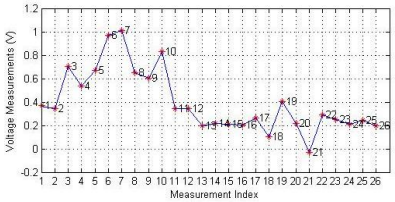

Fig. 4. The voltage measurements corresponding to Fig. 3.

3 Conclusions

The novel hexagonal electrode arrangement and data acquisition method ensures up to 1416 independent measurements with high SNR by effective reducing the DYN without losing the signal in range of interest (ROI) .

References

[1] B. Nevis, "An investigation into combining electrical impedance mammography with 3D ultrasound for breast cancer detection," Doctoral thesis, Engineering and Design, University of Sussex, 2013.

[2] G. Sze, "Detection of breast cancer with electrical impedance mammography," Doctoral thesis, Engineering and Design, University of Sussex, 2012

Iontophoretic Conditioning of the Electrode to Skin Contacts

Pavel Govyadinov[1,2], Amanda Gunn[2], Sergei Turovets[1,2], Don Tucker[2], Phan Luu[2]

[1]Department of Computer Science, University of Oregon, pgovyadi@cs.uoregon.edu
[2]Electrical Geodesics Inc., Eugene, Oregon

Abstract: By utilizing direct current (DC) iontophoretic treatment on electrodes with high impedance we show the effectiveness of iontophoresis as a driving force for permeation of ionic electrolyte into the skin barrier. After a 60 second DC treatment at 50µA or 100µA amplitudes on either saline, Nihon Kohden Elefix, or Agar based electrolytes we saw an immediate impedance drop ranging from 3-30%. The effects generally lasted several hours.

1 Introduction

In early electrophysiological recording, such as electroencephalography (EEG), low electrode-scalp impedance was necessary. In addition to using electrolyte to hydrate the skin, it was common to abrade the scalp to reduce impedance. Although with the advent of modern solid state amplifiers the necessity for low impedance in EEG has almost disappeared [1], transcranial electric stimulation (TES) and other applications like ECG, EMG and EIT still require low impedances to guarantee stable contact. Direct current iontophoresis, the physical process of driving ions through a medium with electrical current [2], is a promising technique for electrical contact conditioning. The goal of this study was to decrease the contact impedance by applying iontophoretic treatment at several amplitudes, with multiple electrolytes and study the short term and long term effects of the procedure.

2 Methods

2.1 Experimental Setup

We employed the multichannel NA 300 amplifier with a built-in Howlan-type DC/AC constant current generator, isolated from the amplifier circuitry, Net Station v4.4.1a1 software, and Ag-Cl coated electrode head EEG net (Electrical Geodesics, Inc) to perform DC iontophoresis. A scanning protocol was used to select electrode pairs (one source, one sink) for treatment and either 50µA or 100µA of DC current was injected through the selected electrodes for a length of 60 seconds. 12-16 electrode pairs were selected for every subject, and were treated with the procedure while the rest of electrodes were left untreated. 2 subjects volunteered for the experiment, with a total of 5 sessions. All hardware complies with the International Electrical Safety Limits.

2.2 Impedance Measurements.

Impedances were measured using the standard impedance checking methods in EGI's NA 300 system [1].

2.3 Electrolyte

Three electrolytes were used: saline electrolyte(1.5 liters of saline, 5ml of shampoo and 15 grams of sodium chloride (NaCl)); Nihon Kohden Elefix Paste (a propylene glycol based paste electrolyte that is FDA cleared and available commercially); Agar-saline based gelatinous electrolyte.

3 Results

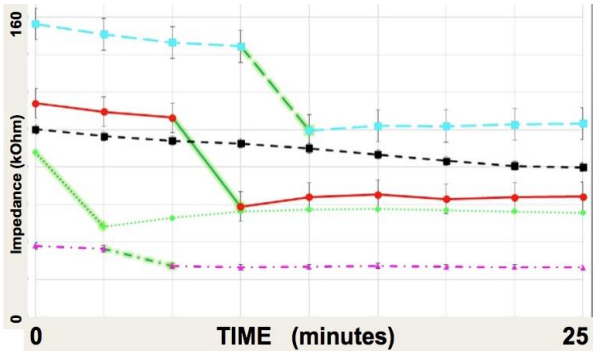

Figure 1: Impedance (kOhms) over time (minutes) of four treated source electrodes (in color) and the mean trend of untreated electrodes (black). The time segments with treatment are highlighted.

We have observed an average 19% impedance drop at the source and 11% impedance drop at the sink electrode immediately after injection with saline, and even larger effects with other electrolytes (Elefix, Fig.1).
Along with DC conditioning, AC treatment at 10KHz frequencies was shown to be effective in lowering impedance [3], suggesting possible future research direction.

References

[1] Ferree, Thomas C., et al. *Clinical Neurophysiology* 112.3 (2001): 536-544.
[2] Prausnitz MR.. Adv. Drug Deliv. Rev. 1996;18:395–425.
[3] Bagniefski, T, Burnette, R. *Journal of controlled release* 11.1 (1990): 113-122.

Table 1: Mean impedance drop at the source and sink electrodes immediately after the treatment for each session and electrolyte. Mean Untreated is the impedance change from the beginning of the session until the end of the session, hence showing the general impedance trend of the electrolyte.

	Saline 1	Saline 2	Elefix	Agar 1	Agar 2
Source, 50µA	-12.63%	-20.46%	-33.56%	-10.12%	-15.38%
Sink, 50µA	-9.93%	-3.41%	-9.86%	-9.03%	-24.06%
Source, 100µA	-18.60%	-23.13%			
Sink, 100µA	-15.82%	-8.40%			
Mean Untreated	0.48%	5.61%	-2.41%	-8.97%	-23.21%

Design of a Microendoscopic EIT Probe: A Simulation Study

Aditya Mahara, Shadab Khan, and Ryan J Halter

Thayer School of Engineering, Dartmouth College, Hanover, NH, USA, e-mail: aditya.mahara.th@dartmouth.edu

Abstract: We describe a simulation study evaluating different electrode configuration for a microendoscopic EIT probe intended to intraoperatively assess surgical margins during radical prostatectomy. In our simulation study, we analyze the performances of three probe designs with varying number of electrodes (8, 9, and 17) and configurations (dependent on number of electrodes).

1. Introduction

There is a significant clinical need to develop a technology to intraoperatively evaluate the pathological status of tissue margins during prostate surgery. Negative surgical margins lead to a significantly decreased rate of recurrence in men treated with radical prostatectomy (RP). We are developing endoscopically-introducible EIT probes to meet this need. Here we describe a microendoscopic EIT probe (Fig. 1) that will be paired with a high speed, high precision modular multi-channel EIT system [1].

Surgical constraints limit the maximum probe diameter to 12 mm (to enable the probe to fit within a laparoscopic port). This defines the design space used for evaluating the number and orientation of probe electrodes. Specifically, the probe was designed to fit as many electrodes as possible within a circular pattern to ensure 1) maximum coverage of the probe tip's active surface and 2) a uniform angular sensitivity. One mm diameter electrodes arranged in circular pattern were therefore chosen for the design. Based on the constraints, three cylindrical probes with 8, 9, and 17 electrodes were considered and evaluated.

Figure 1: Image of a prototype probe.

2. Methods

Simulations were used to evaluate the 3 different probe geometries using a previously described 3-D EIT reconstruction algorithm [2]. Specifically, we were interested in evaluating which probe geometry identified the position and size of an inclusion most accurately. All possible tetrapolar drive patterns were used for the simulations.

2.1 Electrode Configuration

The 3 different electrodes geometries are shown in Fig 2. A 5 mm radius hemisphere represents the tissue being probed. A spherical inclusion of diameter 1mm and conductivity (σ) contrast of 10:1 ($\sigma_{inclusion}$:$\sigma_{background}$) was placed at 17 unique locations spanning the tissue volume. Results and analysis for one representative location are presented.

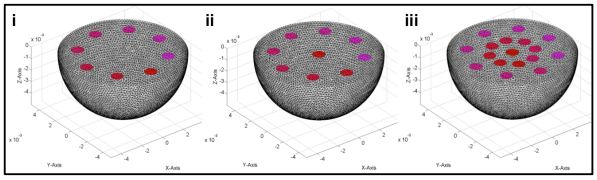

Figure 2: FEM meshes of 8 (i), 9 (ii), and 17(iii) electrode probe designs. The hemisphere represent the tissue volume being probed.

2.2 Simulation Results: Qualitative

For a spherical inclusion centered at (x,y,z) = (1.5mm, 0mm, -0.5mm), the 8 electrode configuration does not accurately identify the position and size, while 9 and 17 electrode configurations provide a more accurate representation (Fig. 3). The 17 electrode configuration provides a better size estimate than the 9 electrode probe.

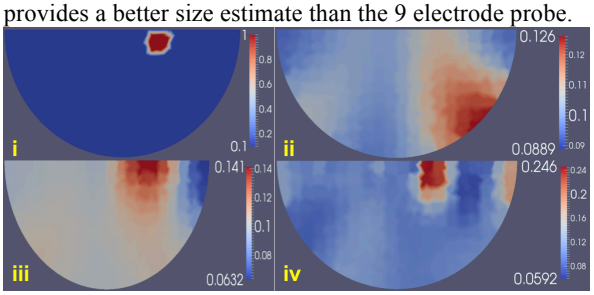

Figure 3. Comparison of 3D absolute reconstruction algorithm in the xz plane for 8, 9, and 17 electrode configuration presented in Fig. 3. ii, ii, iv respectively. An inclusion of diameter 1mm centered at [x,y,z] = [1.5mm,0mm,-0.5mm] is shown in Fig. 3.i.

2.3 Simulation Results: Quantitative

We define the Euclidian distance between the true center of inclusion and the center of the reconstructed volume as the position error (PE). For the inclusion as shown in Fig. 3 the PEs are listed in Table 1; the 8-electrode configuration performs worst while the 17-electrode configuration performs best.

Other quantitative analysis looked at i) the volume error (VE), which is defined as the difference between the true and reconstructed inclusion volume and, ii) noise analysis, in which PE and VE were compared in the presence of Gaussian noise (5 noise levels were explored). In all cases, the 17 electrode configuration performed the best and 8 electrode configuration performed the worst.

Table 1: Position Error in 'mm'

Configuration	**8 electrode**	**9 electrode**	**17 electrode**
Position Error	3.69 mm	0.87 mm	0.49 mm

3. Conclusion

Based on these simulations, a 17 electrode probe performs significantly better than the 8 and 9-electrode configurations. Moving forward, this configuration is being used to design our microendoscopic EIT probe for real-time monitoring of surgical margins.

References

[1] Khan S *et al* In *ICEBI* 2014

[2] Borsic A *et al* In *Phys. Meas*. **31** S1-1, 2010

Application of DICOM in Electrical Impedance Tomography

Alexander Korjenevsky[1], Vladimir Kornienko[1], Vasily Pavluk[2],
Sergey Sapetsky[1] and Timur Tuykin[1]

[1] Kotel'nikov Institute of Radioengineering and Electronics of the RAS, Moscow, Russia, korjenevsky@cplire.ru
[2] Moscow Institute of Physics and Technology, Dolgoprudny, Russia

Abstract: Medical imaging devices including EIT systems are required to be integrated in the clinical information systems. Combining DICOM industrial standard with Open EIT file format can lead to the result, appropriate both to clinical requirements and research community. Successful implementation of the DICOM format for data storage in real EIT system is described here.

1 Introduction

Any medical device pretending to be used in general practice rather than in marginal areas of medicine must be capable of being integrated in the clinical information systems. This supposes compliance with corresponding standards of the data exchange and storage. For the imaging devices such a standard is DICOM (Digital Imaging and Communications in Medicine) [1]. De facto DICOM is the only worldwide used medical data framework, which is adapted even for non-imaging modalities such as electrocardiography. EIT, which makes modest steps in clinical practice and frequently, suffers from lack of this compliance. Customers just refuse to buy equipment if it does not support at least export to the DICOM format. On the other hand, the scientific community needs some common data exchange facilities to share and interpret experimental data. Open EIT initiative is primarily aimed at this task, and the first version of the EIT data storage format is almost ready [2]. Combining industrial DICOM standard with Open EIT internal data arrangement can lead to the result, appropriate both to the requirements of the clinical applications and research community demands.

DICOM is a standard of processing, storage, printing and transmitting information in medical imaging systems. It includes a description of the file format and network protocol. Network protocol uses TCP/IP as the basis for communication among systems. Also systems that support reading and writing DICOM files can simply exchange files in this format. DICOM enables the integration of scanners, servers, workstations, printers, and network equipment of different manufacturers in a single system named PACS (picture archiving and communication system).

2 Methods

In response to many requests from medical community and authorities we have started development of a next software version for the Multifrequency Electrical Impedance Mammography system MEM to achieve DICOM compatibility. MEM is an EIT system with 3D visualization [3, 4]. Before this development the MEM data were stored in a proprietary format, which combines binary and xml data, readable only by the native software.

DICOM is considered sometimes as just a particular image storage format equal to jpeg, png and so on. In fact, the DICOM file is a specialized data base, which can store some mandatory text fields such as patient's social data, equipment and physician identifications, examination conditions as well as binary pixel data including series of images or multiple cross-sections. Every conventional DICOM viewer can extract and display these data. In addition**,** DICOM standard makes provision storing an arbitrary text or binary data in so-called raw data modules in the same file. Format of such raw data entries is wholly specified by the vendor. For example**,** they are used for storing MRI or CT raw measurements to make possible further image reconstructions with different parameters. EIT can use this possibility in the same way: we can store results of electrical measurements and other specific data in the raw data module inside a DICOM file. Certainly, this part of DICOM data is readable only by specialized software.

At the first stage we have implemented the DICOM export and import facilities inside existing MEM software. Corresponding procedures are coded as a dynamically loaded library using resources of DCMTK open source project [5]. The raw data storage part of the library is not device specific, so it can be used with other EIT systems. The next step is transition to using DICOM files instead of our native data storage format. This will make it possible to view and store EIT data in the clinical information system without export/import steps. The further development would be implementation of the DICOM network protocol for direct communication with the data storage servers.

3 Conclusions

DICOM data format has been successfully used in the commercial EIT application as for storage of the general patient data and reconstructed images as well as for EIT specific data storage, including raw measurement results. Because of flexibility of the raw data file module in DICOM format, it is possible to combine it with the Open EIT format suggested by the community. This supposes storing the reconstructed images and general information in the corresponding DICOM modules while encapsulating the rest of Open EIT data in the raw data module instead of zipping them in archive.

References

[1] DICOM standard online. *http://dabsoft.ch/dicom/*
[2] Gaggero PO, et al. In *XIVth Conference on Electrical Impedance Tomography*:92. 2013
[3] Cherepenin V, et al. *IEEE Trans. Medical Imaging* **21**:662 – 667, 2002
[4] Trokhanova OV, Okhapkin MB and Korjenevsky AV. *Physiol. Meas.* **29**:S331-S344, 2008
[5] DCMTK - DICOM Toolkit. *http://dicom.offis.de/dcmtk.php.en*

Using real data to train GREIT improves image quality

Pascal Gaggero[1], Andy Adler[2] and Bartłomiej Grychtol[3]

[1]Bern University of Applied Sciences, Bienne, Switzerland
[2]Carleton University, Ottawa, Canada
[3]German Cancer Research Center, Heidelberg, Germany

Abstract: Image reconstruction in electrical impedance tomography is sensitive to errors in the (forward) model of the measurement system. We propose a new approach, based on the GREIT algorithm, where the reconstruction matrix is trained on real rather than simulated data, obviating the need for an accurate numerical forward model. We observe a substantial improvement in image quality, particularly for changes close to the boundary.

1 Introduction

Traditional approaches to image reconstruction in electrical impedance tomography (EIT) require knowledge of the geometry of the studied domain and characteristics of the measurement system. However, accurate hardware modelling, including all of its imperfections and the interface between the electrodes and the studied domain, is a very difficult task. We present an approach that bypasses the need for an accurate model of the hardware by using real measurement data to calculate a reconstruction matrix based on the GREIT approach [1]. The motivation of the present work is to customize the reconstruction method for a particular configuration of a particular EIT system to improve the accuracy of the reconstructed images.

2 Methods

GREIT is a linear reconstruction algorithm for difference EIT, where the reconstruction matrix is calculated based on a data set of sample measurements from small single-target perturbations and the corresponding desired images [1]. To date, this training data set was generated using numerical simulations. Here, we use a recently developed robotic testing platform for EIT systems [3] to create the training perturbations and record the corresponding measurements in a saline tank. We compare reconstructions of a testing data set (recorded by the same system) obtained with GREIT trained on real data with that trained on equivalent simulated data.

Measurements were acquired on a saline tank (∅ 290 mm, σ=1.6 S/m) with the Pioneer Set (Swisstom, Landquart, Switzerland) with its 32 active electrodes [2] in a single ring around the tank and default settings. Training data were acquired by placing a non-conductive POM ball (∅ 25 mm) in 770 different positions in the plane of the electrodes. Equivalent simulated data were obtained with the `mk_GREIT_model` function in EIDORS using a best-effort FEM model of the tank. Testing data were acquired in 250 positions with a ∅ 45 mm ball.

To compare the reconstructions obtained with GREIT trained on measurements (GREITm) and simulations (GREITs), we used figures of merit adopted from [1]: position error (PE), deformation (DEF), amplitude response (AR) and ringing (RNG).

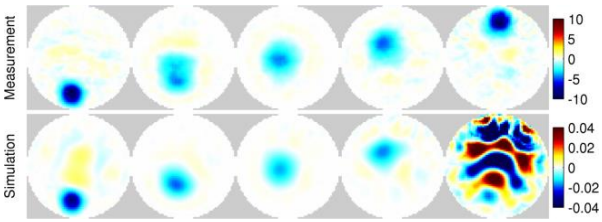

Figure 1: Sample reconstructions with GREIT trained on measurements (top) and simulations (bottom).

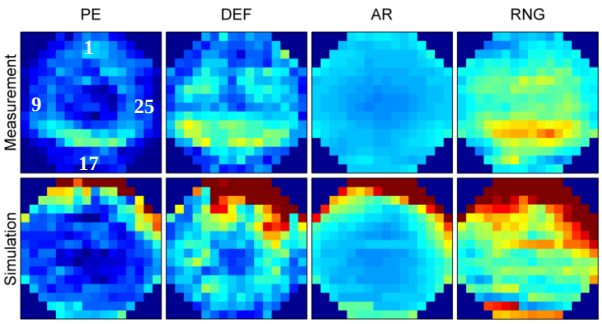

Figure 2: Figure of merit maps. The color scale for both images in a single column is fixed; very high values (red) are cropped.

3 Results

Sample reconstructions of the test data with GREITm and GREITs are presented in Fig. 1. Neither algorithm reconstructs the correct value of the conductivity contrast (about -1.6 S/m). For most target positions, the algorithms show comparable performance. However, for targets in the region delimited by electrodes 5 and 25 (top part of the image), GREITs shows much worse performance. This is reflected in the figure of merit maps (Fig. 2), where GREITs shows deterioration in that region. GREITm is characterised by a more uniform amplitude response and less ringing.

4 Conclusions

Our results support the notion that real measurement data can successfully replace the forward used to calculate the GREIT reconstruction matrix. We interpret the non-uniform performance of GREITs as resulting from hardware setup imperfections, since greatest deterioration was observed for target locations near the end of the electrode belt (electrodes 25 to 32) or where measurement and current stimulation are performed across the belt's ends (electrodes 5 to 25). Future work will address the extent to which tank measurements are helpful in training a GREIT reconstruction matrix for human thorax imaging.

References

[1] A. Adler et al., *Phys Meas* **30**, S35-S55, 2009
[2] P. O. Gaggero et al., *Phys Meas* **33**:831-847, 2012
[3] P. O. Gaggero et al. In *XIVth Int Conf EIT*. 2013

Session 5

Applications II

24 April 2014, 16:15 – 18:00

Slope Stability Monitoring through Impedance Imaging

Alistair Boyle[1], Paul Wilkinson[2], Jonathan Chambers[2], Nolwenn Lesparre[3], Andy Adler[1]

[1]Carleton University, Ottawa, Canada, {boyle,adler}@sce.carleton.ca
[2]British Geological Survey, [3]Institut de Radioprotection et de Sûreté Nucléaire

Abstract: A technique for monitoring slope stability in a geological setting through impedance tomography is demonstrated. An iterative absolute Gauss-Newton solver simultaneously constructs estimates of the underground resistivity distribution and movement of the stimulation and measurement electrodes. The results are a step toward demonstrating that a cost effective and potentially predictive monitoring technology could be practical.

1 Introduction

Slope stability is a key issue for land uses where slope morphology and annual changes in soil and rock water saturation lead to movement. Monitoring of these slip prone regions in the railway, mining, oil and gas, and construction industries is currently available through laser range finding and similar surface observation technologies which can not provide remote, unmanned and cost effective monitoring over time. Slope Stability is important for long term railway embankment safety and for determining mine tailings pile slope angles. To corporations involved in these industries, slope stability translates into a significant risk/cost balance. The challenging task of managing landslide risk may be mitigated to some degree through insight gained from monitoring and understanding the geophysical process.

In sedimentary rock, resistivity is related to water saturation through Archie's Law [1]. A common adaptation of Archie's Law, the Waxman-Smits equation [2], accounts for the effects of clay, common in top soil and non-sedimentary rock, by adding variables that support variation in ion mobility and ion concentration. The geology of a region is relatively fixed on a human time scale, such that completing a lab correlation provides accurate estimates of water saturation and hence, can provide a prediction of slope stability through static slope stability analysis techniques. An accurate and ongoing estimate of electrode movement provides immediate warning of slope movement at a reduced cost compared to the previously mentioned technologies.

2 Reconstruction

Measurements have been taken since 2008 on a slow moving land slide located in the British countryside [3]. An absolute Gauss-Newton iterative solver that simultaneously solves for the combined log conductivity and electrode movement using this data was developed in the EIDORS environment (Figure 1).

An initial background estimate was constructed by finding the best-fit average resistivity of the apparent resistivity measurements. Initial electrode positions were determined via GPS measurements.

The conductivity Jacobian was calculated using the adjoint method for conductivity and scaled for log conductivity using the chain rule.

$$\mathbf{J}_{\ln\sigma} = \frac{\partial \mathbf{b}}{\partial \ln\sigma} = \frac{\partial \mathbf{b}}{\partial \sigma}\frac{\partial \sigma}{\partial \ln\sigma} = \frac{\partial \mathbf{b}}{\partial \sigma}\sigma = \mathbf{J}_\sigma \sigma \qquad (1)$$

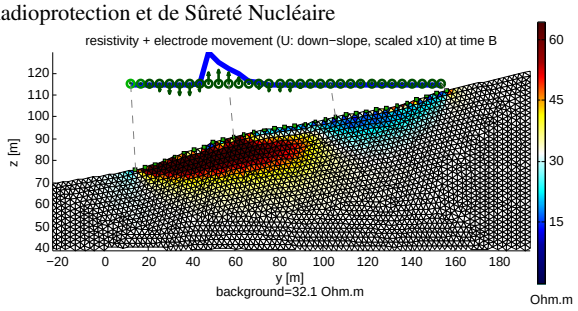

Figure 1: Simultaneous reconstruction of resistivity and electrode movement after 4 Gauss-Newton iterations; green arrows are reconstructed down-slope movement, blue line is measured movement (GPS)

The movement Jacobian [4] was estimated by constructing a down-slope and cross-slope movement perturbation using alternate electrode sites. Alternate electrode sites were preferred over rank-1 updates [5] because rank-1 updates restrict the magnitude of the electrode movements to within a single surface mesh element in the forward model where high mesh density is critical to accurate measurement estimates. Performing movement Jacobian perturbations in this fashion increased the original dipole-dipole stimulation and measurement pairs P_{orig} such that

$$P_M = N_{e\ell} D_{DoF} P_{orig} \qquad (2)$$

where the total stimulation/measurement pairs for movement estimates P_M increased by the number of electrodes $N_{e\ell}$ and movement degrees of freedom M_{DoF}. Many of the calculated measurements required for this approach are redundant across each electrode movement. A generic stimulation and measurement pattern improvement routine was developed to minimize computation time for the forward solutions by rearranging the forward solution results and removing duplicate measurements. This routine improved run times by two-orders of magnitude ($N_{e\ell} = 32$, $D_{DoF} = 2$, $P_M \simeq 37000$) from 45 minutes to 3.75 minutes for the rearrangement and approximately 15 seconds for each new forward solution (Intel Xeon 2.6GHz, 8 cores, 64GB mem.) of which there was one per Gauss-Newton iteration.

3 Discussion

Simultaneous reconstruction of absolute impedance and electrode movement is a practical and promising method for monitoring slope stability. While prior work has reconstructed electrode movement and absolute impedance separately [6], to our knowledge, this is the first time they have been reconstructed simultaneously.

References

[1] Archie GE. *Trans Am Inst Min Metall Pet Eng Inc* **146**(1):54–62, 1942
[2] Waxman M, Smits L. *SPE Journal* **8**(2):107–122, 1968
[3] Chambers JE, Wilkinson PB, Kuras O, et al. *Geomorphology* **125**(4):472–484, 2011
[4] Soleimani M, Gómez-Laberge C, Adler A. *Physiol Meas* **27**(5):S103–S113, 2006
[5] Gómez-Laberge C, Adler A. *Physiol Meas* **29**:S89–S99, 2008
[6] Wilkinson PB, Chambers JE, Meldrum PI, et al. *Geophys J Int* **183**(2):543–556, 2010

Cross-section electrical resistance tomography of La Soufrière of Guadeloupe lava dome

Nolwenn Lesparre[1], Bartłomiej Grychtol[2], Dominique Gibert[3], Jean-Christophe Komorowski[3], Andy Adler[4]

[1]Institut de Radioprotection et de sûreté Nucléaire, Fontenay-aux-Roses, France, nolwenn.lesparre@irsn.fr
[2]German Cancer Research Center, Heidelberg, Germany
[3]Institut de Physique du Globe de Paris, Sorbonne Paris Cité, Univ Paris Diderot, Paris, France.
[4]Carleton University, Ottawa, Canada

Abstract: The electrical resistivity distribution at the base of La Soufrière of Guadeloupe lava dome is reconstructed by using transmission electrical resistivity data obtained by injecting an electric current between pairs of electrodes on opposing sides of the volcano. The data are inverted to perform a slice electrical resistivity tomography (SERT). The resulting image shows the presence of highly conductive regions separated by resistive ridges.

1 Introduction

The La Soufrière volcano has an active eruptive history. Future eruptions are possible, and could have large impacts on surrounding communities. Various scenarios are possible: collapse, phreatic eruption, magma ascent [1]. To give early warning, multi-parameter monitoring is conducted by the local volcano observatory (IPGP/OVSG). Complementary geophysical studies are then necessary to obtain a view of the inner structure of the volcano in order to better understand the monitoring data. The present study aims at contributing to the knowledge of the lava dome interior by performing a slice electrical resistivity tomography (SERT) obtained by inverting an electrical resistivity data set. The data set considered here was acquired with a transmission tomography configuration in order to probe the innermost regions of the lava dome [2].

2 Methods

Data were acquired at 62 electrodes attached to a 945 m long main cable. One of the cable extremities was connected to an auxiliary long wire in order to place an electrode on the opposite side of the lava dome. Both the remote electrode and one electrode plugged onto the main cable were used to inject an electric current forced to cross the innermost parts of the volcano. The main cable was moved to successively occupy three circular segments surrounding La Soufrière lava dome to form an almost closed loop. The elevations of the electrode loop vary between 1146 and 1337 m with an average of 1270 m, *i.e.* about 200 m bellow the summit.

We performed a SERT to reconstruct the conductivity distribution in a cross-section limited by the ring of electrodes. The SERT was implemented by defining the unknown conductivity distribution σ_{2d} on a coarsely meshed 2D cross-section. σ_{2d} was subsequently used to construct the full 3D conductivity distribution σ_{3d} necessary to solve the forward 3D finite element model. This was achieved by using a coarse-to-fine matrix that maps the conductivity σ_{2d} of each element of the cross-section onto each of the elements of the 3D model.

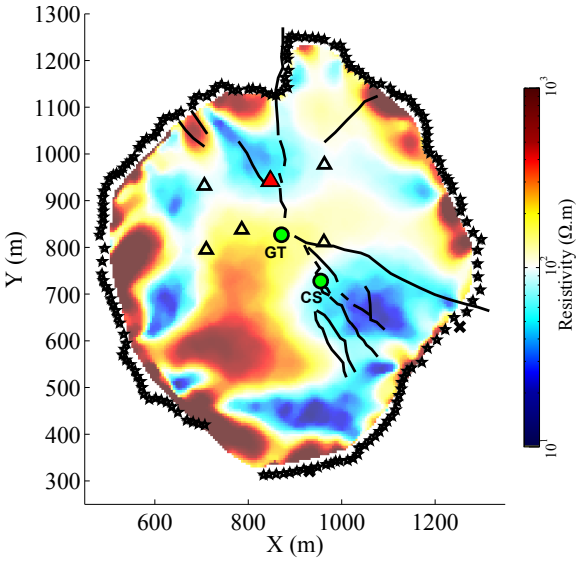

Figure 1: Reconstruction of the electrical resistivity at the dome base. Stars represent the electrodes location. Main geological structures are reported such as fractures (black lines), peaks (triangles) and acid ponds (green circles). The summit of La Soufrière is in red.

3 Discussion

The reconstructed resistivity cross-section shows that the interior of the lava dome contains three main conductive domains and one resistive structure (Fig. 1). Considering the resistivity values of these structures together with the densities obtained by cosmic muon radiography [3] we interpret the conductive regions as reservoirs filled with unconsolidated material and conductive hydrothermal fluids. This description is coherent with the activity observed during the successive phreatic eruptions that occurred since the creation of the lava dome 500 years ago.

Similarly, the resistive region is interpreted as a massive lava body that vertically extends through the whole height of the lava dome and which seems to constitute a barrier that, up to now, blocked eruptive activity on the south-west flank of the volcano.

References

[1] Komorowski, JC, Legendre, Y, Caron, B & Boudon, G. J. Volcanol. Geotherm. Res., **178**(3): 491–515, 2008.
[2] Nicollin, F, Gibert, D, Beauducel, F, et al.. *Earth Planet. Sc. Lett.*, **244**(3): 709–724, 2006.
[3] Lesparre, N, Gibert, D, Marteau, J, et al. *Geophys. J. Int.*, **190**(2), 1008–1019, 2012.

Impedance-Cystovolumetry from Multifrequency Electrical Impedance Tomography

Jakob Orschulik, Thomas Schlebusch, Steffen Leonhardt

Chair for Medical Information Technology, RWTH Aachen University,

Pauwelsstr. 20, D-52074 Aachen, Germany, orschulik@hia.rwth-aachen.de

Abstract: The objective of impedance-cystovolumetry is the continuous, non-invasive monitoring of bladder volume. By using electrical impedance tomography, a correlation between the change of impedance in the image and bladder volume can be found. However, the typically used time-differential approach has the problem of both requiring a calibration measurement with an empty bladder and being dependent on the urine conductivity. This paper presents an improvement to the time-differential approach using multi-frequency electrical impedance tomography.

1 Introduction

The continuous monitoring of the bladder volume is of great interest to patients with paraplegia as they have to empty the bladder manually using catheterization. Currently, this is done using a fixed-time scheme. To allow a demand driven catheterization, a continuous monitoring is necessary.

2 Methods

One possibility for the estimation of the bladder volume from electrical impedance tomography is the global impedance method. After reconstructing an image using the GREIT-algorithm [1], all pixel values are summed up. To retain phase information, both data acquisition and image reconstruction are performed in the complex domain. Previously it was shown, that this sum over all pixel values and the bladder volume correlate with each other [2]. However, the time-differential approach that has been used has the two problems of requiring a reference measurement with an empty bladder as well as being dependent on the urine conductivity. Thus, a frequency-differential approach is examined, where the measurements are performed nearly simultaneously using frequencies of 51.8 kHz and 100 kHz. Since the urine conductivity is not frequency dependent in our frequency range, the reconstructed impedance change in this area is zero. In contrast, the impedance of muscle or fat is frequency dependent. As a full bladder displaces more tissue than an empty one, the global change of impedance in the tomogram correlates with the bladder volume while being independent of urine conductivity.

2.1 Simulation

The simulation was performed in Matlab using the EIDORS-framework [3]. The finite element model consists of a cylinder inside of a tank with 8 electrodes. The conductivity of the environment was simulated as complex, frequency dependent muscle tissue according to the tissue database from Gabriel & Gabriel [4]. In contrast, the urine conductivity was simulated using frequency independent values in the physiological range of 12–28 mS/cm.

2.2 Measurement

The real measurement was performed using an agar-agar model inside a tank similar to the simulation. To simulate the bladder, holes were cut into the model and filled with distilled water (0 mS/cm), 0.9 % saline (approx. 16 mS/cm), and 1.8 % saline (approx. 30 mS/cm).

3 Results

To analyze the influence of urine conductivity, a calibration curve was calculated based on the data at a reference conductivity of 20 mS/cm in the simulation and 0.9 % saline in the measurement. Then, the mean of the relative error $\bar{\varepsilon}_r$ and the standard deviation σ_{ε_r} between the data at other conductivities and the calibration curve were calculated. A comparison between the time-differential and the multifrequency approach is shown in Table 1. The simulation results show an improvement regarding the impact of urine conductivity on volume estimation as the average error decreases significantly compared to the time-differential approach. Furthermore, the standard deviation improves as well. This simulation results were verified in the agar-agar measurement.

4 Conclusion

Multifrequency impedance tomography for impedance-cystovolumetry is a very promising approach as it provides urine conductivity independent results. In addition, no empty bladder reference measurement is required taking the concept one step further towards clinical use.

References

[1] Adler A, Arnold JH, Bayford R, et al. *Physiological Measurement* **30**(6):S35, 2009

[2] Leonhardt S, Cordes A, Plewa H, et al. *Biomedizinische Technik/Biomedical Engineering* **56**(6):301–307, 2011

[3] Adler A, Lionheart WRB. *Physiological Measurement* **27**(5):S25, 2006

[4] Gabriel S, Lau R, Gabriel C. *Physics in medicine and biology* **41**(11):2251, 1996

Table 1: Mean relative error $\bar{\varepsilon}_r$ and its standard deviation σ_{ε_r} in simulation and measurement with different urine conductivities. Both in simulation and measurement the time-differential (TD) and multifrequency (MF) results are compared.

simulation					measurement				
σ (mS/cm)	TD		MF		saline conc.	TD		MF	
	$\bar{\varepsilon}_r$ (%)	σ_{ε_r} (%)	$\bar{\varepsilon}_r$ (%)	σ_{ε_r} (%)		$\bar{\varepsilon}_r$ (%)	σ_{ε_r} (%)	$\bar{\varepsilon}_r$ (%)	σ_{ε_r} (%)
12	-27.46	1.50	-6.26	0.73	0.0 %	-18.24	15.76	2.87	8.54
28	13.92	1.07	2.15	0.40	1.8 %	13.45	10.39	9.45	10.07

Continuous non-destructive conductivity monitoring of chondrogenesis using bioimpedance tensor probe

Geuk Young Jang[1], EunAh Lee[2], Hun Wi[1], Eung Je Woo[1] and Tong In Oh[1]

[1]Department of Biomedical Engineering, Kyung Hee University, Yongin, Republic of Korea, tioh@khu.ac.kr
[2]College of Life Science and Graduate School of Biotechnology, Kyung Hee University, Yongin, Republic of Korea

Abstract: A continuous non-destructive monitoring method is required to apply proper feedback controls during chondrogenesis. We measured the apparent conductivity and the amount of anisotropy on the top and bottom surfaces of samples in the chondrogenesis process to evaluate the ECM structure and composition changes. We compared them with histological trait to analyse the results.

1 Introduction

There are many reports to demonstrate that nerve or tissue regeneration is a successful treatment modality in skin, muscle, nerve and periodontal reconstruction. Implantation of tissue engineered cartilage replacing degenerated cartilage tissue is expected to show the normal cartilage function shortly with reference to other methods [1]. In order to control the quality of productions, non-destructive, continuous monitoring and proper feedback control based on monitoring results are required during chondrogenesis. We considered that the conductivity of cartilage after formation was quite different from the conductivities of chondrocytes and stem cell growth medium. Additionally, the cellularity and contents in the extracellular matrix (ECM) structure are different depending on the zonal organization as shown in Figure 1 [2]. In this study, we observed the apparent conductivity and anisotropic conductivity on the top and bottom surfaces related with different ECM compositions and structures in the chondrogenesis process.

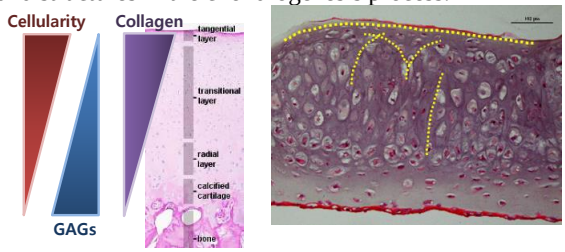

(a) (b)

Figure 1: (a) Structure of depth-dependent ECM components in articular cartilage and *in-vitro* constructed cartilage.

2 Methods

Fragments of costal cartilages were obtained from lower false rib of 3-4 month old New Zealand White rabbits [3]. Perichondrium was extracted from cartilage tissue and minced. We filtered the digested cartilage in 0.5% collagenase type I with Mesenchymal stem cell growth medium. *In-vitro* expanded chondrocytes were seeded in a Millicell cell culture inserts in order to construct disc-type cartilage.

We used the bioimpedance tensor probe employing a conductivity estimation algorithm with 16 electrodes to eliminate the geometrical effects and accurately measure the tissue conductivity and its degree of anisotropy [4]. For 6 weeks, we measured conductivity and the ratio of eigenvalue to estimate the degree of anisotropy. We could not measure conductivity on the bottom surface before two weeks because chondrocyte was not formed as the gel type.

3 Results

Conductivities on the top and bottom surfaces were decreased by the time continuously. Even though the thickness of the sample was not increased much after 4 weeks, the conductivity was changed. Also, we can clearly discriminate the top and bottom after 2 weeks. This difference may be caused by the ECM compositions. The ratio of eigenvalue also differed between them after 3 weeks. It revealed that the ECM had different shape in the depth-dependent stratified structure.

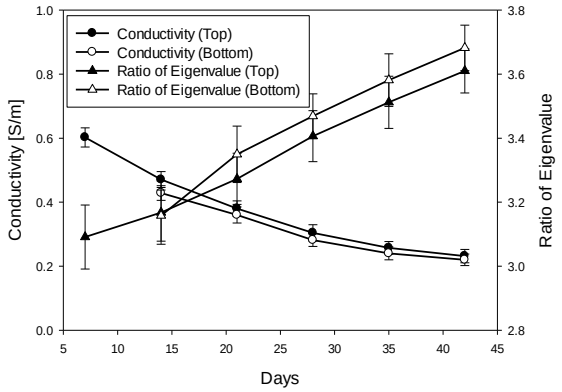

Figure 2: Variation of conductivity and the ratio of eigenvalue during chondrogenesis (6 weeks).

4 Conclusions

Tissue or nerve regeneration is the most promising treatment to replace and heal the functionality inside the body. However, it requires a continuous, non-destructive, and label-free monitoring method for proper feedback controls to improve the productivity and the quality of the final implant. Impedance characterisation will be a feasible technique for tissue regeneration monitoring.

References

[1] Brittberg M, Lindahl A, Nilsson A, Ohlsson C, Isaksson O, Peterson L. *New Eng J Med* **331**: 889-895, 1994
[2] Kock L, van Donkelaar CC, Ito K. *Cell Tissue Res* **347**: 613-627, 2012
[3] Lee J, Lee E, Kim H, Son Y. *Biotechnol Appl Biochem* **48**: 149-158, 2007
[4] Kwon H, Wi H, Karki B, Lee EJ, McEwan A, Woo EJ, Harrach B, Seo JK and Oh TI. *Electron Lett* **48**: 1253-1255, 2012

High-resolution imaging of fast neural activity in the brain with Electrical Impedance Tomography

K. Aristovich*[1], B. Packham*[1], G. Santos[1], H. Koo[1] and D. Holder[1]

[1]University College London, London, UK (* equal contributors)

k.aristovich@ucl.ac.uk, brett.packham.09@ucl.ac.uk

Abstract: We present the first EIT images of evoked physiological activity in the primary somatosensory cortex (S1) obtained with intracranial planar electrode array. Images were validated using intrinsic signal optical imaging (ISOI) and current source-sink density analysis (CSDA). Detailed high-resolution spatiotemporal connectivity of the brain cortex was reconstructed with ≤200μm and ≤2ms.

1 Introduction

There is great interest in imaging functional connectivity in the brain using methods such as functional MRI and optical imaging, but no technique currently exists that could image neural activity over milliseconds throughout the whole brain. Electrical impedance tomography has the potential to image neural activity throughout the brain by recording impedance decreases due to the opening of ion channels during neuronal depolarization [2]

2 Methods

EIT images of evoked physiological activity in the cerebral cortex were reconstructed using the data collected with a 30-electrode epicortical planar array, 7x5mm, placed over primary somatosensory cortex (S1); activity was elicited by mechanical whisker stimulation in the anaesthetised rat.

ISOI was recorded together with simultaneous local field potentials, and further CSDA analysis were undertaken and directly compared with EIT images.

Functional connectivity was then extracted from impedance images using dynamic analysis, and connectivity maps in the whisker barrel cortex were computed for two separate whisker groups.

3 Results

Impedance images showed somatotopically separate activity, which was validated with intrinsic optical imaging. Simultaneous electrophysiological recordings revealed correlation between EIT and current source-sink density analysis for activity onset time (r=0.6, P<0.001), peak amplitude (r=0.9, P<0.001), and depth of activity onset (815±80 um deep for both methods). Functional connectivity was extracted from impedance images using dynamic analysis, revealing the depth of largest lateral spread at 450±40 um.

The trajectory of neural activity, imaged throughout S1 with a resolution of ≤200μm and ≤2ms, entered at layer IV and passed to extragranular layers over ~3 ms; the greatest lateral spread, up to 1.5 mm, occurred in supragranular layers, predominantly along barrel rows (figure 1).

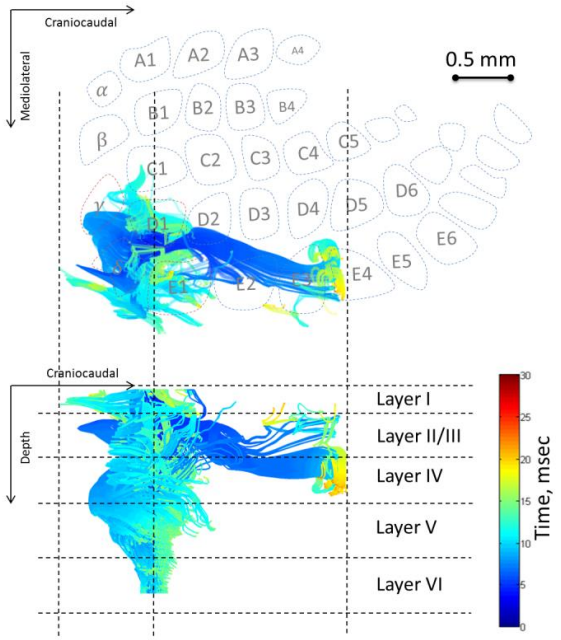

Figure 1: Functional connectivity in the somatosensory cortex of the rat in response to mechanical stimulation of a group of four whiskers ($\gamma, \delta, E1,$ and $D1$). Activity is shown in two isometric views. The top view, superimposed with the map of whisker barrel cortex (top figure), shows lateral propagation of activity to adjacent whisker barrels along the rows. The side view (bottom figure) displays the interlaminar propagation across layers: activity comes in the middle of layer IV, propagates into supra- and infra-granular layers within the stimulated barrels, and then spreads to adjacent whisker barrels predominantly through layers II/III. Timing of activation over milliseconds is colour-coded.

4 Conclusions

Our results demonstrate that EIT can image neural activity throughout the mammalian cerebral cortex with reduced invasiveness, greater resolution and imaging volume (70 mm^3) than other methods. Modelling indicates similar resolutions are feasible throughout the entire brain so that this technique, uniquely, has the potential to image functional connectivity of cortical and subcortical structures.

References

[1] Holder,D.S. Electrical Impedance Tomography: Methods, History and Applications. (Taylor & Francis, 2004).

[2] Oh,T., Gilad,O., Ghosh,A., Schuettler,M. & Holder,D.S. A novel method for recording neuronal depolarization with recording at 125-825 Hz: implications for imaging fast neural activity in the brain with electrical impedance tomography. Med.Biol.Eng.Comput. 49,593–604(2011).

Multi-channel EIT for layer-based hydration monitoring

Xiaohui Chen, Tzu-Jen Kao, Jeffrey Ashe, Gregory Boverman, James Sabatini, David Davenport

GE Global Research Center, One Research Circle, Niskayuna, NY, USA, chenx@ge.com

Abstract: Accurate monitoring of hydration level in patients remains a major challenge for hemodialysis therapy. Using a prototype EIT system with simultaneous multi-channel current excitation, we demonstrated the capability to detect a difference of 35ml daily fluid change in human subjects who wear compression sock only on one leg. The prototype system has the potential to be used in clinical settings with hydration monitoring needs.

1 Introduction

Fluid balance is of great importance for hemodialysis therapy. Poor assessment of hydration status during hemodialysis can lead to under- or over- hydration in patients with consequences of increased morbidity and mortality. In current practice, fluid management is largely based on clinical assessments to estimate dry weight. Since hemodialysis patients usually have co-morbidities that can make the signs of fluidic status ambiguous, dry weight estimation remains a major challenge for hemodialysis therapy[1].

EIT has emerged as a non-invasive method for hydration monitoring. Conventional EIT hydration monitoring systems employ single-channel current excitation to extract hydration information from bulk tissue. In the present study, a prototype GE GENESIS EIT system with multi-channel current excitation was used to enable layer-based hydration monitoring in human legs with minimal interference from skin artifacts.

2 Methods

2.1 Experiment protocols

Proof-of-concept experiment in chicken breast

We injected conductive saline mixed with food dye into different depths of a chicken breast positioned on top of a linear eight-electrode array, impedance change was recorded during the injection process.

Healthy human subject experiment protocol

Healthy subjects reported to the lab at the beginning of their workday. We placed 8-electrode linear arrays on the outside calf of each leg. Multiple current patterns were applied to each leg and impedance measurements were recorded. Volume of each leg was recorded by weighing the amount of water displaced from an edema gauge. The subjects were asked to wear one compression sock on one leg and return to their normal daily work. At the end of the workday, the subjects returned to the lab where the compression sock was removed and measurements of impedance and volume on both calves were repeated.

2.2 Reconstruction algorithms

A linear reconstruction algorithm is used to extract impedance differences due to fluid changes as previously described.[2,3]

3 Results and conclusions

3.1 Detection of layer-based hydration change in chicken breasts

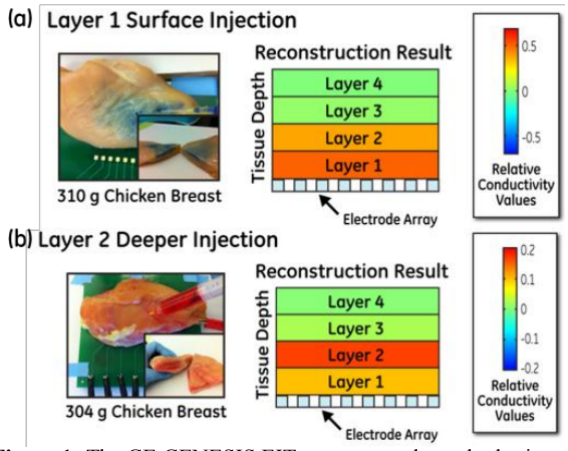

Figure 1: The GE GENESIS EIT system can detect hydration change at different tissue layers in a chicken breast. (a) Surface tissue layer injection; (b) deeper tissue layer injection.

3.2 Detection of layer-based hydration change in human subjects

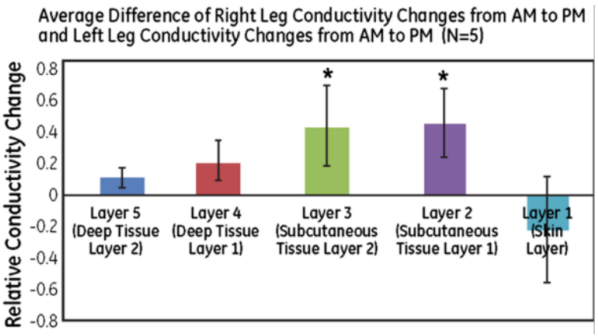

Figure 2: Multi-channel EIT can detect layer-based hydration difference between two legs induced by compression sock

3.3 Conclusion

The multi-channel EIT prototype system offers layer-based hydration monitoring in human subjects.

References

[1] Lindley, Elizabeth, Lynne Aspinall, Claire Gardiner and Elizabeth Garthwaite. 2011. Management of Fluid Status in Haemodialysis Patients: The Roles of Technology and Dietary Advice, Technical Problems in Patients on Hemodialysis.

[2] Mueller JL, D Isaacson D, Newell JC, A reconstruction Algorithm for Electrical Impedance Tomography Data Collected on Rectangular Electrode Array" IEEE Trans. Biomed. Engr., 46(11): 1379-1386, 1999

[3] Kao TJ, Isaacson D , Newell JC, and Saulnier GJ, A 3D reconstruction algorithm for EIT using a handheld probe for breast cancer detection, Physiol Meas. 2006 May; 27(5): S1–11

Session 6

Special Lungs Session

25 April 2014, 8:00 – 9:30

Recent advances in thoracic imaging by electrical impedance tomography

Inéz Frerichs

Department of Anaesthesiology and Intensive Care Medicine, University Medical Centre Schleswig-Holstein, Campus Kiel, Kiel, Germany, inez.frerichs@uksh.de

Abstract: Thoracic imaging by electrical impedance tomography (EIT) is one of the most promising research fields dedicated to this non-invasive imaging technology. Important advances have been achieved mainly in the EIT use for monitoring regional lung ventilation and aeration in critically ill patients. In these patients, the bedside EIT use is expected to improve the ventilator therapy and reduce the ventilator-associated lung injury.

1 Introduction

Thoracic imaging has been identified as one of the most relevant medical applications of EIT already in the early phases of its development [1]. Since then, important experimental and clinical validation studies have been performed showing that EIT is capable of correctly detecting regional changes in lung volumes in both healthy and injured lungs under a variety of ventilation conditions. Various established imaging modalities like computed tomography (CT) [2], electron beam CT [3], xenon multidetector-row CT [4], positron emission tomography [5] or hyperpolarised helium magnetic resonance imaging [6] were used as reference techniques in these studies.

In the future, EIT-derived information on regional lung function might be routinely utilized in a clinical setting mainly in mechanically ventilated patients and in patients suffering from both restrictive and obstructive lung diseases. Recent studies EIT studies confirm this development.

2 Recent advances

Significant progress has been achieved with respect to the use of EIT for monitoring regional lung ventilation and aeration during mechanical ventilation. Findings from experimental studies [7,8] as well as clinical data obtained in patients of all age groups (neonatal, paediatric and adult patients) [9,10] imply that EIT might potentially be used as a bedside tool for individualized guidance of ventilator therapy.

Recent studies revealed that the use of specific ventilation manoeuvres like quasistatic low-flow inflation and deflation [11, 12], stepwise increase and decrease of airway pressure [13], positive end-expiratory pressure (PEEP) trial [14] performed during thoracic EIT examination may increase the information content of the acquired EIT data. Simultaneous sampling of EIT data with other relevant signals (e.g. airway pressure, air flow and volume) enables the assessment of regional respiratory system mechanics [3,13-16]. The choice of PEEP, tidal volume and other ventilator settings using the EIT-derived measures of respiratory system mechanics could result in the selection of the least aggressive ventilation mode and at the same time secure adequate gas exchange. Patients with infant or adult respiratory distress syndrome with already injured lung tissue might particularly benefit from this type of EIT monitoring.

The advantages of regional lung function assessment using EIT have recently also been documented in another group of patients suffering from obstructive lung diseases like chronic obstructive lung disease [17], cystic fibrosis [18] or asthma. EIT examinations accompanying conventional pulmonary function testing by spirometry and whole body plethysmography may provide additional information on the heterogeneity of regional lung function and its changes during disease progression or in response to therapy.

3 Conclusions

The cited but also many other recent studies document the achieved progress in EIT use for thoracic imaging. The present time in EIT research can be characterized as the transition time between experimental and established, clinically used technology. However, this time bears not only possibilities for EIT but also risks, as identified in a recent review summarizing the current state of EIT development and its future challenges [19].

The prerequisites for the clinical acceptance of EIT are the definition of standardized examination procedures, the use of unified nomenclature and interpretation schemes. The EIT measures most relevant for clinical decision-making need to be agreed on. The EIT findings have to be combined with the findings generated by other medical examination tools to render diagnoses on which later therapy can be based on. Further future challenges for EIT are the currently lacking large clinical trials and limited experience with long-term EIT use. To increase the robustness and applicability of EIT further technological development and reduction of interference through other medical devices [20] are mandatory. The success of EIT in a clinical setting will rely on an interdisciplinary approach in EIT research.

References

[1] Brown BH et al. *Clin Phys Physiol Meas* **6**:109-121, 1985
[2] Victorino JA et al. *Am J Respir Crit Care Med* **169**: 791-800, 2004
[3] Frerichs I et al *J Appl Physiol* **93**: 660–666, 2002
[4] Elke G et al. *Physiol Meas* **34**: 1303-1318, 2013
[5] Richard JC et al. *Crit Care* **13**: R82, 2009
[6] Dunster KR et al. *Biomed Eng Online* **11**: 68, 2012
[7] Gómez-Laberge C et al. *Physiol Meas* **34**: 163-177, 2013
[8] Wolf G et al. *Crit Care Med* **41**: 1296-1304, 2013
[9] Miedema M et al. *J Pediatr* **162**: 691-697, 2013
[10] Blankman P et al. *Intensive Care Med* **39**: 1057-1062, 2013
[11] Frerichs I et al. *Physiol Meas* **34**: 567-577, 2013
[12] Pulletz S et al. *J Crit Care* **27**: 323 e311-328, 2012
[13] Pulletz S et al. *Multidiscip Respir Med* **7**:44, 2012
[14] Dargaville P et al. *Intensive Care Med* **36**: 1953-1961, 2010
[15] Lowhagen K et al. *Minerva Anestesiol* **76**: 1024-1035, 2010
[16] Zick et al. *PLoS One* **8**: e72675, 2013
[17] Vogt B et al. *J Appl Physiol* **113**: 1154–1161, 2012
[18] Zhao Z et al. *Physiol Meas* **34**: N107–N114, 2013
[19] Adler A et al. *Physiol Meas* **33**: 679–694, 2012
[20] Frerichs I et al. *Physiol Meas* **32**: L1–L10, 2011

Progress in Perfusion Imaging with EIT

Steffen Leonhardt

Philips Chair for Medical Information Technology , Helmholtz Institute for Biomedical Engineering , RWTH Aachen University
Pauwelsstr. 20, D-52074 Aachen, Germany, leonhardt@hia.rwth-aachen.de

Abstract: There is significant interest in the use of EIT to detect and monitor the changes induced by perfusion, however, such measurement presents various technical difficulties. This talk focuses on recent progress in perfusion imaging with EIT.

Perfusion Imaging with EIT

Electrical Impedance Tomography (EIT) shows clinical promise for its ability to image air and fluid flows in the thorax. Perfusion-related changes reflect the behaviour of the cardiovascular system, and thus can convey many clinically important variables for patient management.

Since perfusion-related changes in thoracic impedance are much smaller than the impedance changes induced by ventilation, it is much more difficult to use electrical impedance tomography to extract information on stroke volume (SV), cardiac output (CO), or lung perfusion. In order to use the cardiac-related impedance information provided by EIT to quantify cardiac output and lung perfusion, several approaches have been presented in the literature, including a.) Separation of cardiac- and ventilation-related EIT signals based of frequency-domain filtering, b.) ECG gating, c.) Apnea methods, d.) Use of contrast agents and e.) Separation based on principal component analysis. After the overview, the talk will focus on recent results obtained from pig trials by using our PCA-based separation method, as soon available in [1]. One aspect here will be mixed-models analysis versus trend-monitoring.

In order to provide a background for the reader interested in further exploring the literature on perfusion imaging with EIT, we provide a selection of relevant references [2]–[17].

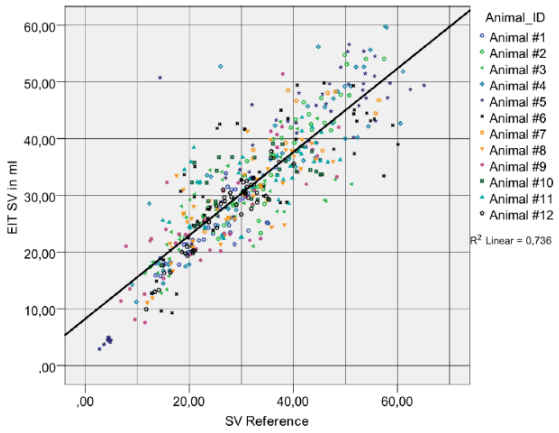

Figure 1: Overall mixed-models-correlation (r = 0.85, r2 = 0.736) for SV estimation using PCA-separated EIT information and transthoracic thermodilution as a reference. To avchieve this result, SV_EIT data had to be calibrated against SV_TTD in each single maneuver. From [1].

References

[1] R. Pikkemaat, S. Lundin, O. Stenqvist, S. Leonhardt, (2014) "Recent advances in and limitations of cardiac output monitoring by means of electrical impedance tomography", Anesthesia & Analgesia, in print.

[2] Borges JB, Suarez-Sipmann F, Bohm SH, Tusman G, Melo A, Maripuu E, Sandstrom M, Park M, Costa EL, Hedenstierna G, Amato M (2012). Regional lung perfusion estimated by electrical impedance tomography in a piglet model of lung collapse. J Appl Physiol 112:225–236.

[3] Carlisle HR, Armstrong RK, Davis PG, Schibler A, Frerichs I, Tingay DG (2010). Regional distribution of blood volume within the preterm infant thorax during synchronised mechanical ventilation. Intensive Care Med 36:2101–2108.

[4] Deibele J, Luepschen H, Leonhardt S (2008). Dynamic separation of pulmonary and cardiac changes in electrical impedance tomography. Physiol Meas 29:1–14.

[5] Eyueboglu B, Brown B (1988). Methods of cardiac gating applied potential tomography. Clin Phys Meas 9:43–48.

[6] Fagerberg A, Stenqvist O, Aneman A (2009). Monitoring pulmonary perfusion by electrical impedance tomography: an evaluation in a pig model. Acta Anaesthesiol Scand 53:152–158.

[7] Fagerberg A, Stenqvist O, Aneman A (2009). Electrical impedance tomography applied to assess matching of pulmonary ventilation and perfusion in a porcine experimental model. Crit Care 13:R34.

[8] Frerichs I, Pulletz S, Elke G, Reifferscheid F, Schadler D, Scholz J, Weiler N (2009). Assessment of changes in distribution of lung perfusion by electrical impedance tomography. Respiration 77:282–291.

[9] Kerrouche N, McLeod C, Lionheart W (2001). Time series of EIT chest images using singular value decomposition and Fourier transform. Physiol Meas 22:147–157.

[10] Leathard AD, Brown BH, Campbell J, Zhang F, Morice AH, Tayler D (1994). A comparison of ventilatory and cardiac related changes in EIT images of normal human lungs and of lungs with pulmonary emboli. Physiol Meas 15:137–146.

[11] Luepschen H, Muders T, Pikkemaat R, Meier T, Putensen C, Leonhardt S (2010). Bestimmung der Lungenperfusion mittels Elektrischer Impedanztomographie. Rostock, Germany, pp 5–8 (in German).

[12] Smit HJ, Handoko ML, Vonk Noordegraaf A, Faes TJ, Postmus PE, de Vries PM, Boonstra A (2003). Electrical impedance tomography to measure pulmonary perfusion: is the reproducibility high enough for clinical practice? Physiol Meas 24:491–499.

[13] Smit HJ, Vonk-Noordegraaf A, Marcus JT, Boonstra A, de Vries PM, Postmus PE (2004). Determinants of pulmonary perfusion measured by electrical impedance tomography. Eur J Appl Physiol 92:45–49.

[14] Smit HJ, Vonk-Noordegraaf A, Boonstra A, de Vries PM, Postmus PE (2006). Assessment of the pulmonary volume pulse in idiopathic pulmonary arterial hypertension by means of electrical impedance tomography. Respiration 73:597–602.

[15] Vonk-Noordegraaf A, Kunst PW, Janse A, Marcus JT, Postmus PE, Faes TJ, de Vries PM (1998). Pulmonary perfusion measured by means of electrical impedance tomography. Physiol Meas 19:263–273.

[16] Vonk-Noordegraaf A, van Wolferen SA, Marcus JT, Boonstra A, Postmus PE, Peeters JW, Peacock AJ (2005). Noninvasive assessment and monitoring of pulmonary circulation. Europ Respir J 25:758–766.

[17] Zadehkoochak M, Blott BH, Hames TK, George RF (1992). Pulmonary perfusion and ventricular ejection imaging by frequency domain filtering of EIT images. Clin Phys Meas 13:191–196.

EIT and the infant lung and respiratory transition at birth – current state and future potential?

David Tingay[1,2,3]

[1]Neonatal Research, Murdoch Childrens Research Institute, Melbourne, Australia. [2]Neonatology, Royal Children's Hospital, Melbourne, Australia. [3]Dept of Paediatrics, University of Melbourne, Melbourne, Australia

Abstract: Theoretically, EIT holds immense potential in the neonatal lung, where traditional 'gold-standard' techniques in adults are either impractical or harmful. This presentation will critically appraise the potential uses of EIT in the neonatal population, the current state of the literature and detail new advances in EIT that highlight the potential of EIT to guide therapy in this vulnerable population, especially at birth.

1 Discussion

Compared to the adults, monitoring lung function in the infant and neonatal lung is problematic due to smaller and variable patient size, patient compliance, rapidly changing lung mechanics, small absolute values in recorded data, especially tidal volume, faster breathing and cardiac rates[1] and a move towards non-invasive respiratory support. Despite this, there is a great need for accurate lung function monitoring. Optimising respiratory support in a critically ill neonate is more likely to result in better long term outcomes than in diseased adults[2]. EIT has been long proposed as an attractive solution to lung function monitoring in children and babies but has failed to move beyond a research tool, and its role remains unclear. This presentation will describe the current state of literature in this population and highlight novel and exciting new concepts. Particular focus will be on the use of EIT to better understand, and direct care during, the transition from fetal (liquid-filled lung) to ex utero (aerated) life.

To date, EIT has been predominantly used to understand the behaviour of the diseased and healthy neonatal lung during mechanical ventilation and spontaneous breathing[3-5]. This work has highlighted the gravity dependent pattern of preterm lung disease, and the described the regional changes that occur within the developing but diseased preterm lung with increasing age[4]. EIT has been used to challenge the traditional teaching that there are gravitational differences in regional ventilation between adults and infants[3].

In the short term, the clinical use of EIT in the neonatal population is likely to be related to simply identifying adverse events, such as pneumothroaces[6], or monitoring interventions, such as intubation[7] and ETT suction[8,9].

EIT has been shown have potential in optimising the application of HFOV using open lung strategies[5,10,11]. Although how these controlled research observations can be translated to a clinical tool remains uncertain. More recently, we have shown that EIT can be used to define the behaviour of the preterm lung at birth, allowing the process of aeration from a fluid filled fetal lung to an air filled one. There are important advantages in using EIT in this environment. Firstly, the process starts with a constant lung state that has never been aerated. Secondly, existing research tools to investigate this critical point in human physiology are either inaccurate, limited to a few research groups or hold no clinical translation. Finally, clinicians lack existing tools to guide resuscitation at birth. Increasingly, neonatologists are becoming aware of the need to optimise this process as irreversible lung injury pathways can be initiated from even one or two injurious inflations[12]. EIT imaging of regional aeration and tidal ventilation has shown that some accepted resuscitation strategies may not be lung protective or produce the benefits hypothesised (Fig 1)[13,14]. Last year we demonstrated that EIT could be used to guide lung aeration during the first inflations at birth.

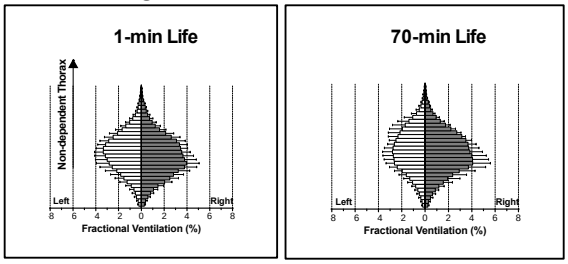

Figure 1: Changing pattern of fractional distribution of tidal ventilation at 1-min and 70-min after birth in a group of preterm lambs managed with a resuscitation strategy from the first inflation of life that was found to be injurious. Data derived from fEIT scans (from Tingay et al J Appl Physio 2013).

2 Conclusions

EIT has a long history as a research tool in infants, and has been used to explore a diverse range of issues. More recently, a number of research groups have been using EIT to guide respiratory therapies with promise. Translation into clinical practice will require commitment and cooperation from clinicians, engineers and mathematicians and industry.

References

[1] Schibler A, Frey U. *Arch Dis Child (F&N)* **87**:F7-10; 2002
[2] Anderson et al. *JAMA* **289**:3264-7; 2003
[3] Schibler et al *Pediatr Pulmonol* **44**: 851-8; 2009
[4] Armstrong et al. *Intensive Care Med* **37**:839-46; 2011
[5] Miedema et al *Intensive Care Med* **38**:294-9;2012
[6] Bhatia et al. *Intensive Care Med* **38**:308-15; 2012
[7] Schmoelzer et al. *Pediatr Pulmonol* **48**: 38-45; 2012
[8] van Veenendaal et al *Intensive Care Med* **35**:2130-4:2009
[9] Tingay et al *Intensive Care Med* **36**:888-96; 2010
[10] Miedema et al. *Eur Respir J* **40**:479-84: 2012
[11] Zannin et al Ped Res doi: 10.1038/pr.2013.251; 2013
[12] Bjorklund et al *Pediatr Res* **42**:348-355;1997
[13] Tingay et al Ped Res doi: 10.1038/pr.2013.218; 2013
[14] Tingay et al J Appl Physio1 **116**:251-8; 2014

Session 7

Poster Session II

25 April 2014, 9:30 – 9:45

Fixed-Duration versus EIT-determined Volume-Response Defined Sustained Inflation in Preterm Lambs

Anna Lavizzari[1,3] Elroy Zonneveld[1], Anushi Rajapaksa[1], Don Black[1], Liz Perkins[1], Magdy Sourial[2], Emanuela Zannin[6], Raffaele Dellaca'[6], Peter Davis[1,4,5], Fabio Mosca[3], David Tingay[1,2,4,5]

[1] Neonatal Research, Murdoch Childrens Research Institute, Melbourne, Australia;
[2] Royal Children's Hospital, Melbourne; [3] Neonatology, Fondazione IRCCS Ca'Granda, Ospedale Maggiore Policlinico-Università degli Studi di Milano, Milano, Italy; [4] Neonatal Research, Royal Women's Hospital, Melbourne; [5] University of Melbourne, Melbourne; [6]Dipartimento di Elettronica, Informazione e Bioingegneria, Politecnico di Milano, Milano, Italy.
David.Tingay@rch.org.au

Abstract: We compared a standard fixed duration Sustained Inflation (SI) during resuscitation at birth in preterm lambs with two SI guided by real-time volumetric EIT imaging, lasting respectively until volume plateau and until 30s beyond plateau. Global and local end expiratory volume (EEV), lung mechanics and gas exchange were measured. Both the volumetric EIT guided approaches were feasible and resulted in better relative lung aeration.

1 Introduction

Sustained Inflation (SI) is gaining increasing interest as a method of lung recruitment at birth [1]. A SI consists of applying a continuous elevated airway pressure to enhance lung liquid clearance and achieve functional residual capacity [2]. However the best way to deliver SI still remains to be elucidated [3]. Current SI strategies use a fixed duration and pressure, irrespective of the individual mechanical properties of the lung. The time constant of the lung is highly variable and unpredictable at birth. We aimed to investigate a new SI strategy tailored to the recipient's individual needs, in which duration was determined by the volumetric response at birth. Secondly, we wished to determine if a long SI would be harmful for the preterm lung.

2 Methods

127±1 day preterm lambs were instrumented, intubated and EIT electrodes applied before birth. Lambs were randomly assigned to one of following strategies at birth (n=11-13/group):

1. Control (PEEP group): positive pressure ventilation (PEEP 8 cmH_2O, PIP_{max} 40 cmH_2O)
2. Fixed duration SI (SI_{30}): 40 cmH_2O for 30s
3. EIT guided SI (SI_{EIT}): SI at 40 cmH_2O continued until no further visible gain in global lung volume (V_L) on EIT monitor (Thorascan, Carefusion, Germany).
4. SI_{long}: as for SI_{EIT} but continued for 30s after V_L stability was achieved in the global EIT-signal.

Thereafter, lambs were ventilated in a volume guarantee modality with 7 ml/kg tidal volume for 60 min.

Pressure, SpO_2, lung mechanics (including Forced Oscillation Technique; FOT), global and regional EEV and ventilation changes by EIT were recorded from birth, along with arterial blood gases. At 60 min lambs were euthanized and tissue taken for injury analysis. Differences between groups were tested by two-way ANOVA and Bonferroni *post hoc* test.

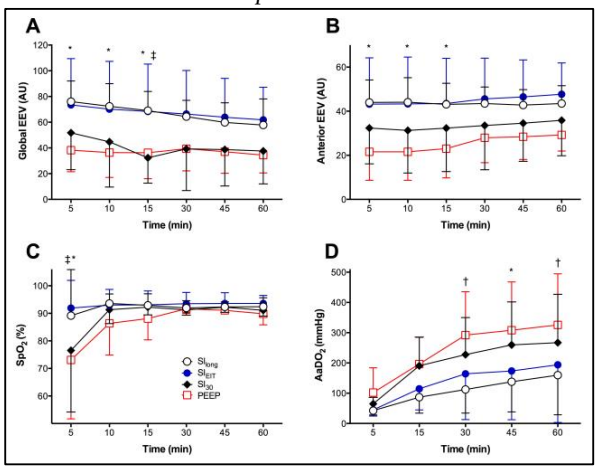

Figure 1: A. Global EEV, **B.** Anterior hemithorax EEV, **C.** Oxygen saturation (SpO_2) and **D.** Alveolar-arterial oxygen difference ($AaDO_2$). All data mean±SD. *PEEP vs SI_{long} & SI_{EIT} $p<0.05$; †PEEP vs SI_{long} $p<0.05$; ‡SI_{30} vs SI_{long} & SI_{EIT} $p<0.05$; §SI_{30} vs SI_{long} $p<0.05$.

3 Results

Both SI_{EIT} and SI_{long} resulted in higher EEV in the first 15-min of life (Fig 1A), with better recruitment in the non-gravity dependent (anterior) hemithorax (Fig. 1B), although the geometric centre of aeration was not different. The early improvements in EEV recruitment resulted in quicker attainment of target SpO_2 range and a sustained benefit in oxygenation (Fig 1C-D). Lung reactance was significantly higher reactance in SI_{EIT} and SI_{long} groups in the first three minutes of life, supporting better recruitment. No significant differences were found in broncho-alveolar lavage.

4 Conclusions

In our model, an individualised approach to resuscitation at birth, tailored to patients' lung mechanical properties, was feasible and may be beneficial for preterm neonates.

References

[1] te Pas AB et al. Pediatrics. 2007 Aug;120(2):322-9.
[2] te Pas AB et al. Pediatr Res. 2009;66(3):295-300.
[3] Tingay et al. J Appl Physiol. 2014. doi:10.1152/japplphysiol.01142.2013

Validation and Management of Data Quality Metrics on ICU Patients

Hervé Gagnon[1], Philippe Jouvet[2], Andy Adler[1]

[1]Carleton University, Ottawa, Canada
[2]Hôpital Ste-Justine, Montreal, Canada

Abstract: Real-time monitoring of lung function is one of the most promising applications of electrical impedance tomography (EIT). There are however some technical challenges that require validating diagnostic information extracted from EIT images. Two new data quality metrics are proposed and are applied on EIT and ventilator data acquired in an intensive care unit (ICU) setting. Their interpretation and usefulness in a clinical context is discussed.

1 Introduction

Real-time monitoring of mechanically-ventilated lung function at the bedside of intensive care unit (ICU) patients represents one of the most promising applications for electrical impedance tomography (EIT). Some technical challenges remain however before EIT could become a routinely used clinical tool in the ICU [1]. Most of these challenges are related to the long-term monitoring of patients for durations of hours or days. Maintaining high-quality EIT data then becomes difficult due to variations in quality of electrode contacts with the patient, instrumentation drift as well as patient's movement and manipulation by clinical staff. Some data quality metrics (DQM) have been proposed in the literature [2] to assess EIT data quality and therefore ensure the quality of any diagnostic or therapeutic information extracted from EIT images.

From reviewing and validating previous DQM definitions from the literature, two new simple and efficient DQM are presented. They are applied and validated on EIT and ventilator data previously acquired on ICU patients [3]. A discussion follows on how clinical staff should interpret and manage the information provided by these two new DQM.

2 Methods

Most EIT systems used for monitoring lung function reconstruct time difference images representing a change of conductivity relative to a reference state: $\mathbf{m} = (\boldsymbol{\sigma} - \boldsymbol{\sigma}_\mathrm{r})/\boldsymbol{\sigma}_\mathrm{r}$, where $\mathbf{m}$ is a vector, whose elements correspond to the element of a mesh or the pixels of an image, that represents the change of conductivity between the latest conductivity distribution $\boldsymbol{\sigma}$ and a reference conductivity distribution $\boldsymbol{\sigma}_\mathrm{r}$. Such images are typically reconstructed from normalized voltage difference data $\mathbf{d} = (\mathbf{v} - \mathbf{v}_\mathrm{r})/\mathbf{v}_\mathrm{r}$, where $\mathbf{v}$ is the latest voltage measurement vector and $\mathbf{v}_\mathrm{r}$ is the voltage measurement vector corresponding to a reference state.

The relationship between $\mathbf{d}$ and $\mathbf{m}$ is typically obtained from the linearization of a physics model:

$$\mathbf{d} = \mathbf{J}\mathbf{m} \tag{1}$$

where $\mathbf{J}$ represents the Jacobian or sensitivity matrix. Since, EIT is an ill-posed problem, some optimization algorithms combined with regularization techniques are used to obtain the following linear relationship:

$$\mathbf{m} = \mathbf{R}\mathbf{d} \tag{2}$$

where $\mathbf{R}$ is called the reconstruction matrix which can be derived from different optimization methods such as, for instance, the *maximum a posteriori* (MAP) estimate.

From (1) and (2), reconstruction error $\boldsymbol{\varepsilon}_\mathrm{reconst}$ can be defined as:

$$\boldsymbol{\varepsilon}_\mathrm{reconst} = \frac{1}{P_\mathbf{d}}(\mathbf{I} - \mathbf{J}\mathbf{R})\mathbf{d} \tag{3}$$

where $P_\mathbf{d}$ is the average signal $\mathbf{d}$ obtained for a spherical conductivity located in the medium center with 2:1 contrast and 20% medium radius.

Reciprocity error $\boldsymbol{\varepsilon}_\mathrm{recip}$ can be defined as:

$$\boldsymbol{\varepsilon}_\mathrm{recip} = \frac{1}{P_\mathbf{v}}(\mathbf{I} - \mathbf{K}(\mathbf{K}^\mathrm{t}\mathbf{K})^{-1}\mathbf{K}^\mathrm{t})\mathbf{v} \tag{4}$$

where $P_\mathbf{v}$ is the average of signal $\mathbf{v}$ and $\mathbf{K}$ is a matrix representing the relationship $\mathbf{v} = \mathbf{K}\mathbf{v}_\mathrm{ind}$ between voltage measurement vector $\mathbf{v}$ and a reduced-size version $\mathbf{v}_\mathrm{ind}$ containing only a set of independent voltage measurements mainly due to the reciprocity principle. Using (4) implies that the EIT acquisition system performs some reciprocal measurements or else $\mathbf{K}$ would be equal to the identity matrix $\mathbf{I}$ and $\boldsymbol{\varepsilon}_\mathrm{recip}$ would be equal to the zero vector $\mathbf{0}$ and become useless. In practice, most systems perform reciprocal measurements.

Finally, DQM q_reconst and q_recip are defined by respectively substituting $\boldsymbol{\varepsilon}_\mathrm{reconst}$ and $\boldsymbol{\varepsilon}_\mathrm{recip}$ from (3) and (4) into

$$q = \frac{1}{M}\sum_{i=1}^{M}\left(\frac{1}{2}\right)^{|\varepsilon_i|} \tag{5}$$

where M represents the length of $\boldsymbol{\varepsilon}_\mathrm{reconst}$ or $\boldsymbol{\varepsilon}_\mathrm{recip}$ depending on which DQM is being computed. Following this definition, any computed q value will be constrained between 0 and 1 to respectively indicate poor or good data quality.

3 Discussion

DQM were computed on data acquired on ICU patients from a previous study [3] and validated with the corresponding ventilator data. It was found that 1) DQM show abrupt changes, which often correspond to known events, and 2) DQM behave differently and are sensitive to different effects. q_recip indicates the quality of a particular voltage measurement vector $\mathbf{v}$ while q_reconst is useful to assess the quality of reconstructed images. q_reconst is affected by several parameters: mainly, reference voltage measurement vector $\mathbf{v}_\mathrm{r}$, physics model geometry and reference conductivity distribution $\boldsymbol{\sigma}_\mathrm{r}$ used to compute Jacobian $\mathbf{J}$. q_reconst can be used to assist clinicians in selecting the best model geometry and reference conductivity distribution for a given patient and in assessing how long a reference state ($\boldsymbol{\sigma}_\mathrm{r}$, $\mathbf{v}_\mathrm{r}$) is valid before a new one should be selected or acquired.

References

[1] Adler A, Amato MB, Arnold JH, et al. *Physiol Meas* **33**:679–694, 2012

[2] Mamatjan Y, Grychtol B, Gaggero P, et al. *IEEE Trans Med Imag* **32**:1997–2005, 2013

[3] Gagnon H, Jouvet P, Gervais JC, et al. In *XIVth Conference on Electrical Impedance Tomography, Heilbad Heiligenstadt, Germany*. 2013

Adaptive Kaczmarz method for cardiac activity reconstruction in electrical impedance tomography

Taoran Li[1], David Isaacson[1], Jonathan C. Newell[1], Gary J. Saulnier[1]

[1]Rensselaer Polytechnic Institute, Troy, USA, lit5@rpi.edu

Abstract: An adaptive Kaczmarz method to reconstruct conductivity changes from 2D EIT data is described. The framework to combine the adaptive Kaczmarz method and the adaptive mesh refinement is also outlined in the paper. Reconstructions from data collected on a human chest torso are shown. The results accurately recover the conductivity changes during a cardiac cycle and demonstrate the reconstruction performance of the adaptive Kaczmarz method.

1 Introduction

In this paper, we will outline a framework to combine the adaptive Kaczmarz method and the adaptive mesh refinement techniques. The adaptive algorithm can locally refine the mesh and generate optimal current patterns to improve the accuracy of the reconstructed images with the help of the prior information obtained from the previous iterations.

2 Methods

The adaptive Kaczmarz method was introduced and described in more detail in [1]. It combines the block Kaczmarz method and optimal current pattern generation. The algorithm avoids the inversion of large matrices at each iteration and adaptively generates optimal current patterns to improve the distinguishability of the system. It can solve the reconstruction problem cost-efficiently without degrading the quality of the reconstructed images.

2.1 Adaptive Kaczmarz with Adaptive Mesh Refinement

The proposed algorithm balances the trade-off between the accuracy and the efficiency of the EIT reconstruction process. With the help of adaptive mesh refinement, it is possible to avoid unnecessary mesh elements and improve the efficiency and the conditioning of the reconstruction. The flowchart of the adaptive algorithm is shown in Figure 1.

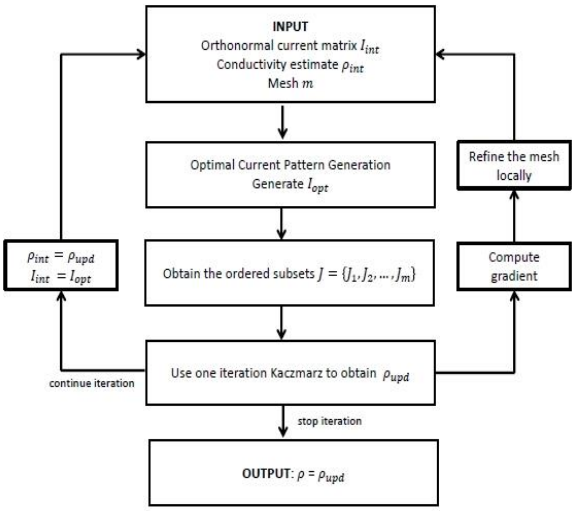

Figure 1: Flowchart of the adaptive algorithm

2.2 Results of the adaptive Kaczmarz

The images were reconstructed from archival data measured by the ACT3 system at Rensselaer Polytechnic Institute. In Figure 2, a sequence of 8 images in one cardiac cycle is displayed.

3 Conclusions

In this paper, reconstructions of cardiac activity using the adaptive Kaczmarz are shown and a new adaptive algorithm is outlined.

References

[1] Li T, Kao T, Isaacson D, Newell J C and Saulnier G. Adaptive kaczmarz method for image reconstruction in electrical impedance tomography *Physiol. Meas.* **34**:595–608, 2013

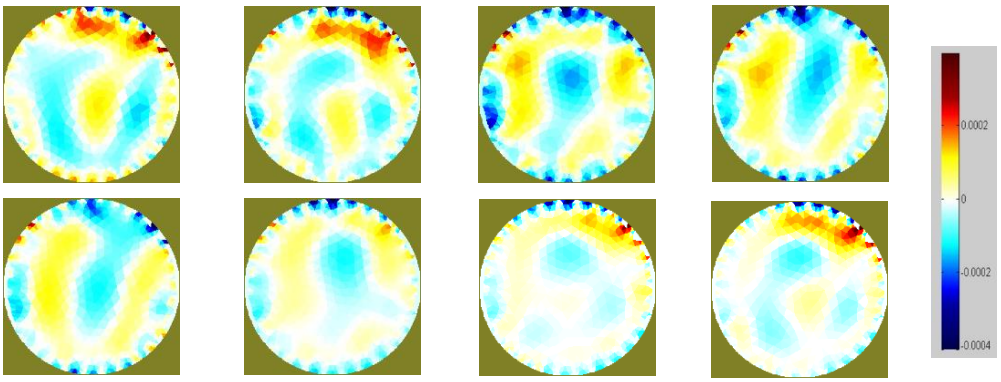

Figure 2: A sequence of 8 different images in one cardiac cycle is shown.

Evaluation of Centre of Ventilation (CoV) during three different ventilation conditions

Martina Mosing[1], Andreas D. Waldmann[2], Thom Gent[1], Nadja Sieber-Ruckschuh[1] and Stephan H. Bohm[2]

[1]Vetsuisse Faculty, Zürich, Switzerland; mmosing@vetclinics.uzh.ch
[2]Swisstom AG, Landquart, Switzerland

Abstract: The EIT-based Centre of Ventilation (CoV) within the lungs was evaluated at baseline and 10 minutes after applying three ventilation conditions: (1) zero end-expiratory pressure (ZEEP), (2) 5 cmH_2O of PEEP without a recruitment maneuvre (RM) and (3) after a RM. A significant dorsal shift of the CoV was seen for the RM, but not for the other two conditions.

1 Introduction

During anaesthesia, functional residual capacity decreases resulting in atelectasis formation in the dependent parts of the lungs. Several ventilation modes have been used to avoid or counteract this lung collapse. However, monitoring the effectiveness of different ventilation modes and settings is still challenging. The CoV has been used to evaluate the distribution of ventilation within the lungs of anaesthetised subjects [1].
The aim of this study was to investigate in healthy dogs the shift in the CoV under changing ventilation conditions.

2 Methods

The lungs of nine healthy Beagle dogs positioned in dorsal recumbency were ventilated during three subsequent anaesthesias (sevoflurane in oxygen 100%) using volume-controlled ventilation at 10 ml kg^{-1}, zero end-expiratory pressure (ZEEP) and a respiratory rate adjusted to maintain $P_E'CO_2$ between 4.7 and 5.3 kPa. After 35 minutes, baseline EIT images were recorded using a belt around the thorax caudal to the apex of the heart (T_1). Dogs then underwent in randomised order either continued ventilation at ZEEP (control group), ventilation with positive end-expiratory pressure of 5cmH_20 (PEEP) alone or after a recruitment manoeuvre (RM) performed by increasing PEEP stepwise to 15 cmH_2O and peak inspiratory pressure to 40 cmH_2O and by maintaining them there for 10 breaths [2]. Measurements were repeated after 10 minutes (T_2). The ventilation-related relative impedance changes (ΔZ) from the start to the end of inspiration were calculated, see Figure 1. Then the geometric CoV was determined. T_1 was compared to T_2 using Student´s paired t-test.

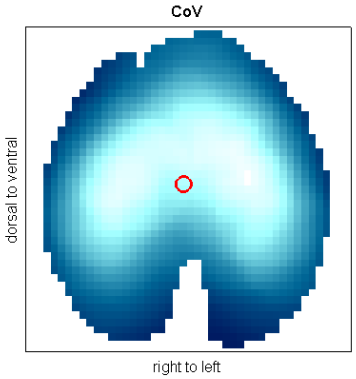

Figure 2: EIT ventilation image of a dog with CoV (red circle). Bright colours mark areas with high and dark colours areas with low impedance changes, which relate directly to the amount of regional ventilation. The CoV is calculated from the tidal image (end minus start of inspiration).

3 Results

Only after the RM a significant dorsal shift of the CoV was found (P = 0.0118), while such a redistribution of ventilation was observed neither during ZEEP nor PEEP (Figure 2).

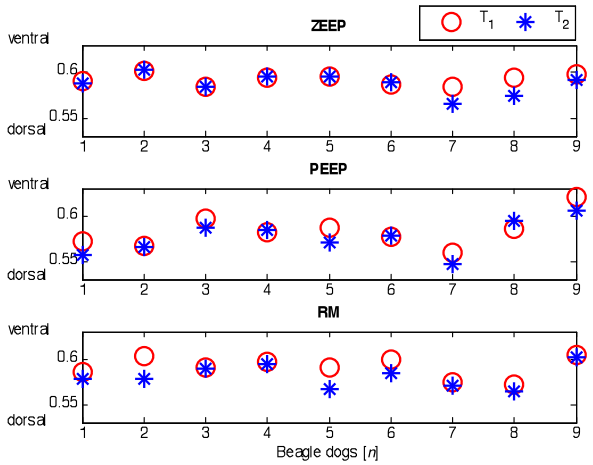

Figure 2: CoV before (T_1) and after (T_2) applying three different ventilation modes to the lungs of healthy dogs. ZEEP = zero end-expiratory pressure, PEEP = positive end-expiratory pressure, RM = recruitment manoeuvre combined with PEEP.

4 Conclusions

While the combination of RM and PEEP caused a significant dorsal shift of the CoV from baseline ventilation at ZEEP even in healthy lungs and during short term ventilation, PEEP did not show the same effect.

References

[1] Radke O, Schneider T, Heller A. Spontaneous breathing during general anesthesia prevents the ventral redistribution of ventilation as detected by electrical impedance tomography. Anesthesiology 116: 1227-1234, 2012.
[2] Tusman G, Böhm S, de Anda GFV, Do Campo J, Lachmann B. "Alveolar recruitment strategy"improves arterial oxygenation during general anaesthesia. British Journal of Anaesthesia 82: 8–13, 1999.

An Approach to Extend GREIT Image Reconstruction to 3D

Justin Wagenaar[1], Bartłomiej Grychtol[2], Andy Adler[3]

[1]Carleton University, Ottawa, Canada
[2]German Cancer Research Center, Heidelberg, Germany
[3]Carleton University, Ottawa, Canada

Abstract: This paper presents a new image reconstruction technique for 3D EIT based on the extension of the 2D GREIT method. Key aspects include the expansion of optimization targets and set of desired images to cover multiple planes. Results show the reduction off-plane interference seen in 2D reconstruction. The selection of target planes is also found to be highly significant to the image.

1 Introduction

There is strong potential in the use of 3D imaging in Electrical Impedance Tomography (EIT) applications, [1,2] despite challenges with accuracy, evaluation, and processing requirements. This paper presents a new method for 3D EIT image reconstruction. The method is compared with the 2D GREIT method to analyze the influence of off-plane targets.

2 Methodology

2.1 GREIT Method

The 3D reconstruction approach is an extension of the 2D GREIT method, which is described in [3]. The 2D method consists of a forward model, a noise model, and a set of desired performance metrics. A training set of conductivity target images is created based on the performance metrics. The reconstruction matrix R is then calculated as follows:

$$R = DY^{-1}(YY^{-1} + \Sigma_n)^{-1} \quad (1)$$

where D is a point spread function based on the desired target features, Y is the set of simulated target measurements, and Σ_n is the noise covariance term.

In order to extend this algorithm to 3D, a three dimensional set of targets is created. A set of target planes must be selected according to the region of interest, as well as speed and memory concerns.

The calculation of matrix D is expanded to cover the n target planes, giving diagonal matrix $D_{n,n}$. A matrix $D_{i,i}$ is solved for each target plane i based on the desired performance metrics. This approach assumes that the target radius is smaller than the target plane separation.

2.2 Simulation

The proposed 3D GREIT method is compared to the 2D GREIT method to examine the effects of off-plane targets on image quality. The forward model is built using a cylindrical finite element model (FEM) using 35 089 elements. The 2D model includes one ring of 16 circular electrodes and the 3D model uses 2 rings of 16 electrodes. Measurements are simulated using the adjacent pattern. The 2D method solves each plane individually while the 3D method uses a single reconstruction matrix.

3 Results and Discussion

The reconstructed images, overlaid onto the FEM model, are shown in Fig. 1. The 2D GREIT image shows strong off-plane influence. For each slice, the image extends towards the off-plane sphere, resulting in a wide column. The 3D GREIT image is better constrained to the object regions for both the on- and off-plane objects.

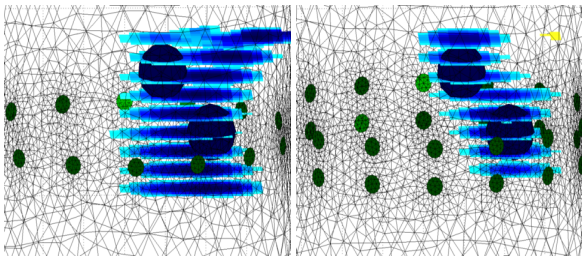

Figure 1: Reconstructed images using 2D GREIT method `left` and 3D GREIT method `right` for one on-plane sphere and one off-plane sphere. Images generated using `EIDORS`.

The 3D GREIT method provides better resolution and lower position error, as illustrated in Fig. 2. This suggests that the 3D method has improved immunity to off-plane effects while also providing useful information concerning regions outside the electrode planes.

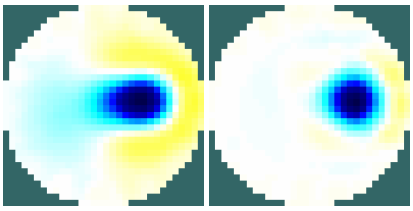

Figure 2: Centre image slice from 2D GREIT method `left` and 3D GREIT method `right`. Images generated using `EIDORS`.

Although 2D GREIT allows the specification of the position of the desired image plane, since a single image must explain all the data, it necessarily conflates the two targets. By simultaneously reconstructing images at multiple planes, 3D GREIT allows to distinguish changes occurring at different levels, resulting in reduced off-plane influence. Consequently, the selection of the target planes has high significance in the 3D GREIT method.

4 Conclusions

The 3D GREIT method proposed in this paper has been demonstrated against the 2D GREIT method. Results indicate that the 3D GREIT method reduces off-plane effects and allows for the imaging of off-plane objects, while improving resolution and position error. In addition, the selection of target planes will have a significant impact on the image.

References

[1] Adler A. et. al. *Physl Meas* 33:679-694 2012.
[2] Zhao Z. et. al. *Journal of Cystic Fibrosis* 11:412-418 2012.
[3] Adler A. et. al. *Phys Meas* 30:S35-55 2009.

GREIT is sensitive to training targets near boundary

Zhanqi Zhao[1], Andy Adler[2], Knut Möller[1] and Bartłomiej Grychtol[3],

[1]Furtwangen University, VS-Schwenningen, Germany, zhanqi.zhao@hs-furtwangen.de

[2]Systems and Computer Engineering, Carleton University, Ottawa, Canada

[3]Medical Physics in Radiology, German Cancer Research Center (DKFZ), Heidelberg, Germany

Abstract: It has been observed that the distribution of the training targets used to calculate the GREIT reconstruction matrix has a strong impact on its chief figure of merit, the amplitude response (AR). We found that uniform AR requires a minimum target distance to the domain boundary, and target density gradient toward the centre has less impact on uniform AR.

1 Introduction

In the GREIT framework [1], the reconstruction matrix for linear difference EIT is calculated based on a training set of simulated measurements of small single-target conductivity perturbations and the corresponding desired images, constructed based on specified consensus figures of merit. Chief among the requirements is that equal conductivity changes have equal effects on the image regardless of their position, i.e. uniform amplitude response (AR).

Originally, GREIT was proposed for cylindrical domains and used a centre-heavy spiral distribution of training targets in the plane of electrodes. After extruded shapes of arbitrary contour were introduced to GREIT [2], the default distribution of training targets was changed to a uniform grid pattern, since the original spiral was not generalizable and random distributions were deemed not suitable. It was later observed that this distribution produces a less uniform amplitude response (AR) than the original formulation.

Since the fluctuation of AR becomes stronger close to the domain boundary, we investigated 2 properties in the present study: i) target density gradient toward the centre, and ii) minimum target distance to the boundary.

2 Methods

The plane of electrodes is divided into concentric ring-shaped layers by binary image erosion. Within each layer, training targets are distributed in a uniform gird. The target density in each layer is defined by the ratio between two consecutive layers (denoted as R2L). We analyse three distributions for 5 layers with i) equal density in each layer (R2L=1), ii) moderate density gradient towards the centre (R2L=1.2), and iii) strong density gradient (R2L=3). At the same time, we varied the target distance to the boundary (D2B) from 0 to 2 times of target radius in steps of 0.5. For each distribution, we calculate a GREIT matrix for EIDORS's adult thorax model such that noise figure in the centre equals 0.5. Results are compared by calculating the figures of merit defined in [1] for a set of uniformly distributed targets in the electrode plane.

3 Discussion

Figure 1 shows part of the results due to limited space. AR was more homogeneous when R2L=3 (Fig. 1, middle) compared to R2L=1 (Fig. 1, left) due to the fact that the density of targets near the boundary was strongly reduced. AR became even more uniform by simply adding target distance to the boundary (Fig. 1, right). We found that uniform AR requires a minimum target distance to the domain boundary, and target density gradient toward the centre has less impact on uniform AR.

References

[1] Adler A, et al. *Physiol Meas.* **30**:S35-55, 2009

[2] Grychtol B, et al. *IEEE Trans Med Imaging*. **31**:1754-60, 2012

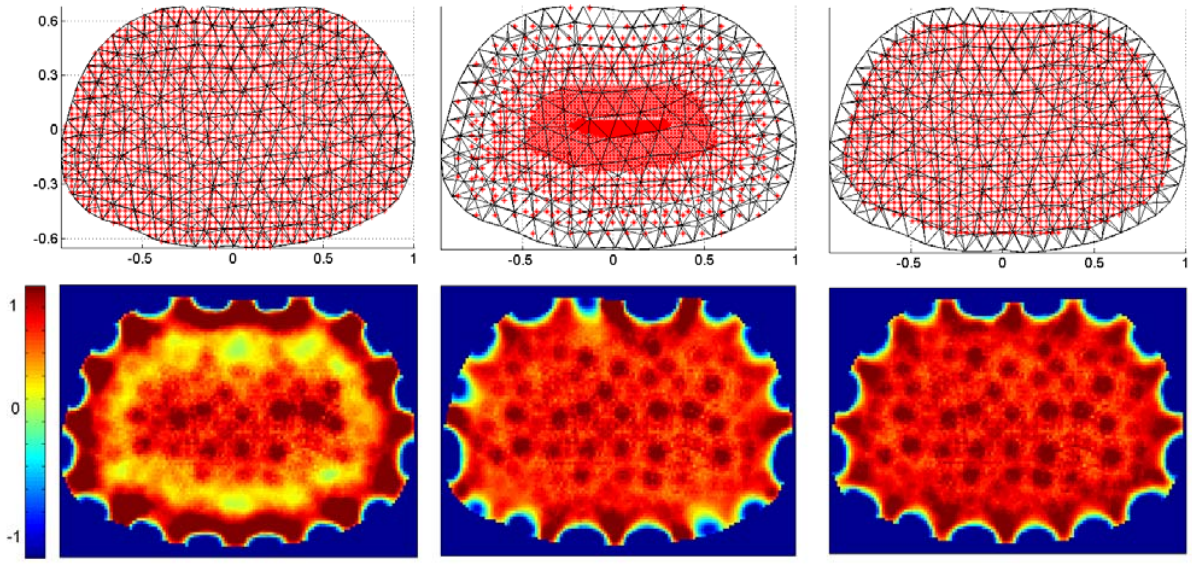

Figure 1. Top: distributions of training targets (red *) test. Left, R2L=1, D2B=0; middle, R2L=3, D2B=0; right, R2L=1, D2B=1.5; Bottom: corresponding AR maps normalized to the value in the centre.

3-D Electrical Impedance Tomography Reconstruction Using ℓ_1 Norms Regularization

Yang Pu, Qifan Wang and Tao Dai

Sealand Technology (Chengdu), Ltd., Chengdu, China. ypu@eitchina.net

Abstract: An ℓ_1 norm reconstruction algorithm which has the merits of reducing the sensitivity to data outliers and avoiding edge blurring is applied in this paper to solve a 3-D EIT problem. The iterative imaging method allows flexible choice of norms by simply choosing different norm value. A cluster analysis is implemented for labelling targets using the morphology technique.

1 Introduction

Electrical Impedance Tomography (EIT) is a soft field imaging modality due to the diffusive propagation of electrical current. Reconstruction of the internal conductivity distribution from boundary measurements is severely ill-conditioned. Most reconstruction algorithms are based on ℓ_2 norm regularization (e.g. one-step GN method) which is believed to blur image outlines and be sensitive to measurement noises. These difficulties can be greatly alleviated if ℓ_1 norm reconstruction technique is involved [1-5]. An ℓ_1 norm applied on the measurements residue term reduces the sensitivity to data outliers, while an ℓ_1 norm on the image prior term avoids edge blurring. An ℓ_1 norm iterative method is applied in this paper to solve a 3-D EIT problem, which is designed to detect breast cancer from women patients. In the post-processing stage, a cluster analysis is applied for labelling reconstructed targets using the morphology technique. Simulative and phantom experiments showed the advantages of ℓ_1 norm reconstruction and the validity of the clustering method.

2 Methods

A weighted and regularized inverse seeks an estimate solution $\hat{\mathbf{x}}$ by minimizing

$$\hat{\mathbf{x}} = \underset{\mathbf{x}}{\operatorname{argmin}} \|\mathbf{y} - \mathbf{J}\mathbf{x}\|_{\Sigma_n^{-1}}^{p_n} + \|\mathbf{x} - \mathbf{x}^0\|_{\Sigma_x^{-1}}^{p_x} \qquad (1)$$

Where p_n and p_x are the data and image norms respectively. With $p_n = 2, p_x = 2$ it models the ℓ_2 norm regularization; while with $p_n = 1$, $p_x = 1$, ℓ_1 norm reconstruction can be achieved. In this paper, a general iterative method for solving (1) is applied, which allows flexible choice of norms by simply choosing different p_n and p_x value. Details can be found in [5], and will not be elaborated here.

When EIT reconstruction is completed, image filtering technique is implemented to remove noises, and then a cluster analysis based on the morphology is involved for labelling targets.

3 Results

3.1 Numerical simulation

The forward model was a funnel-shaped applicator. 64 electrodes were located surrounding the outside surface. Inside, there were two targets with conductivity $1.2 \times \sigma_h$, while the background had conductivity $\sigma_h = 1$. In order to accurately simulate forward model and make inverse solution less ill-conditioned, dual model was applied, which means a fine mesh for the forward and coarse mesh for the inverse. Gaussian white noise was added to the simulation data with noise level SNR=20dB. When reconstruction was completed, cluster analysis was implemented. The two targets were marked by different colours (red and yellow) as shown in Fig. 1.

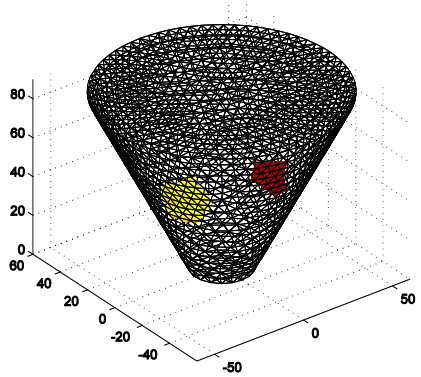

Figure 1: Image reconstructed using ℓ_1 norm and labelled by cluster analysis.

3.2 Phantom experiment

The saline phantom was fabricated the same as described in the previous section. Small biological tissues such as potato, apple and porcine liver were statically suspended in the saline solution. Similar results were obtained.

4 Conclusions

EIT images reconstructed using ℓ_1 norm regularization give two distinct advantages: edge preservation and noise robustness. However, the disadvantage is that the ℓ_1 norm formulation cannot be realized as a linear one-step algorithm due to non-differentiability. In this paper, we extended Dai's previous work [5] from 2-D to 3-D problem, and proved that the iterative process for solving (1) is effective in 3-D scenario as well. Moreover, the cluster analysis based on the morphology technique was involved and successfully separated targets from the background, which is important in clinical applications.

References

[1] Y. Mamatjan, *Physiol Meas*, 34:1027−1039, 2013
[2] Y. Mamatjan, Canadian Medical and Biological Engineering Society (CMBEC 35) and Canada Clinical Engineering Society (ACCES 17) conference, June 19−22, Halifax, Canada, 2012
[3] A. Borsic, *Inverse Problems*, 28:095011, 2012
[4] A. Borsic, *IEEE Trans. Medical Imaging*, 29: 44-54, 2010
[5] T. Dai, *Conf. IEEE Eng. Med. Biol. Soc.*, Vancouver, Canada, August 20-24, 2008

A Hybrid Image Reconstruction for Medical Magnetic Induction Tomography: an experimental evaluation

Lu Ma, Chuan Yang, and Manuchehr Soleimani

Engineering Tomography Laboratory, Department of Electronic and Electrical Engineering,
University of Bath, Bath, UK

Abstract: Magnetic induction tomography is a tomographic technique with potential medical applications. However, the realization of this technique remains a challenging topic both in hardware and in image reconstruction. This paper presents a hybrid image reconstruction algorithm for the image reconstruction using experimental data.

1 Introduction

Magnetic induction tomography (MIT) is capable of imaging electrical properties of the materials under testing [1]. Due to its contactless and non-invasive nature, it has great potential to be employed in medical applications, such as brain imaging. As MIT is a low-resolution technique, one of the major issues lies in the image reconstruction. The main objective of this study is to improve the quality of reconstructed images by using a hybrid regularization algorithm resulting in some enhancements in reconstructed images.

2 Methods

In the forward problem of MIT, a reduced magnetic vector potential is used [2]. The general equation in quasi-static electromagnetic field can be written as.

$$\nabla\times\left(\frac{1}{\mu}\nabla\times A_r\right)+j\omega\sigma A_r = \nabla\times H_s - j\omega\sigma A_s - \nabla\times\frac{1}{\mu}\mu_0 H_s \quad (1)$$

where A_r is the reduced magnetic vector potential in the eddy current region, ω is the angular frequency, σ is the electrical conductivity, H_s is the magnetic field due to the the excitation coil, which can be directly computed according to the Biot-savart law. A_s is the impressed magnetic vector potential as a result of source current density J_s, μ_0 is the permeability of the free space, and μ is the permeability of the medium. In equation 1), the only unknown is A_r, which can be computed by soving the system linear equation [3].

$$SA_r = b \quad (2)$$

where S is a system matrix, and b is the right hand side current density. The inverse problem of MIT can be solved by using a hybrid image reconstruction algorithm [4].

$$\Delta\sigma = (J^TJ + \alpha R_1 + \beta R_2)^{-1}J^T(\Delta v) \quad (3)$$

where Δv is the changes in the induced voltage measurements, J is the sensitivity map computed from the forward model, R_1, R_2 are the regularization matrices, and α and β are the regularisation factors for R_1 and R_2 respectively. A combination of NOSER and identity matrix was used as hybrid regularization scheme. Combined regularization produces images with more accurate location and shape of the inclusion(s).

3 Imaging system

The Bath medical MIT system is shown in Figure 1. It is a 16 channel National Instrument based system working at 13 MHz excitation modes. The detailed system design has been reported in [5]. Imaging different level of salinity solutions inside various salinity solutions background carries out the experiments. Both individual and multiple bottles are used. A large number of experimental data are collected to verify the proposed method. Figure 1 gives an example of reconstructed images using non- conductive bottles inside 0.9% saline solution in different locations.

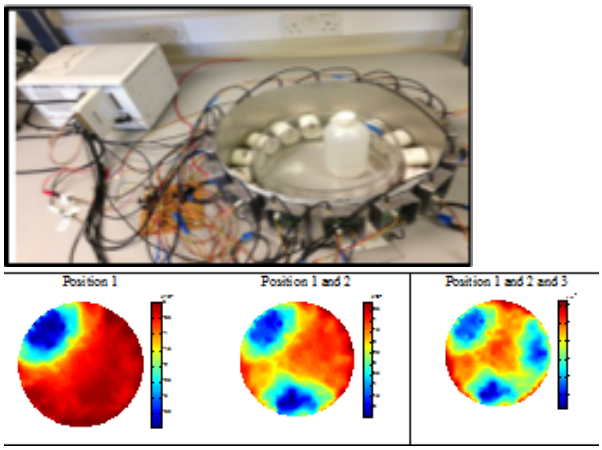

Figure 1: Bath 16-channel medical MIT system, reconstruction of 1, 2 and 3 bottles in saline background with 0.9% saline.

4 Conclusions

A hybrid image reconstruction algorithm is presented in this study in an attempt to improve the quality of reconstructed images. Both forward and inverse problems are studies, and the results are validated using large number of experimental data. The proposed hybrid regularization provides better quality reconstruction compared to each of these regularization methods.

References

[1] Griffiths H. *Meas. Sci. Technol.*12: 1126– 1131, 2001
[2] Bíró O. *Comput. Method. Appl. M.* 169: 391–405, 1999.
[3] Soleimani M, Lionheart WRB. *IEEE T. Med. Imaging.* 25 (12): 1521-1530, 2006
[4] Hu L, Wang HX, Zhao B, Yang WQ. *Meas. Sci. Technol.*18: 813-818, 2007
[5] Wei HY, Soleimani M. *Physiol. Meas.* 33(5): 863-879, 201.

Quantitative index of EIT based on 3D abdominal bleeding simulation model

Fusheng You[1], Xuyang Huo[2], Xiaolei Zhao[2], Xiuzhen Dong[1]

[1]Department of Biomedical Engineering, Fourth Military Medical University, Xi'an, China. fushengyou@fmmu.edu.cn
[2]School of public health, Jilin Medical College, Jilin, China.

Abstract: According CT images, a 3D abdominal bleeding simulation model with real shape was set up using COMOSOL Multi-physics. By parameter sweeping, the surface measurement data for EIT were obtained while bleeding from 0~800ml. Total relative changes (TRC) of the data were calculated, shown a linear correlation (R>0.99) with bleeding volume (BV), which implies TRC be a good quantitative index to indicate BV.

1 Introduction

Electrical impedance tomography (EIT) is noninvasive and sensitive to abdominal bleeding. Bleeding model in pig shown that 30ml of blood could be detected by EIT [1], also EIT is sensitive to detect 20ml of conductive fluid in the peritoneum of patient [2].So abdominal bleeding can be dynamically and sensitively detected by EIT *in vivo* [1-3]. How to quantitatively monitor bleeding volume is the key problem which should be solved by abdominal EIT. Several quantitative indexes (QI), such as resistivity index (RI) [2,4,5], total relative changes (TRC) [6] and singular value decomposition (SVD) [7] have been reported to quantitatively estimate the volumes of lung air or liquid in dogs, abdominal liquids in phantom or patients, and balder volume in simulation, respectively. In order to systematically testify the relation of QI and BV, a 3D real shape abdominal bleeding simulation model was built.

2 Methods

The simulation model has been built from abdominal CT images. According the grey values of CT image, 3D shapes of liver, spleen, stomach, kidney and backbone, etc., were segmented and saved as CAD files. Then the data of different organs were input into COMSOL to form a 3D real shape model of abdomen. To solve the forward problem of EIT, 16 copper electrodes placed on the the model for polar driving and adjacent measuring.

2.1 To simulate different bleeding volumes

A sphere with different volumes to simulate different BV was put into the abdominal model at the electrodes plane, as shown in Fig.1. The volumes of sphere was set to 0, 5, 10, 20, 30, 40, 50, 60, 70, 80, 90, 100, 150, 200, 250, 300, 350, 400, 450, 500, 550, 600, 650, 700, 750, 800ml, in total 26 volumes. 0ml was treated as reference without bleeding. Using parameter sweeping function of COMSOL the radius of sphere was swept from 0 to 5.78cm, and 26 EIT data for the above BV were obtained.

2.2 To set parameters of the 3D model

In the 3D model, there are 243120 volume elements. For different organs and tissues, such as liver, spleen, stomach, kidney, backbone and blood, their conductivity and permittivity were set accordingly.

The bleeding simulation was done in COMSOL using the AC/DC module. Automatic changing of the current injection electrodes (polar driving) was accomplished by COMSOL LiveLink for Matlab interface [7]. For each BV a frame data with 16X16 was obtained by rotating 16 times of driving electrodes.

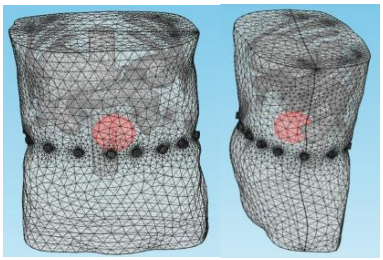

Figure 1: 3 D abdominal bleeding model with 16 electrodes

2.3 To calculate quantitative index

TRC was used as QI. The frame data without bleeding was set as reference data, and the other 25 frame data with different BV were used to calculate TRC [6], then the 25 TRC data and 25 BV data were analysed by linear fitting.

3 Conclusions

The TRC has a significant linearity with the BV (R=-0.999). Equation (1) gives the linear relationship between TRC and BV.

$$TRC = -0.0067*BV-0.0484 \quad (1)$$

The results shows that in 3D abdominal simulation model, TRC is a good QI to estimate BV in the range of 0-800ml, the results is also same as in phantom experiments [6], in which TRC has a good linear relation with the volumes of saline solution (150ml in total) perfused into physical phantom.

In practice, abdominal motion arising in breath and organ movements would cause impedance changes [2]. How to filter such kind of interfere and how to evaluate different QI, more trials *in vivo* should be studied further.

Acknowledgement: This research was partly supported by China MOST 2012BAI20B02 and NSFC 51177166.

References

[1] Shuai WJ, *et al.* Physiol. Meas. **29 :** 217–225, 2008
[2] Sadleir RJ and Fox RA.. IEEE TBME 48(4), 484-491, 2001
[3] YOU FS, *et al.* Intensive Care Med. 39(6): 1159-60, 2013
[4] Tucker AS, *et al.* Physiol. Meas. 32: 151–165, 2011
[5] Adler A, *et al.* J. Appl. Physiol. 83: 1762–7, 1997
[6] YOU FS, *et al.* IEEE TBME., 55(3):1224-6, 2008
[7] Schlebusch T, *et al.* 35th IEEE EMBS Conference, p 6441 – 6444, 2013

Application of a Fast Parallel EIT Forward Solver to Study the Feasibility of Stroke Type Detection

Markus Jehl[1], Emma Malone[2], Timo Betcke[3], David Holder[4]

[1]Department of Medical Physics and Bioengineering, University College London, markus.jehl.11@ucl.ac.uk
[2]Department of Medical Physics and Bioengineering, University College London
[3]Department of Mathematics, University College London
[4]Department of Medical Physics and Bioengineering, University College London

Abstract: We present an application of a newly developed fast parallel EIT forward solver (PEITS) implemented in C++. Its features are summarised and the installation, configuration and interface to Matlab are demonstrated. An application of the solver to a feasibility study of stroke type differentiation is illustrated. We found that precise positioning of the electrodes is critical for obtaining good images of stroke.

1 Introduction

Most research groups in EIT currently use the Electrical Impedance Tomography and Diffuse Optical Tomography Reconstruction Software EIDORS [1], which is programmed in Matlab. EIDORS provides many useful features, such as 2D and 3D forward simulations and an extensive collection of reconstruction algorithms, visualisation functions and more. Horesh et al. [2] adapted EIDORS with different preconditioners and more efficient routines, resulting in a version called SuperSolver. For large meshes, however, Matlab suffers from a lack of efficient parallel programming possibilities, which makes the computation of forward solutions a lengthy task. Last year we presented the implementation of a fast parallel forward solver using the complete electrode model, which is now available for free download [3].

2 Methods

2.1 Running PEITS

Used on a workstation or computer cluster, the *P*arallel *EIT S*olver (PEITS) reduces the computation times for the forward solutions and the Jacobian matrix significantly on large finite element meshes. A typical EIT application with 60 forward solutions and around 1000 protocol steps (i.e. 1000 lines in the Jacobian matrix) can be solved on 40 processors in 78 seconds on a 2 million element mesh, and in less than 18 minutes on a 15 million element mesh. Even on one processor we found PEITS to be twice as fast as an optimised version of EIDORS for an application on 2 million elements. This comes at the expense of less flexibility with regards to different applications, e.g. parallel current injection is not yet supported. PEITS is currently only supported on UNIX systems, where it can be easily installed following the guidelines on the website [3].

2.2 Feasibility Study

We are presenting the application of PEITS in a simulation study determining the main error sources in frequency-difference EIT imaging of stroke [4]. This study required 31 forward solutions on a 5 million element mesh for 12 different frequencies for each studied situation. In total this added up to more than 5000 forward solutions. On all 16 cores of a workstation with two 2.4GHz Intel Xeon CPUs with eight cores and 20MB cache each, the computation time for all forward solutions was around 300 minutes. The results of the study show that the precise positioning of electrodes is critical for good image quality. Even electrode misplacements as small as 1.3mm can lead to an image deterioration that makes the detection of a stroke impossible.

For the study, forward solutions were simulated on a fine 5 million element mesh with various errors on electrode position, electrode contact impedance and tissue conductivity at different frequencies. For the reconstruction the we used the frequency-difference fraction reconstruction method presented in [5] on a coarse 180k element mesh. The mesh we used included a scalp layer, a skull layer and a brain layer. We chose this simplified head geometry because we intend to reproduce the study in a tank and confirm our simulation results with experimental data.

3 Conclusions

We illustrate an application of a new fast parallel solver for the forward problem in EIT. It significantly reduces the time needed for simulation studies and EIT reconstructions on large finite element meshes. A feasibility study of frequency-difference EIT on a realistic head mesh has shown that it is very important to measure the electrodes positions with an accuracy of less than 1mm.

References

[1] Adler A, Lionheart W. *Physiological measurement* **27**(5):S25–42, 2006
[2] Horesh L, Schweiger M, Bollhöfer M. *Int J Inf Syst* ... **2**(4):532–556, 2006
[3] Jehl M, Dedner A, Betcke T, et al. http://users.dune-project.org/projects/dune-peits/wiki, 2014
[4] Malone E, Jehl M, Arridge S, et al. *Submitted to Physiological Measurement* 2014
[5] Malone E, Sato Dos Santos G, Holder D, et al. *IEEE Transactions on Medical Imaging* 1–12, 2013

A High Precision Parallel Current Drive Experimental EIT System

Jeff Ashe[1], David Shoudy[1], Gregory Boverman[1], James Sabatini[1], Tzu-Jen Kao[1], and Bruce Amm[1]

[1]General Electric Global Research, Niskayuna, NY USA, (email: ashe@ge.com)

Abstract: Our parallel current drive EIT architecture can simultaneously drive 32 independent high impedance current sources and measure 32 independent precision voltage channels. Coherent modulation and demodulation is digitally implemented using field programmable gate arrays. High accuracy and precision is achieved using custom analog circuits containing modified Howland current sources coupled to negative impedance converters.

1 Introduction

Parallel drive EIT systems afford the ability to optimize excitation patterns for maximum distinguishability vs. conventional systems employing pairwise excitations [1]. To realize the benefits of parallel drive, it is important for the design of each channel to remain stable while achieving high output impedance. The Howland current source topology, by itself, can produce either high output resistance or low output capacitance but is incapable of producing both simultaneously. Generalized impedance converters have been used for compensating the output capacitance [2]. A negative impedance converter (NIC) circuit can generate a broad range of negative compensation capacitances but is often unstable when producing a high resistance. The Howland-NIC combination can produce low output capacitance (< 1 pF) while achieving high output resistance (>40 Mohms) by adaptively tuning the circuits to a resistance cancelling operating point using the droop circuit method [3]. A drawback of the Howland-NIC topology is a relatively narrow fractional bandwidth (slightly in excess of 30%) which creates a need for switched elements for octaves or decades of bandwidth.

Our GENESIS parallel current drive EIT system (Figure 1) employs 32 Howland-NIC current sources connected to a FPGA-based acquisition system (PXI-7853R, National Instruments, 16 bits). The system supports excitations in excess of 20 frames per second wherein each frame can contain up to 64 orthogonal patterns. One-step reconstruction is performed in real-time on a frame by frame basis and the raw data is stored for offline analysis.

2 Methods

The GENESIS system was characterized using parallel resistor-capacitor networks approximating the measured impedance of large Ag/AgCl electrodes placed on skin (nominal 1 kohm and 20 nF). After offline tuning of the Howland-NIC circuits at 10 kHz, the amplitude of each current channel was linearly increased from 0 to approximately 120 uA in 64 steps. The real and imaginary voltages on each channel were measured after digital demodulation and matched filtering. The applied current for each channel was independently measured by returning the current through the virtual ground connection of an additional current to voltage converter. Voltage and current measurements were collected for 10,000 frames.

For analysis, the gain and phase drift of each frame was removed using a first order least squares fit vs. the measured current from the virtual ground. The residual error was computed using ohms law assuming the resistor-capacitor networks were constant and known. The maximum average residual error was determined to be less than 20 parts per million (slightly less than 16 bits accuracy) and the maximum signal to noise ratio was greater than 110 dB (slightly more than 18 bits precision).

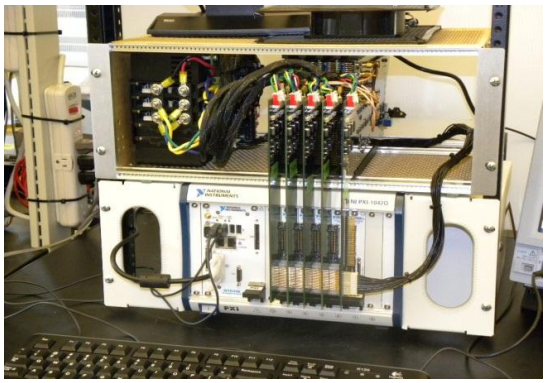

Figure 1: Parallel Current Drive GENESIS EIT System. The 32 channel experimental system employs a Howland-NIC analog circuit topology with a National Instruments FPGA digital backend for modulation and demodulation.

3 Conclusions

The GENESIS parallel current drive experimental EIT system simultaneously provides high performance to explore optimization of simultaneous current patterns for maximum distinguishability. The Howland-NIC analog circuit designs and tuning methodologies provide performance that is consistent with the accuracy and precision of the FPGA digital modulation/demodulation implementation.

References

[1] Isaacson, *IEEE Trans. Med. Imag.* **5**:92–95, 1986
[2] Ross et al, *Phys. Meas.* **24**:509–516, 2003
[3] Cook et al, *IEEE Trans. Biomed. Eng.* **41**:713-722, 1994

Discarding the Direct Component in Electrical Impedance Tomography

Michael Rapin[1,2], Martin Proença[1,3], Fabian Braun[1,3], Josep Solà[1], Pascal Olivier Gaggero[4], Andy Adler[5], Marc Correvon[1], Olivier Chételat[1]

[1]CSEM SA, Swiss Centre for Electronics and Microtechnology, Neuchâtel, Switzerland
[2]ETHZ, Swiss Federal Institute of Technology, Zurich, Switzerland
[3]EPFL, Swiss Federal Institute of Technology, Lausanne, Switzerland
[4]BFH, Institute for Human-Centered Engineering, Bienne, Switzerland
[5]Carleton University, System and Computer Engineering, Ottawa, Canada

Abstract: Several studies [1,2] have shown the potential of EIT to estimate cardiovascular parameters. To achieve this goal, EIT devices have to deal with small impedance variations. As a consequence, the high value of the direct component (DC) of the bio-impedance signal becomes an issue in terms of analog to digital converter resolution. With this research, we aim at demonstrating that the DC of the signal can be discarded before digitalization.

1 Introduction

The present research aims at studying the impact of DC signal in EIT difference image reconstruction algorithms, via simulations and actual measurements. An example of a thoracic bio-impedance measurement performed in a human subject is shown and illustrates the high dynamic range required to measure both DC amplitude and cardiogenic impedance variations. The feasibility of DC-free approach has been proven by means of simulated data based on a body-inspired model. These simulations underline the importance of filtering out low frequencies to highlight the cardiogenic signal. The results obtained via simulation have been validated with results obtained on real experimental data. Finally, a discussion describes the encouraging results found during this research.

2 Materials and method

2.1 Actual bio-impedance measurement

In vivo measurement performed in a male subject's thorax shown the very small cardiogenic impedance variation (0.5Ω) compared to the high DC value (155Ω). Such a large dynamic range requires demanding ADC resolution.

2.2 Simulations based on a body-inspired model

EIT simulations with EIDORS software [3] were performed to ensure that DC is not essential for the difference image reconstruction process. For the standard reconstruction process (Figure 1), the homogeneous set of voltages is computed once during the baseline and kept constant throughout the whole recording time. This is the main difference with the novel approach shown in Figure 2. Namely, a high-pass filter is applied in the time dimension to each voltage channel before digitalization and image reconstruction. Consequently, the homogeneous set of voltages becomes the null vector.

Raw simulation data in Figure 3 (left image) shows the result of the standard image reconstruction method. In this example, one can see the high amplitude of the breathing signal compared to cardiogenic signal. High-passed data (right image) shows that it is possible to filter out low frequencies, including DC, before image reconstruction without altering image quality of higher-frequency regions (i.e. cardiogenic signal region). The cutoff frequency of the high-pass filter has been chosen at 0.8Hz. This way, the breathing signal (0.2Hz) and the DC component of each of the voltage channels were filtered out, whereas the cardiogenic signal (1Hz) remained close to its raw value.

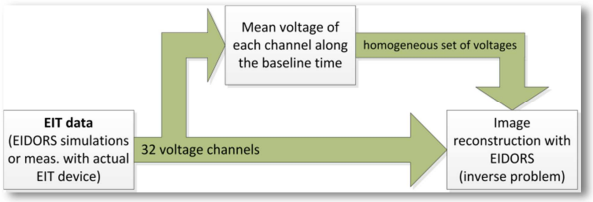

Figure 1: Standard approach for image reconstruction process.

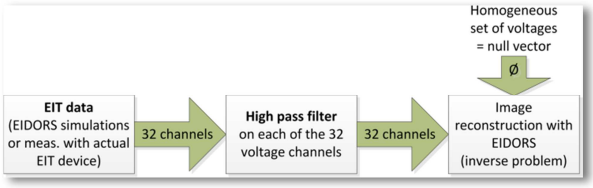

Figure 2: Novel image reconstruction process.

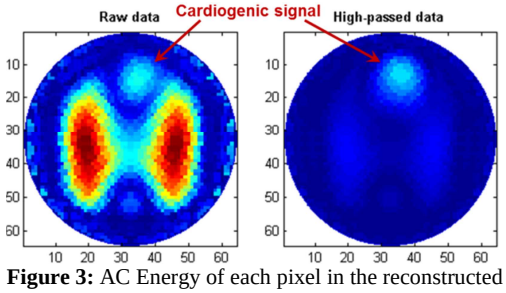

Figure 3: AC Energy of each pixel in the reconstructed image sequence without (left) and with (right) the high-pass filter.

2.3 Actual measurement

Measurements on real data have been performed, concluding that the DC of bio-impedance is not required for EIT difference image reconstruction.

3 Conclusions

In this research, we hypothesized that the zero-frequency component of the EIT voltage signal was not required to reconstruct differential images. Both simulations and actual measurements have corroborated this hypothesis by showing that the amplitude of high frequency signal was not altered whether the DC component was kept or filtered out.

4 References

[1] F. Braun Master thesis, "Systolic Time Intervals Measured by Electrical Impedance Tomography (EIT)", ETH, 2013
[2] D. Ferrario, et al., "Unsupervised localization of heart and lung regions in EIT images: a validation study," in 12th International Conference in Electrical Impedance Tomography, Bath (UK), 2011
[3] A. Adler, W. R. B. Lionheart, "Uses and abuses of EIDORS: An extensible software base for EIT", Physiol. Meas., 27, S25-S42, 2006

Use of electrical impedance tomography for the diagnosis of precancerous diseases and cancer of the cervix

O.V. Trokhanova[1], Y.A. Chijova[1], V.A. Cherepenin[2], A.V. Korjenevsky[2], T. S. Tuykin[2]

[1] Yaroslavl State Medical Academy, Yaroslavl, Russia, trokhanove@yandex.ru
[2] Institute of Radioengineering and Electronics of the RAS, Moscow, Russia

Abstract: The paper describes possibility of EIT diagnostics of precancerous diseases and cancer of the cervix. The data were obtained through EIT system GIT (gynaecological impedance tomograph) [1].

1 Introduction

Cervical cancer is one of the most frequent types of cancer. The disease is increasingly recorded in young women and is characterized by high mortality. Cervical cancer kills 290 000 women per year, which equals to 789 women per day or a woman per 2 minutes, all over the world.

There is a generally accepted classification of precursors of cervical cancer, which is based on the depth of lesions stratified squamous epithelium:
-cervical intraepithelial neoplasia grade 1 (CIN1) defeats a third of the thickness of stratified squamous epithelium;
-cervical intraepithelial neoplasia grade 2 (CIN2) captures 2/3 of the thickness of stratified squamous epithelium;
-cervical intraepithelial neoplasia grade 3 (CIN3) corrupts the whole layer of stratified squamous epithelium.

Intraepithelial lesions usually are associated with human papillomavirus (HPV) and it is considered as forerunner of cancer.

The purpose of the study is to identify opportunities of electrical impedance tomography in the diagnosis of precursors and cervical cancer.

2 Methods

The data were obtained through EIT system GIT [1] with 48 electrodes organized in non-orthogonal matrix. The external diameter of a vaginal probe is 33 mm. Images were reconstructed by a weighted 3D back-projection along equipotential sphere algorithm [2] extended by Delaine interpolation [1]. The result of GIT visualization is three slices at a depth of 2, 5 and 8 mm for 10 kHz and 50 kHz simultaneously in a real time mode (a shot per seconds). On a slice the conductivity value is presented in relative units (relative to average conductivity), that helps to calculate average value over a region and get numerical criteria of diagnostics, not only visual estimation of pictures.

The report presents main results (see table 1) of a comprehensive examination of the neck of the womb of 186 women from 19 to 70 years: 63 - without cervical pathology, 50 - with low-grade squamouse intraepithelial lesion (LSIL) CIN1, 46 – with high-grade squamouse intraepithelial lesion (HSIL) CIN2 and CIN3, 11 - cervical cancer stage 1, 16 - cervical cancer stages 2-3.

We used the following methods of diagnosis: history taking, a visual examination on the uterine speculum, liquid oncocitology, extended colposcopy, target biopsy of cervix, electrical impedance tomography of the neck of the womb.

3 Conclusions

According the preliminary results, the conductivity of cervical tissue is almost the same for intact and LSIL cases while it is slightly different from the HSIL case and is significantly different from cancer cases (see table 1). That allows us to hope that electrical impedance tomography will help: to detect precursors of cervical cancer before visual changes of cervical surface; to distinguish diseases (CIN1, CIN2, CIN3, cancer, inflammation); to control effectiveness of treatment and to detect changes associated with HPV.

References

[1] Cherepenin V A, Gulyaev Yu V, Korjenevsky A V, Sapetsky S A and Tuykin T S 2012 An electrical impedance tomography system for gynecological application GIT with a tiny electrode array *Physiol. Meas.* **33** 849 – 62
[2] Cherepenin V, Karpov A, Korjenevsky A, Kornienko V, Kultiasov Yu, Ochapkin M, Trochanova O and Meister D 2002 Three-dimensional EIT imaging of breast tissues: system design and clinical testing *IEEE Trans. Medical Imaging* **21** 662 – 7

Table 1: Conductivity is given in arbitrary units at frequency 50 kHz. MC is menstrual cycle; n is quantity of patients in a group. Transformation area is the border between two types of epitheliums (squamous and columnar) on cervix.

Cervix pathology, MC phase and patient quantity		Age before 30		Age after 30	
		2mm	Transformation area	2mm	Transformation area
Norm	1 phase of MC n = 63	0.92±0.06	1.08±0.1	0.95±0.06	1.02±0.06
	2 phase of MC n = 63	0.95±0.06	1.02±0.06	0.99±0.07	1.06±0.08
LSIL	1 phase of MC n = 50	0.91±0.04	1.0±0.04	0.96±0.02	1.07±0.04
	2 phase of MC n = 50	0.94±0.03	1.07±0.06	0.98±0.01	1.1±0.03
HSIL	1 phase of MC n = 46	0.96±0.02	1.07±0.01	1.01±0.07	1.1±0.09
	2 phase of MC n = 46	0.99±0.1	1.13±0.09	1.09±0.08	1.14±0.01
Cancer stage 1	1 phase of MC n = 11	No data	No data	1.03±0.03	1.18±0.04
	2 phase of MC n = 11	No data	No data	1.03±0.03	1.18±0.04
Cancer stage 2-3	1 phase of MC n = 16	0.65±0.01	Not applicable	0.79±0.1	Not applicable
	2 phase of MC n = 16	0.65±0.01	Not applicable	0.79±0.1	Not applicable

A Comparison of Two Regularization Methods Based on the Sussex EIM MK4 System

Xiaolin Zhang[1] Chris Chatwin[1] and Wei Wang[2]

[1]University of Sussex, Brighton, UK, xz68@sussex.ac.uk

[2]Micro Image UK Ltd, UK, w97wang@yahoo.co.uk

Abstract: A comparison of two regularization methods: the general regularization method and the Sheffield method using the voltage ratio rather than the difference.

1 Introduction

The Sussex MK4 is a 3D EIT system for breast cancer detection, using current excitation and voltage measurements. The data acquisition is completed by a planar electrode array at the bottom of the tank in the MK4. In experiments, two groups of measurements are collected: the reference measurements which are from a tank of saline and the actual measurements which are from a patient with a breast placed in the tank. For detailed information of the MK4, please refer to [1] (page 44-49). The aim of this paper is to compare the two regularization methods shown in Section 2.

2 Methods

The vector c_0 denotes the initial conductivity, which is the saline in the tank; the vector V_0 denotes the measurements of the saline; the vector c_{ref} denotes the reference conductivity, which could be c_0 or the conductivity with some known anatomical features; the vector C denotes the actual conductivity, with a breast in the tank; the vector V_m denotes the actual patient measurements. Defining $\Delta c = C - C_{ref}$, $\Delta V = V_m - V_{ref}$, the general regularization method for the EIT inverse problem is:

$$\begin{cases} \Delta c = (S^*S + \alpha^2 I)^{-1}\left(S^*\Delta V + \alpha^2 I\left(c_{ref} - c_0\right)\right) \\ c = c_{ref} + \Delta c \end{cases} \quad (1)$$

where S is the Jacobin matrix, α is the regularization parameter, I is the identity matrix. For the details, please refer to [1] page 62-65 and [2] page 21. The Sheffield group uses the logarithm of the voltage ratios rather than the difference to do image reconstruction.

$$\begin{cases} \Delta lnc = (F^*F + \alpha^2 I)^{-1}\left(F^*\Delta lnV + \alpha^2 I\left(lnc_{ref} - lnc_0\right)\right) \\ lnc = lnc_{ref} + ln\Delta c \end{cases} \quad (2)$$

where $\Delta lnV = \left[\ln\left(\frac{V_{m1}}{V_{01}}\right); \cdots; \ln\left(\frac{V_{mM}}{V_{0M}}\right)\right]$, $\Delta \ln c = [\ln\left(\frac{c_1}{c_{ref1}}\right)$ $; \cdots; \ln\left(\frac{c_E}{c_{refE}}\right)]$, $F_{ij} = \frac{1}{V_{refj}}.S_{ij}.C_{refi}$, M and E indicate the number of measurements and the number of the mesh elements (refer to [1] page 65-67 and [2] page 370).

To compare the two algorithms, a cylindrical model is employed in Figure 3. The conductivity of the object is 0.8 mS/cm and the conductivity of the surrounding saline is 0.5 mS/cm. The SNR of the simulated measurements is 60dB. The L-curve is employed to decide α. α at the global corner is the optimized trade-off between the noise and image quality (Figure 1, 3), thus the optimized α for (1) and (2) are $\alpha^2 = 2$ and $\alpha^2 = 0.08$. The results corresponding to the optimized α are shown in Figure 2, 4. The images from left to right indicates the bottom, middle and top reconstructed conductivity.

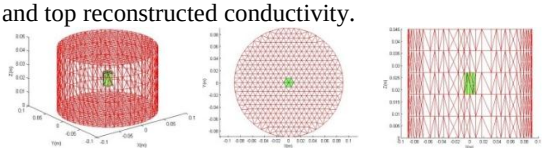

Figure 3: Model: 3D view, XY view and XZ view

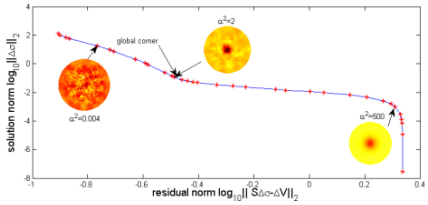

Figure 4: L-curve of the general regularization method

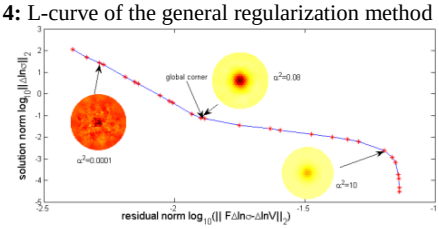

Figure 5: L-curve of the Sheffield method

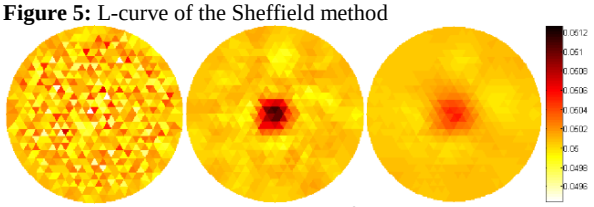

Figure 6: Result from Equation (1), $\alpha^2 = 2$.

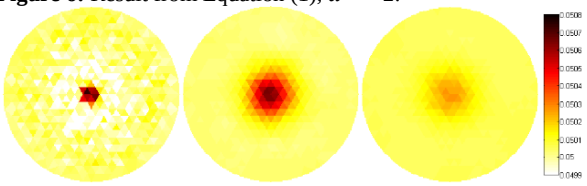

Figure 7: Result from Equation (2), $\alpha^2 = 0.08$.

3 Conclusions

For the Sussex MK4 system, at an optimised α, the general regularization method gives a better performance in distinguishing the object from the background but has less noise tolerance. The Sheffield algorithm is more robust to noise.

References

[1] G. Sze, "Detection of breast cancer with electrical impedance mammography," Doctoral thesis, Engineering and Design, University of Sussex, 2012.

[2] D. C. Barber, "EIT: The view from Sheffield," Electrical impedance tomography : methods, history and applications, D. S. Holder, ed., pp. 348-371, Bristol: Institute of Physics, 2005.

Validity of Using the Sheffield Algorithm for the Sussex EIT MK4

Xiaolin Zhang[1], Tabassum Qureshi[1], Chris Chatwin[1] and Wei Wang[2]

[1]University of Sussex, Brighton, UK, xz68@sussex.ac.uk

[2]Micro Image UK Ltd, UK, w97wang@yahoo.co.uk

Abstract: This paper introduces the image reconstruction algorithm from Sheffield group and the validity of this algorithm to the Sussex MK4.

1 Introduction

The Sussex MK4 electrical impedance mammography (EIM) is developed for breast cancer detection[1][2]. This paper is focusing on the validity analysis of using the Sheffield algorithm for the MK4.

2 Methods

The widely used equation to explain the relationship between the change of the conductivity and the change of the boundary voltage measurements is:

$$\Delta V = V_m - V_{ref} = S(C - C_{ref}) = S\Delta C \qquad (1)$$

where S is the Jacobin matrix. $\partial V_j/\partial C_i = S_{ij}$. Vector V_m denotes the real voltage measurement corresponding to the real conductivity C. Vector V_{ref} denotes the reference voltage measurements corresponding to the reference conductivity C_{ref}. S is a function of C. As C changes, S changes. Eq. (1) is based on the assumption that the changes of C are small, so that the changes of S can be ignored. However Eq. (1) was proven by us to have a poor noise tolerance for the MK4, thus the Sheffield method using the voltage ratio rather than the difference is employed [3]: (For details, please read [3], Page 368-371)

$$\Delta \ln V = F \Delta \ln C \qquad (2)$$

where $\Delta \ln V_i = \ln(V_{mi}/V_{refi})$, $\Delta \ln C_i = \ln(C_i/C_{refi})$.

$$\frac{\partial \ln(V_j)}{\partial \ln(C_i)} = \frac{\partial \ln(V_j)}{\partial V_j} \cdot \frac{\partial V_j}{\partial C_i} \cdot \frac{\partial C_i}{\partial \ln(C_i)} = \frac{1}{V_j} S_{ij} C_i = F_{ij} \qquad (3)$$

The image reconstruction algorithm is:

$$\begin{cases} \Delta \ln(C) = (F^* F + \alpha^2 I)^{-1} F^* \left(\ln(V_m) - \ln(V_{ref})\right) \\ \ln(C_{ref}) = \ln(C) + \Delta \ln(C) \end{cases} \qquad (4)$$

where α is the regularization parameter, I is the identity matrix. Let's see Eq. (3). As V and S are both determined by C, basically F is determined by C. As C changes, F changes. So this algorithm is based on the assumption that the changes of F are ignored when the changes of the conductivity are sufficiently small. However how much changes of the conductivity will make the assumption invalid? According to Eq. (3), if V_j is equal or close to 0, F_{ij} will go to infinity, which will make the algorithm unavailable. In practice, the measurements from the 0.5 mS/cm saline are used as the reference measurements and in each excitation, we only use at most 12 strongest measurements which are collected parallel to the electric field [1][2], therefore V_j won't be close to 0. However if there are big changes of conductivity, V_j may be close to 0, then Eq. (2)-(4) becomes invalid.

This section discuss how much changes of the conductivity will make Eq. (2)-(4) invalid. See Figure 1. The positive pole of the current source is at the yellow dot S+ and the negative pole of the current is at the yellow dot S-. The electric potential at P1, P2, P3, P4 is denoted by: $\emptyset_1, \emptyset_2, \emptyset_3, \emptyset_4$ and the voltage measurements between P2 and P1, P4 and P3 are denoted by V_{21}, V_{43}. For an uniform field (0.5 mS/cm Saline), according to our study, V_{21}, V_{43} are approximately 300mv when the tank height is 4.5cm. For a significant changes of the field, $\emptyset_1$ and $\emptyset_3$ may get close to $\emptyset_2$ and $\emptyset_4$, which means V_{21}, V_{43} may become 0 even negative. then Eq. (2)-(4) will be invalid. Thus, we conclude that the changes of the conductivity which cause $V_{21} \leq 0$ or $V_{43} \leq 0$ will make Eq. (2)-(4) invalid. If $V_{21} \leq 0$, there must be a high conductivity path between S+ and P1, so that most of the current flows through this path and brings up $\emptyset_1$. See Figure 1. The most likely condition to make $V_{21} \leq 0$ or $V_{43} \leq 0$ is that the high conductivity path needs 1) the shortest distance between S+ and P1 without covering P2; 2) a big volume of the path to reduce the resistance between P1 and S+; 3) a much higher conductivity than the surrounding background. We made such a path shown in Figure 1. W=5.5cm, L=5.2cm, H=0.9cm. The straight-line distance between P1 and S+ is 4.5 cm. σ_1 and σ_2 indicate the conductivity of the background and the path. According the our studies, only if $\sigma_2/\sigma_1 > 44$ is $V_{21} \leq 0, V_{43} \to 0^+$ Therefore in a real case, if the tumour size is smaller than 4.5cm, which means the high conductive path can't form and the conductivity contrast of the whole tank is smaller than 40, Eq. (2)-(4) will be valid. Practically, a 4.5cm tumour can be found easily, and it is not usual that the conductivity contrast of a breast is bigger than 40.

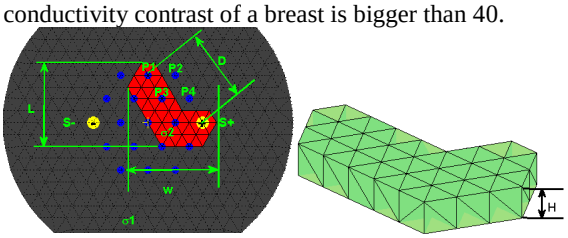

Figure 1: Voltage measurements reverse analysis

3 Conclusions

The Sheffield algorithm is not valid for every condition. For the MK4 system, it is available, for a real breast is too far from the conditions which make the boundary voltage measurements close to 0, hence invalidating Eq. (2)-(4).

References

[1] B. Nevis, "An investigation into combining electrical impedance mammography with 3D ultrasound for breast cancer detection," Doctoral thesis, Engineering and Design, University of Sussex, 2013.

[2] G. Sze, "Detection of breast cancer with electrical impedance mammography," Doctoral thesis, Engineering and Design, University of Sussex, 2012.

[3] D. C. Barber, "EIT: The view from Sheffield," Electrical impedance tomography : methods, history and applications, D. S. Holder, ed., pp. 348-371, Bristol: Institute of Physics, 2005.

Session 8

Lung EIT

25 April 2014, 10:45 – 12:00

Comparison between regional lung CT values and lung densities estimated using EIT

Satoru Nebuya[1], Tomotaka Koike[2], Hiroshi Imai[3], Yoshiaki Iwashita[3],
Niranjan Khambete[4], Hiroshi Kumagai[1], Kazui Soma[5]and Brian H. Brown[6]

[1]Graduate School of Medical Sciences, Kitasato University, Kanagawa, Japan, nebuya@kitasato-u.ac.jp
[2] Kitasato University Hospital, Kanagawa, Japan [3]Department of Medicine, Mie University, Mie, Japan
[4]Deenanath Mangeshkar Hospital and Research Centre, Pune, India [5]Department of Medicine, Kitasato University, Kanagawa, Japan
[6]Department of Clinical Engineering, University of Sheffield, Sheffield, United Kingdom

Abstract: In this paper we report the results of our study in which we compared lung density values obtained from EIT and CT values (HU) within a region of interest. The purpose was to verify clinical use of lung density estimation using EIT data. Image resolution of CT images, which was originally 512*512 pixels, was changed to 16*16 pixels, to match that of the EIT images. The CT and EIT images were recorded from eight patients in an intensive care unit and the results showed a correlation coefficient of 0.66 ($p<0.05$) between the CT values (HU) and the lung density values (kg/m^3) obtained from EIT.

1 Introduction

Electrical Impedance Tomography (EIT) has become a feasible technique to evaluate lung function [1]. However, it is yet to be considered as a clinically acceptable method for evaluation of lung density. We had proposed the use of 'lung density' as an absolute measure of lung function using EIT data sets, but had not compared it with clinical results from patients with lung disease. In this study, CT values (HU) and lung density (kg/m^3), though representing different physical properties of lung tissue, were compared to verify the feasibility of using lung density values for clinical monitoring of lung disease.

2 Methods

Eight patents, connected to a ventilator, were studied by recording CT and EIT images within 24 hours of each other. Shefield Mk3.5 [3] EIT system with 8 electrodes and 16*16 image resolution was used in this study. To achieve pixel by pixel comparison between CT values and lung densities, the thorax shape of the CT image was deformed to be circular and its spatial resolution, which was originally 512*512 pixels, was changed into 16*16, similar to that of EIT. EIT was reconstructed with the Sheffield back projection method using a sensitivity matrix [4]. The lung density at each pixel was estimated using 1 minute data set, measured at four frequencies between 2 kHz and 768 kHz. A region of interest (ROI) over the lungs was chosen manually. We calculated the correlation coefficient between the CT values (HU) and lung densities (kg/m^3) in all of subjects.

3 Results and discussions

Figure 1 shows a result of comparison between CT value and lung density in one patient. They are in reasonable agreement around both lung collapsed and consolidated regions. All the data from eight patients is plotted in Figure 2. The correlation coefficient was 0.66 ($p<0.05$) between CT value and lung density and can be considered acceptably high. However, deformation of the thorax shape into a circular shape and manual determination of the ROI are likely to have introduced errors. Furthermore, we could not make both CT and EIT measurements on the same day because of the limited availability of ICU clinical staff required to be present. The extent of the lung disease is likely to have changed between the measurements and so would have reduced the correlation between the CT and EIT measurements related to lung density.

Although the CT values and lung density are not directly comparable, the results of this study suggest that lung density could be a feasible index to evaluate lung disease. Further experiments need to be carried out to verify this finding by increasing the number of patients.

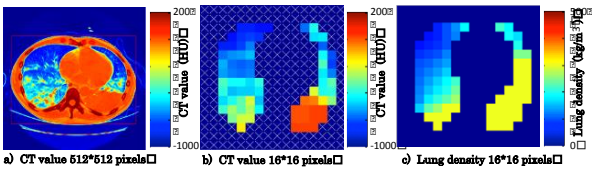

Figure 1: An example of comparison between CT values (HU) and Lung density (kg/m^3) in a patient.

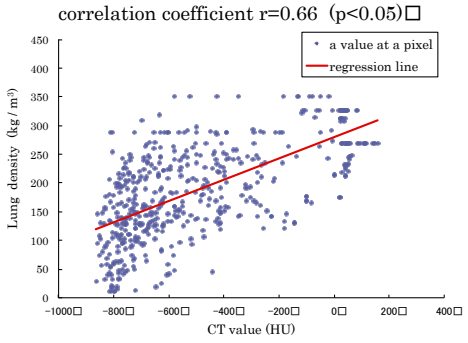

Figure 2: Relationship between CT values (HU) and Lung density (kg/m^3) in eight patients.

References

[1] Adler A, Amato MB, Arnold JH *et. al.*, Whither lung EIT: where are we, where do we want to go and what do we need to get there? *Physiol Meas.***33**: 679-94, 2012.
[2] Nebuya S, Mills GH, Miles P, Brown BH, Indirect measurement of lung density and air volume from electrical impedance tomography (EIT) data.*Physiol Meas.***32**: 1957-67, 2011.
[3] Wilson AJ, Milnes P, Waterworth AR *et. al.*, Mk3.5: a modular, multi-frequency successor to the Mk3a EIS/EIT system. *Physiol Meas.***22**: 49-54, 2001.
[4] P. Metherall, Barber DC, Smallwood RH *et. al.*: Three-dimensional electrical impedance tomography, *Nature*, **380**, 509-12, 19

Assessment of tidal recruitment and overdistension by regional analysis of respiratory system compliance at different tidal volumes

Tobias Becher, Timo Meinel, Daniel Bläser, Günther Zick, Norbert Weiler, Inéz Frerichs

Department of Anaesthesiology and Intensive Care Medicine, University Medical Centre Schleswig-Holstein, Campus Kiel, Kiel, Germany, tobias.becher@uksh.de

Abstract: In this pilot clinical study, we assessed the effects of positive end-expiratory pressure (PEEP) on tidal recruitment and overdistension in mechanically ventilated patients. Changes in EIT-derived regional respiratory system compliance (C_{rs}) induced by variation of tidal volume (V_T) were analysed in the chest cross-section and identified the simultaneous occurrence of tidal recruitment and overdistension in the examined patients.

1 Introduction

Tidal recruitment associated with cyclic opening and closing of alveoli and alveolar overdistension are important mechanisms in the genesis of ventilator-induced lung injury [1]. One promising method for detection of these phenomena is the calculation of regional C_{rs} in individual image pixels [2] or as profiles in 32 horizontal chest layers [3].

When a patient is ventilated with two different values of V_T and regional C_{rs} is calculated in each setting, the differences in regional C_{rs} induced by the V_T variation can be determined. In the present paper, we used this approach to quantify the amount of tidal recruitment and overdistension by calculating the V_T-dependent changes in C_{rs} at two PEEP values on a pixel-by-pixel basis.

2 Methods

We performed a retrospective analysis of data from five critically ill patients (4 male, 1 female, 74±6 years (mean age±SD)) with acute respiratory distress syndrome (ARDS). The patients were ventilated in a volume-controlled mode at two different PEEP values ($PEEP_{high}$, $PEEP_{low}$). As described in [2], $PEEP_{high}$ and $PEEP_{low}$ were set individually in each patient based on the analysis of a quasi-static pressure-volume manoeuvre. For the diagnosis of tidal recruitment and overdistension, a variation of V_T between a high value of 10 ml/kg ideal body weight (IBW) and low value of 6 ml/kg IBW was performed at both PEEP values.

EIT measurements were carried out with the Goe-MF II device (CareFusion, Höchberg, Germany) using a set of 16 electrodes (L-00-S, Ambu, Ballerup, Denmark). EIT images were generated using the back-projection algorithm.

Regional C_{rs} was calculated by dividing the individual pixel values of tidal amplitude of relative impedance change (rel.ΔZ) by the sum of all these values and by multiplying them with the global C_{rs}. The regional C_{rs} values at low V_T were subtracted from the respective values with high V_T to generate difference images, visualising ΔC_{rs} between high and low V_T in every pixel (Fig.1). For quantitative estimation of tidal recruitment and overdistension, we calculated the sum of pixels with positive values of ΔC_{rs} and divided the resulting value by the global C_{rs} at high V_T. This analysis rendered a dimensionless index value of the amount of tidal recruitment that was finally multiplied by 100 to yield a value in %. This was performed similarly for all pixels with negative values of ΔC_{rs} to create an index value of alveolar overdistension.

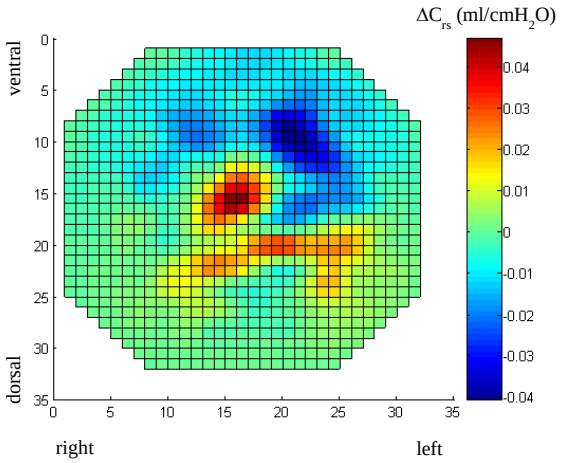

Figure 1: Map of regional differences in respiratory system compliance (ΔC_{rs}) between high and low V_T at the high positive end-expiratory pressure ($PEEP_{high}$) in one of the examined patients. Positive values imply tidal recruitment, whereas negative values show overdistension. At this PEEP level, 10% overdistension and 6% tidal recruitment were identified in this patient.

3 Results

Tidal recruitment and alveolar overdistension occurred simultaneously at both PEEP levels in all studied patients. At $PEEP_{high}$, we found a non-significant reduction in tidal recruitment (11% vs 14%; p=n.s.) and a non-significant increase in overdistension (18% vs 11%; p=n.s.) in comparison with $PEEP_{low}$.

4 Conclusions

Analysis of changes in EIT-derived regional C_{rs} between high and low V_T is feasible in mechanically ventilated patients and may be used to quantify the overall amount of tidal recruitment and overdistension at a given PEEP. This might be used for an individualized optimization of PEEP and V_T setting adapted to the regional respiratory system mechanics.

References

[1]Caironi P et al. *Am J Respir Crit Care Med* **181**: 578-86, 2010
[2]Costa EL et al. *Intensive Care Med* **35**: 1132-7, 2009
[3]Zick G et al. *PLoS One* **8**: e72675, 2013

Spontaneous effort causes occult Pendelluft during mechanical ventilation

Yoshida T[1, 2]; Torsani V[2]; Gomes S[2]; De Santis RR[2]; Beraldo M[2]; Tucci MR[2]; Zin WA[3]; Kavanagh BP[4]; Amato MBP[2]

[1]Department of Anesthesiology and Intensive Care Medicine, Osaka University Graduate School of Medicine, Suita, Japan
[2]Laboratório de Pneumologia LIM–09, Disciplina de Pneumologia, Heart Institute (Incor) Hospital das Clínicas da Faculdade de Medicina da Universidade de São Paulo, São Paulo, Brazil
[3]Instituto de Biofísica Carlos Chagas Filho, Universidade Federal do Rio de Janeiro, Rio de Janeiro, Brazil
[4]Departments of Critical Care Medicine and Anesthesia, Hospital for Sick Children, University of Toronto, Toronto, Canada
takeshiyoshida@hp-icu.med.osaka-u.ac.jp

Abstract: In the injured lung, local negative pleural pressure generated by diaphragmatic contraction is not uniformly transmitted, but is concentrated in dependent lung. This causes Pendelluft (using EIT), with shift of air from non-dependent to dependent lung regions. Thus, during lung-protective ventilation with strictly limited tidal volume, the presence of strong inspiratory effort can result in a hidden, local over-stretch of the dependent lung.

1 Introduction

In normal lungs, local changes in pleural pressure (P_{pl}) are generalized over the whole pleural surface. However, in a patient with injured lungs, we observed (using EIT) a Pendelluft phenomenon, *i.e.* movement of air within the lung from non-dependent to dependent regions without change in tidal volume that was caused by spontaneous breathing during mechanical ventilation. We hypothesized that in injured lungs: negative P_{pl} generated by diaphragm contraction has localized effects (in dependent regions) that are not uniformly transmitted; and such localized changes in P_{pl} cause Pendelluft.

2 Methods

In seven lavages-injured pigs, EIT data were recorded during spontaneous breathing and muscle paralysis, comparing the temporal pattern and distribution of regional ventilation with the sub-division of the thorax into four zones (ventro-dorsal). For the validation of regional distribution of ventilation, dynamic CT scans were performed to evaluate the absolute movement of air within thick slice. We also measured negative P_{pl} in dependent lung directly using intra-pleural catheters. Further, we estimated the additional airway pressure required to achieve comparable dependent lung inflation in the presence of muscular paralysis by titrating inspiratory airway pressures during paralysis till observing the same delta-Z observed during spontaneous breathing in dependent zones.

3 Results

In all lung-injured animals, spontaneous breathing caused Pendelluft, which was associated with more negative local P_{pl} in dependent regions *vs.* esophageal pressure (-14.3±3.3 *vs.* –7.1±2.1 cmH_2O, P<0.01). During paralysis, there was heterogeneous —but simultaneous— inflation in the dependent as well as in the non-dependent lung regions (Figure 1). Dynamic CT analysis also confirmed the Pendelluft. Continuous recording of EIT was made during the transition from spontaneous effort to complete muscle paralysis (following a bolus of succinylcholine chloride; Figure 2); this demonstrated that the extent of the Pendelluft was proportional to the intensity of the respiratory effort. Comparable over-inflation of dependent lung during paralysis required almost 3-fold greater driving pressure (and tidal volume) *vs.* spontaneous breathing (28.0±0.5 *vs.* 10.3±0.6 cmH_2O, P<0.01; 14.8±4.6 *vs.* 5.8±1.6 mL/kg, P<0.05).

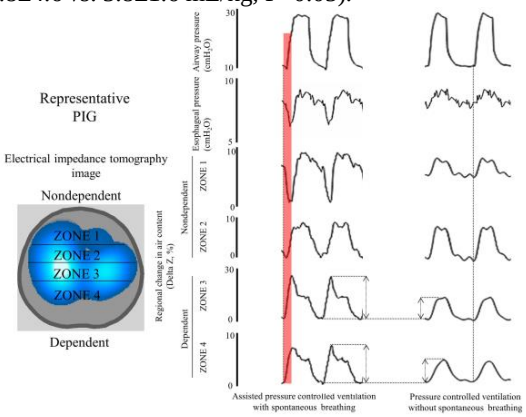

Figure 1: EIT Waveforms in Experimental Lung Injury - Spontaneous vs. Ventilator Breaths

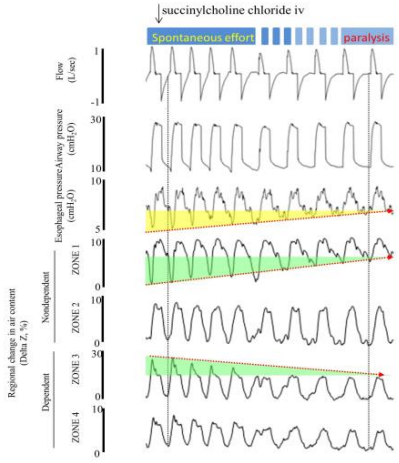

Figure 2: EIT Waveforms in transition from spontaneous breathing to muscle paralysis

4 Conclusions

Pendelluft may constitute a novel mechanism of ventilator–induced lung injury. The observed overstretch of the dependent lung could cause occult local injury, which cannot be detected (and therefore avoided) using conventional monitoring.

Detection of the Upper Airway Obstruction using Electrical Impedance Tomography

Sang-Wook Kim[1,2], Tong In Oh[3], Ohin Kwon[4] and Eung Je Woo[3]

[1]Institute of Health Sciences, Gyeongsang National University, [2]Department of Otorhinolaryngology, Gyeongsang National University Hospital, Jinju, [3]Department of Biomedical Engineering, Kyung Hee University, Kyungki, and [4]Department of Mathematics, Konkuk University, Seoul, Republic of Korea

astroflower77@hanmail.net or tioh@khu.ac.kr

Abstract: Obstructive sleep apnea (OSA) is caused by the occlusion of the upper airway. No real-time imaging technique, which can detect such occlusion during natural sleep, exists at the moment. The surface electrodes were attached on the face and neck, and then changes in the conductivity image of the upper airway were successfully detected.

1 Introduction

Apnea means the cessation of respiration lasting longer than 10 seconds during sleep. Obstructive sleep apnea is caused by repetitive occlusion of the upper airway, and it is diagnosed when apnea occurs ≥5 times/h. It has numerous complications such as hypertension, cardiac arrhythmia, ischemic heart disease, strokes and even mortality [1]. Despite several treatment modalities including the surgery, oral appliance, and continuous positive airway pressure device are used, overall control rate of OSA is not satisfactory. One of the main reasons is the absence of a real-time monitoring technique which can detect the upper airway obstruction during natural sleep. In the preliminary study, we ascertained the feasibility of the electrical impedance tomography (EIT) as a real-time monitoring tool for the upper airway obstruction [2].

2 Methods

2.1 Simulation study

In order to assess the potential of detection or feature extraction from the reconstructed impedance images or measurement data set, we generated the patient-specific FEM model based on the MR images. We segmented skin, muscle, spinal code, tongue, upper airway and teeth in the lower head. The conductivity in the literature was assigned into the each part of model. External boundary surface electrodes were placed in a ring.

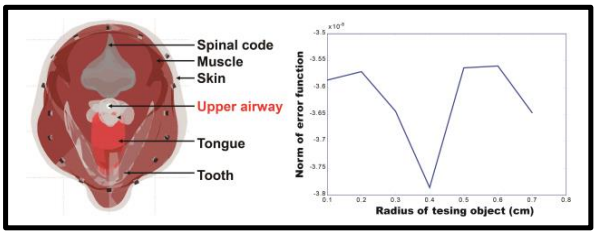

Figure 2. Patient-specific FEM model and size estimation of the upper airway

We assumed that the radius of upper airway was 0.4 cm, and computed the forward solution from the model. Concurrently, we calculated the norm of error function between the patient-specific forward data and pseudo data generated from the simple circular model when changing the radius of testing object. As shown in Figure 1, we can estimate the size of upper airway in the complicated anatomical model.

2.2 Pilot human experiment

We attached small Ag-AgCl electrodes around the upper neck of healthy male subject (28 yr). The upper airway is kept open during normal respiration. Transient airway occlusion was induced by the swallowing maneuver, and then we obtained the reference data. We produced the impedance images when the upper airway was open or closed using the KHU Mark2.5 EIT system [3]. Figure 2 shows the electrode position on the subject and the reconstructed impedance images overlapped on the MR images obtained from the same subject.

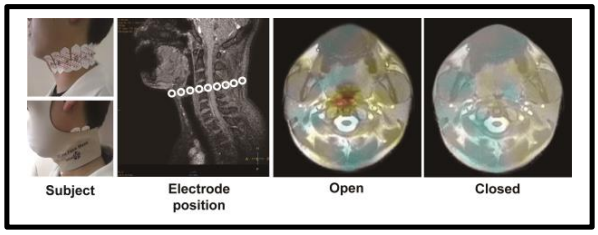

Figure 1. Pilot human experimental results

3 Conclusions

Based on our simulation and experimental studies, we can detect the status of airway and estimate its size when comparing the simulated model. Although further human studies are needed in natural sleep status, the EIT is presumed to be a useful tool to detect the upper airway occlusion which occurs during natural sleep in patients with OSA.

References

[1] L. F. Drager, S. M. Togeiro, V. Y. Polotsky, and G. Lorenzi-Filho. *J Am Coll Cardiol* **62**:569-576, 2013

[2] T. Muders, H. Luepschen, and C. Putensen. *Curr Opin Crit Care* **16**: 269-275, 2010

[3] H. Wi, H. Sohal, A.L. McEwan, E.J. Woo, T.I. Oh *IEEE T. Biomed. Circ. S.* on-line published.

Optimizing PEEP in ARDS: comparison of diverse EIT parameters

Michael Czaplik[1,2], Ingeborg Biener[1], Andreas Follmann[1], Rolf Rossaint[1], Steffen Leonhardt[2]

[1]Department for Anaesthesiology, University Hospital RWTH Aachen, Germany
[2]Department of Medical Information Technology, RWTH Aachen University, Germany

Abstract: Although EIT is a promising technique optimizing ventilator settings, the best approach that leads to an improved clinical outcome is still unknown. Against the background that diverse EIT derived parameters have been published in the last years, clinical studies focusing on defined outcome parameters have to clarify pros and cons of these measures. The aim of this study was to compare several EIT parameters in an animal trial of ARDS.

1 Introduction

Regarding intensive care medicine, EIT is a promising technique optimizing ventilator settings particularly in severely diseased patients suffering from Acute Respiratory Distress Syndrome (ARDS). To ensure a so-called protective ventilation, optimal PEEP settings are crucial. Although EIT enables to visualize ventilation and manoeuvre-dependent changes in air distribution such as stepwise PEEP variation, the optimal target parameter or clinical proceeding are unknown. This study aims to compare already published and new parameters in an animal model of ARDS and to correlate them with common clinical outcome parameters.

2 Methods

The study was approved by the German governmental institution (84-02.04.2012.A173). It was carried out considering the declaration of Helsinki in the care and use of animals. In this trial 6 pigs weighting 33.7 kg (30-36.1 kg) were used. After an initial measurement, experimental ARDS was induced in a double-hit approach. First, surfactant has been washout by repeated lavages. Second, tidal volume was increased to 20 ml/kg body weight leading to a ventilator induced lung injury. Periodic measurements of hemodynamics, blood gas analysis and EIT recording were performed at fixed points in time over 24 hours after established ARDS ("ALI1" to "ALI25"). After ALI1, randomization to either EIT or control group was carried out. At each point in time, FiO_2 setting was adapted to the current pO_2 measure obtained from blood gas analysis (target: 55-80 mmHg). In the control group, PEEP was set according to ARDS network table (table 1).
In EIT group, a PEEP trial was performed: PEEP was changed as follows: +4, +2, 0, -2, -4 cmH_2O. After a two minutes equilibration period, an EIT sequence of 1 min was recorded and diverse parameters were calculated using MATLAB for each step: (1) center of gravidy [1], (2) Impedance Ratio [2], (3) Global inhomogeneity index [3], (4) Regional Ventilation Delay Index [4], (5) Difference in end-expiratory lung impedance [5], (6) Hyperdistension and collaps index [6]. EIT was defined to be best when Global Inhomogeneity Index was lowest that means when regional ventilation was as homogenous as possible.
Post mortem, (1) wet-to-dry ratios were assessed using lung tissue samples and (2) histopathologic measurements were performed.

3 Results

The described double hit approach led to a severe ARDS in all animals. All control pigs survived the entire study whereas two animals from the EIT group died 8 hours after presence of ARDS. PEEP was significantly higher in the EIT group (21.7 vs. 8.5 mbar, $p<0.0001$) leading to a higher peak inspiratory pressure (PIP) as well (47.0 vs. 34.4 mbar, $p<0.0001$). Although the EIT-guided PEEP setting obviously led to a more individual setting, it seems to be insufficient to solely focus on homogenous distribution of ventilation by using the GI index. In most cases high PEEPs led to high homogeneity but also to overdistension. It should be wise to limit PEEP e.g. by considering overdistension index. In histophathologic analysis it could clearly be seen that all lung tissue samples showed oedema, atelectasis and haemorrhage. A tendency towards less alveolar oedema and pronounced barotrauma was determined in EIT group as compared to the control group.

4 Conclusions

A combination of overdistension and homogeneity-related indexes should be used for optimizing PEEP settings.

References

[1] Spontaneous Breathing During General Anesthesia Prevents the Ventral Redistribution of Ventilation as Detected by Electrical Impedance Tomography
[2] I. Frerichs, P. A. Dargaville, H. van Genderingen, D. R. Morel, and P. C. Rimensberger, "Lung volume recruitment after surfactant administration modifies spatial distribution of ventilation," Am. J. Respir. Crit. Care Med., vol. 174, no. 7, pp. 772–779, Oct. 2006.
[3] Z. Zhao, K. Möller, D. Steinmann, I. Frerichs, and J. Guttmann, "Evaluation of an electrical impedance tomography-based Global Inhomogeneity Index for pulmonary ventilation distribution," Intensive Care Med., vol. 35, no. 11, pp. 1900–1906, Nov. 2009.
[4] Muders T, Luepschen H, Zinserling J, et al. Crit Care Med, vol. 40, no. 3, 2012
[5] Lung volume calculated from electrical impedance tomography in ICU patients at different PEEP levels
[6] Bedside estimation of recruitable alveolar collapse and hyperdistension by electrical impedance tomography

Table 1: Tandem settings of FiO_2 and PEEP. To ensure objectivity, the mean was selected from the published PEEP range (Brower RG et al., 2004).

FiO_2	0,3	0,4	0,5	0,6	0,7	0,8	0,9	1,0
PEEP	5	6 [5-8]	9 [8-10]	10	12 [10-14]	14	17[16-18]	21[18-24]

Session 9

Chest EIT

25 April 2014, 13:30 – 14:45

Comparing belt positions for monitoring the descending aorta by EIT

Fabian Braun[1,5], Martin Proença[1,5], Michael Rapin[1], Bartłomiej Grychtol[2], Martin Bührer[3], Peter Krammer[4], Stephan H. Bohm[4], Mathieu Lemay[1], Josep Solà[1], Jean-Philippe Thiran[5,6]

[1]Systems Division, Swiss Center for Electronics and Microtechnology (CSEM), Neuchâtel, Switzerland, fbn@csem.ch
[2]Division of Medical Physics in Radiology, German Cancer Research Center (DKFZ), Heidelberg, Germany
[3]Institute for Biomedical Engineering, University and ETH Zurich, Zurich, Switzerland
[4]Swisstom AG, Landquart, Switzerland
[5]Signal Processing Laboratory (LTS5), Swiss Federal Institute of Technology (EPFL), Lausanne, Switzerland
[6]Department of Radiology, University Hospital Center (CHUV) and University of Lausanne (UNIL), Lausanne, Switzerland

Abstract: In electrical impedance tomography, the impedance changes stemming from the descending aorta contain valuable information for haemodynamic monitoring. However, the low signal strength necessitates an optimal measurement setup. Among different belt positions investigated in this work, a transversal and low placement is the best choice for detecting signals of the descending aorta.

1 Introduction

The intra-thoracic impedance changes measured by Electrical Impedance Tomography (EIT) are primarily used to monitor ventilation. In contrast, cardiovascular monitoring by EIT is still in its infancy [1]. Nonetheless, recent studies provide experimental evidence that blood pressure [2] and stroke volume variations [3] can be estimated non-invasively and continuously with this low-cost technique. Both of the aforementioned approaches exploit impedance changes originating from the descending aorta.

To the best of our knowledge, little is known about the most appropriate configuration for reliable detection of the low amplitude aortic signals. Therefore, this work aims to answer these questions by evaluating impedance changes of the descending aorta at a variety of belt positions and under different heart and lung conditions.

2 Methods

Based on MR images of a human volunteer [4] a 3D thoracic bio-impedance model was created. While the lungs and the heart were modelled as static structures, the aorta was modelled as a dynamic structure with constant conductivity, composed of thirty cylindrical segments. The radii of these segments were extended individually, thus simulating the aortic distension caused by the propagation of an aortic pressure pulse.

To investigate the influence of belt position, four cases were distinguished by placing the belt (i) in a transversal plane between vertebra Th8 and Th9 (TM), (ii) 5cm below TM (TL), (iii) 5 cm above TM (TH). Lastly (iv), the TM belt was tilted by 15° from transverse to coronal to obtain an oblique placement (OM) as recommended for cardiac EIT imaging [5].

One full cardiac cycle was then simulated by modulating conductivities and structures as follows:

- The aortic radii were extended up to 15% according to real aortic blood pressure readings.
- The conductivity of the lungs remained unchanged.
- The heart conductivity was modulated according to real blood volume readings. The maximal change was varied to achieve different signal-to-noise ratios (SNR): *e.g.* an SNR of 0.1 represents a ten-fold higher overall image amplitude originating from the heart compared to the one from the aorta.

All simulations were performed using Netgen and the EIDORS toolbox with GREIT for reconstruction [6].

2.1 Performance Evaluation

Each pixel of the simulated EIT images was correlated with the known modulation signals from the aortic radii and heart conductivity. A figure of merit (FOM) was then calculated as the sum of root mean square amplitude (A_{RMS}) of the descending aorta pixels normalized by the total sum of A_{RMS} within the whole image. In other words, this FOM shows how much (in percent) of the overall signal originates from the descending aorta.

3 Results

Figure 1 shows the best performance over the entire SNR range for the TL position, followed by TM performing half as well as TL on average. Similar simulations were performed with varying conductivities for the lungs instead of the heart, which lead to comparable results.

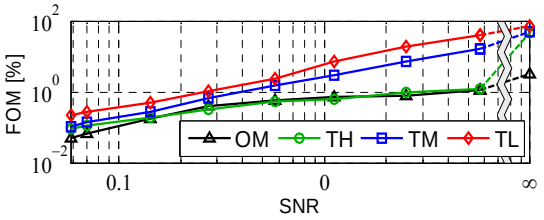

Figure 1: Double logarithmic plot showing the performance (FOM) of four belt positions (OM, TH, TM and TL) to detect the descending aorta with decreasing influence of the heart (SNR).

4 Conclusions and Outlook

These results suggest that a transversal low placement (TL) of the EIT belt is best to detect pulsatility signals from the descending aorta. However, the model is limited by the static nature of the lung and heart structures.

Future simulations with the lungs and heart as dynamic structures and comparisons with real measurements are suggested to validate the current results.

References

[1] Adler A, et al. *Physiol Meas* **33**:679-694, 2012
[2] Solà J, et al. *Med Biol Eng Comput* **49**:409-415, 2011
[3] Maisch S, et al. *Critical Care Medicine* **39**:2173-2176, 2011
[4] Proença M, et al. In *BIOSIGNALS*. 2014 (in press)
[5] Vonk Noordegraaf A, et al. *Physiol Meas* **17**:179-188, 1996
[6] Adler A, et al. *Physiol Meas* **30**:35-55, 2009

Influence of heart motion on EIT-based stroke volume estimation

Martin Proença[1], Fabian Braun[1,5], Michael Rapin[1], Josep Solà[1], Andy Adler[2], Bartłomiej Grychtol[3], Martin Bührer[4], Peter Krammer[5], Stephan H. Bohm[5], Mathieu Lemay[1], Jean-Philippe Thiran[6,7]

[1]Systems Division, Swiss Center for Electronics and Microtechnology (CSEM), Neuchâtel, Switzerland, map@csem.ch
[2]Systems and Computer Engineering, Carleton University, Ottawa, Canada
[3]Division of Medical Physics in Radiology, German Cancer Research Center (DKFZ), Heidelberg, Germany
[4]Institute for Biomedical Engineering, University and ETH Zurich, Zurich, Switzerland
[5]Swisstom AG, Landquart, Switzerland
[6]Signal Processing Laboratory (LTS5), Swiss Federal Institute of Technology (EPFL), Lausanne, Switzerland
[7]Department of Radiology, University Hospital Center (CHUV) and University of Lausanne (UNIL), Lausanne, Switzerland

Abstract: Cardiac electrical impedance tomography (EIT) signals are affected by myocardial motion. The feasibility of stroke volume estimation using such signals is thus questionable. Results based on a dynamic model show that myocardial motion indeed affects but does not compromise stroke volume estimation.

1 Introduction

In EIT, cardio-synchronous impedance changes in the heart region are assumed to reflect variations of blood volume originating mainly from the ventricles [1]. EIT appears therefore as an interesting continuous and non-invasive modality for monitoring total ventricular volume (TVV), and thus estimating total stroke volume (TSV), defined as the maximal change in TVV over a full cardiac cycle. However, there is increasing evidence that other factors – unrelated to blood volume changes – are contributing to these variations of cardiac-related impedance [2]. In that context, simulations we performed on a finite element 2D extruded dynamic bio-impedance model showed that EIT signals in the heart region might be dominated by myocardial motion-induced changes [3].

These findings raised the question whether heart signals – affected by myocardial motion – remain valid for estimating changes in TVV and thus TSV. The hypothesis that the total impedance change in the heart area remains a true indicator for TVV and TSV is thus investigated here.

2 Methods

To test this hypothesis, we exploited the above 2D dynamic bio-impedance model – created from segmented magnetic resonance (MR) data imaged in the heart horizontal long axis plane – and considered three scenarios: In *Scenario A,* we reproduced cardiac blood volume-related impedance changes by simulating the filling and emptying of the cardiac cavities. In *Scenario B,* myocardial motion-induced changes were reproduced by simulating the dynamics of the heart muscle. Finally, *Scenario C* is the real-case scenario and simulates both blood volume-related and motion-induced changes [3].

These simulations were performed on our finite element model over a full cardiac cycle (corresponding to 20 simulated EIT frames) using the open source EIDORS toolbox, with image reconstruction carried out by the GREIT approach [4]. For each scenario, the impedance change ΔZ – with respect to end-diastole in the heart area – was computed for all frames, thus providing an EIT-based indicator for TVV, according to our hypothesis. Hereafter referred to as TVV_{EIT}, it was expected to perform best with *Scenario A* (no heart motion) and worse with *Scenario B* (heart motion only).

The reference TVV_{REF} was obtained by summing the volumes V_{LV} and V_{RV} of the left and right ventricles. V_{LV} and V_{RV} were computed via the area-length method [5] – with the areas (Σ_{LV} and Σ_{RV}) and lengths (L_{LV} and L_{RV}) coming from the MR data used to create our model:

$$TVV_{REF} = c_{LV} \cdot \Sigma_{LV}^2 / L_{LV} + c_{RV} \cdot \Sigma_{RV}^2 / L_{RV} \text{ (ml)}, \quad (1)$$

where $c_{LV} = 8/(3\pi)$ [5] and $c_{RV} = 2/3$ [6]. L_{RV} was measured in the vertical long axis plane [6]. The total end-diastolic volume $TEDV_{REF}$ and the total stroke volume TSV_{REF} inferred from TVV_{REF} (see Figure 1) were used to compute TVV_{EIT} by translating ΔZ – normalized by its maximal (systolic) value – into millilitres:

$$TVV_{EIT} = TEDV_{REF} - TSV_{REF} \cdot \Delta Z_{NORM} \text{ (ml)}. \quad (2)$$

3 Results

The estimation error (mean±SD) between TVV_{REF} and TVV_{EIT} was of 1.9±13.3, –14.1±19.5 and –10.1±15.7 ml for *Scenario A, B* and *C*, respectively.

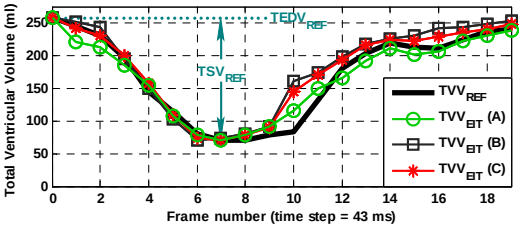

Figure 1: Total ventricular volume estimation using simulated EIT cardiac signals originating from blood volume-related impedance changes (*A*), motion-induced changes (*B*), or both (*C*).

4 Conclusions

In agreement with our expectations, simulations showed that myocardial motion increased the error on TVV_{EIT} and thus EIT-based TSV estimation, without however compromising the approach. When both blood volume changes and myocardial motion are in action (*Scenario C*, real-case scenario) an EIT-based TVV estimation error of –10.1±15.7 ml was obtained, which is sufficiently low to be clinically useful in normal subjects [5].

References

[1] Eyüboglu B, et al. *IEEE EMBM* **8**:39-45, 1989
[2] Hellige G, Hahn G. *Critical Care* **15**:430, 2011
[3] Proença M, et al. In *BIOSIGNALS*. 2014 (in press)
[4] Adler A, et al. *Phys Meas* **30**:S35, 2009
[5] Underwood SR, et al. *Br Heart J* **60**:188-195, 1988
[6] Levine RA, et al. *Circulation* **69**:497-505, 1984

Lung tissue measured in EIT may change depending on the positioning of electrode plane

Zhanqi Zhao, Sabine Krüger-Ziolek, Benjamin Schullcke and Knut Möller

Furtwangen University, VS-Schwenningen, Germany; zhanqi.zhao@hs-furtwangen.de

Abstract: EIT measurements were performed in 3 different transverse thoracic planes during pulmonary function test. Ratios between relative impedance changes and volume changes were different depending on the positioning of electrode planes. Since atelectasis should be minima in the healthy volunteers, the change of ratios may be explained by activity of respiratory muscles, which lead to changes in amount of lung tissue captured by EIT.

1 Introduction

Multiple EIT measurements in different transverse thoracic planes indicate that relative impedance change (ΔI) to volume change (ΔV) ratio may differ at different ventilation levels [1-2]. Since these studies were performed in animals or patients under mechanical ventilation, researchers suspected that the differences of the ratio in various electrode planes were due to different recruitment rates in these thoracic planes or capturing other organs. We conducted a prospective study in healthy volunteers with spontaneous breathing. We hypothesized that due to the movement of respiratory muscles (mainly diaphragm), the amount of lung tissue captured in certain EIT electrode planes may change, causing the change of ratio between ΔI and ΔV at different ventilation levels.

2 Methods

Pulmonary function test was performed in 3 healthy males with body plethysmography (Ganshorn, Germany). Each of the volunteers was asked to perform normal tidal breathing for about 2 minutes before deep exhalation aiming the residual volume and then deep inhalation to total lung capacity. This procedure was repeated 3 times, during which EIT measurements were performed at 3 different transverse thoracic levels (Pulmovista 500, Dräger, Germany). The EIT electrode belt was placed at (1) about 3rd or 4th intercostal space, (2) at about 5th or 6th intercostals space, (3) at about 7th intercostals space. The instruments were special manufactured so that body plethysmography and EIT can be applied at the same time. Functional residual capacity (FRC) was measured to confirm that the volunteers had similar ventilation level in each measurement prior to the vital capacity manoeuvre. Tidal volume (V_T), ins- and expiratory reserve volume (IRV, ERV) were measured. Corresponding relative impedance change ΔI_{VT}, ΔI_{IRV}, and ΔI_{ERV} were calculated, as well as the ratio between those ΔI and volumes.

3 Results

Figure 1 exemplarily shows 3 relative impedance curves of 1 volunteer in 3 transverse thoracic planes. Although the end-expiratory lung impedance values were different because of individual reference baselines, in fact, in all 3 measurements of each volunteer, FRC levels were similar (mean coefficient of variation 0.04). ΔI_{ERV}/ERV at cranial level were slightly higher than ΔI_{IRV}/IRV, while that were totally the opposite at caudal level (Fig. 2).

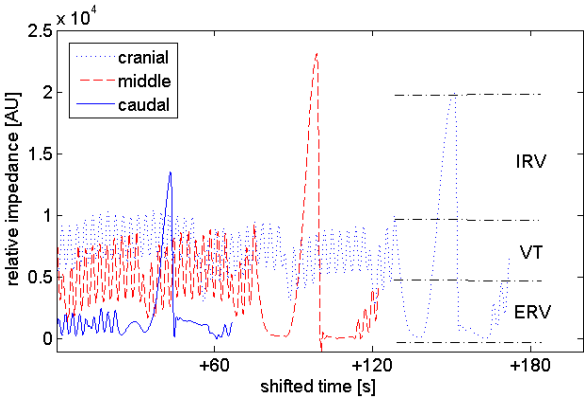

Figure 1: Relative impedance curves of 1 volunteer at 3 different thoracic levels.

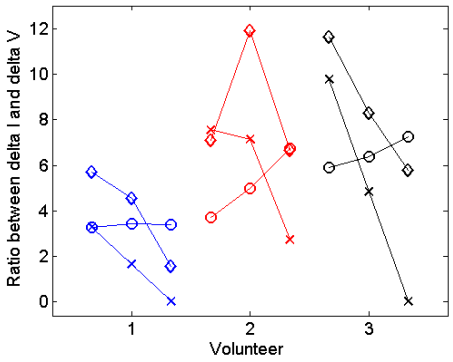

Figure 2: Ratios between various ΔI and volumes in three volunteers. Circle, diamond, and x-mark represented EIT measurements at cranial, middle and caudal thoracic levels, respectively. Within one measurement, three ratios from left to right were ΔI_{IRV}/IRV, ΔI_{VT}/VT and ΔI_{ERV}/ERV, respectively.

4 Discussion and conclusions

We found in the present study that ratios between ΔI and ΔV were different during total lung capacity maneuver depending on the positioning of electrode planes. Since atelectasis should be negligible in the healthy volunteers, the change of ratios may be explained by the activity of respiratory muscles, influencing the amount of lung tissue captured in certain EIT planes. In extreme case, totally different lung tissue is captured in EIT at different ventilation levels, if the electrode positioning is not ideal, so that the EIT images may be misinterpreted.

References

[1] Bikker IG, et al. Crit Care 15:R193, 2011

[2] Frerichs I, et al. IEEE Trans Med Imaging 18: 764-73, 1999

Regional lung compliance: Coupling ventilation and electrical data

Henry Tregidgo[1], Michael Crabb[2], William Lionheart[3]

[1]University of Manchester, Manchester, UK, henry.tregidgo@postgrad.manchester.ac.uk
[2]michael.crabb@postgrad.manchester.ac.uk
[3]bill.lionheart@manchester.ac.uk

Abstract: Before it is possible to use EIT for respiratory monitoring of critical care patients, regional conductivity must be converted to useful diagnostic parameters. This work proposes a road map for dynamically retrieving quantities, such as lung compliance, from data available at the bedside. Combining electrical and ventilator data with other imaging modalities such as MRI or CT where available.

1 Introduction

In a clinical setting it is difficult to interpret the physical meaning of conductivity reconstructions. For EIT to become a useful diagnostic tool we need to have a model in place for converting a conductivity image into more clinically relevant parameters.

Models of the lungs generally focus on a static relationship between air volume and pressure, leading to parameters such as compliance. Hence an obvious approach would be to estimate the air volume fraction from local conductivity. Due to the high temporal resolution EIT provides, an ODE model could allow calculation of the other dynamic parameters such as airflow resistance, and even model the effects of high frequency oscillatory ventilation.

This work sets some research directions for improved retrieval of useful clinical parameters and anticipated challenges in their completion.

2 Research Directions

We believe that the essential steps required to retrieve useful information from EIT must include:

1. Segmenting regions in the chest cavity and assigning specific micro-structures to these sections of the reconstruction,
2. Determining the air volume fraction change from the change in conductivity,
3. Calculating regional air volume from air volume fractions,
4. Using an ODE model to calculate the required diagnostic parameters.

2.1 Chest Segmentation

Defining likely contents of specific anatomic regions in advance has several uses. These include refining models for retrieving air volume fractions as well as labelling functional units of the lung for which diagnostic parameters will be required.

MRI and CT data can be used to segment specific regions of the chest cavity and assign properties to them based on anticipated microstructure. It would then be necessary to model how this structure changes during the breathing cycle. This modelling will require coupling of neighbouring regions through mass and volume conservation, as well as comparisons with typical deformations of the lung, chest cavity and abdomen under forced ventilation.

2.2 Air Volume Fractions

We would like to create a homogenisation scheme, mapping an underlying microstructure to bulk conductivity. We will then need to invert this to find the air volume fraction of a region from reconstructed conductivity values. The assumed microstructure can be as simple as spherical inclusions dispersed in a homogeneous substrate [1], or can further reflect the anisotropic structures identified while segmenting the lung image [2].

However, air content is not the only quantity which will affect the bulk conductivity. In addition other features such as blood flow or lung fluid content may need to be incorporated. This could be done by combining heart rate and blood pressure measurements with dispersion relations from multi-frequency EIT to discern blood content.

2.3 Regional Air Volume

As previously noted, at different times throughout the breathing cycle the domain will have deformed, changing the physical volume occupied by the lung. The volume change is non-uniform, complicating the conversion of air volume fractions to regional volumes. Models created for chest segmentation could help with this problem while the ventilator itself provides information on the amount of air passed into the lung, which can be used to constrain the total air volume within the lung.

2.4 ODE Coupling

We can model each functional unit of the lung as a simple physical system with parameters such as compliance and resistance. Different functional units of the lung can be coupled through their physical locations. We can use the calculated air volume fractions as states of a time series differential equation, and set up a series of coupled second order ODEs relating the air volume, flow and pressure states of the system [3]. Using the airway opening measurements as constraints, we can use techniques from inverse problems for ODEs to estimate the clinically meaningful parameters.

References

[1] Vanbeek L. *Physica* **26**(1):66–68, 1960
[2] Kanaun SK, Kochecksaraii SB. *International Journal of Engineering Science* **46**(2):147–163, 2008
[3] Ben-Tal A, Smith JC. *Respiratory Physiology & Neurobiology* **170**(1):103 – 112, 2010

Influence of different thorax models on anatomical precision of EIT

Peter Salz[1], Andreas Reske[2], Hermann Wrigge[2], Gerik Scheuermann[3], Hans Hagen[1]

[1]Computer Graphics & HCI Group, University of Kaiserslautern, Germany, salz@rhrk.uni-kl.de
[2]Clinic and Policlinic for Anesthesiology and Intensive Care Medicine, University Hospital Leipzig, Germany
[3]Institute for Computer Science, University of Leipzig, Germany

Abstract: To study the anatomical precision of EIT images, we compared 2D, 2.5D and 3D thorax models of varying complexity for EIT data of a healthy and an injured lung. We determined the lung shape as the averaged tidal image for several breaths. The overlap was computed for a reference CT shape. A 3D subvolume of the lung with large anatomical complexity achieves the best overlap scores for most cases.

1 Introduction

It is a general understanding in the EIT community that patient-specific models are necessary to reduce artifacts, noise and anatomical uncertainty in EIT images, especially concerning the lung and heart shape. With this study we aim to quantitatively compare a large variety of body models in terms of overlap of lung and heart shapes in EIT images with the respective shapes in reference CT data. We formulated several research questions. What is a better reference: a CT slice, as used by Ferrario et al. [1], or a projection of the 3D lung shape into the electrode plane? How do models of different dimensionalities and anatomical complexities compare? Is there a difference in heart overlap precision for mechanical ventilation, apnoe, and saline bolus injection? We used CT and EIT data from one pig. CT data were recorded before and after the lung injury. EIT datasets include mechanical ventilation before and after the lung injury, a lowflow maneuver, and a phase of apnoe, followed by a saline bolus injection.

2 Methods

Each set of models was generated with different anatomical complexities, starting with the thorax shape, adding lung and heart shape, known pathological lung regions, and finally major blood vessels. 2D models were computed using *distmesh*, while EIDORS was used for the 2.5D models. 3D models were computed as described in [2]. Also, 3D models from only ten CT slices of the whole lung were generated, as well as a subset of the lung extending to 3 cm above and below the electrode plane.

After image reconstruction with GREIT, we separated the ventilation and perfusion signals using the method by Deibele et al. [3]. As anatomical reference both the CT slice closest to the electrode plane and a weighted projection of the whole thorax into this plane were used. Thorax shapes of EIT and CT images were registered to properly compare the overlap. To extract the shape of the lung function from the EIT images, we averaged the tidal images for each breath during a period of 40 seconds during each EIT recording. The fraction of EIT pixels overlapping with the CT shape was computed with the formula used by Ferrario et al. [1]. Similar to their approach, we thresholded and thereby reduced the size of the tidal image until an overlap of 50%, 75%, and 90% was achieved (compare Figure 1). We assume that the lower the threshold necessary to achieve a large overlap, the better the image quality and the anatomical precision of the body model. The heart shape was determined as the largest ventral cluster of pixels with strong signal changes over time in the perfusion signal.

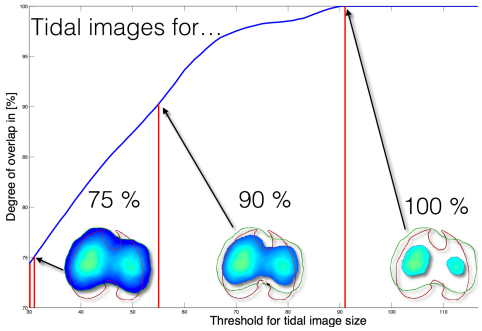

Figure 1: The tidal image thresholds to achieve 75%, 90%, and 100% lung overlap for the 3D subvolume model.

3 Results

The reference slice achieves much better lung overlap scores than the projection, but performs very poorly for the heart overlap due to the small heart shape in the slice (see Conclusion). Compared to the reference slice, 2.5D models achieve the best overlap, very closely followed by the 6 cm subvolume. For the reference projection, 2D models and the 6 cm subvolume perform best. Models of high complexity (using thorax, lung, heart and pathological lung shape) perform better than simple models. The heart overlap during apnoe is almost identical to the saline bolus dataset. During ventilation, the heart overlap is even slightly better than during bolus injection.

4 Conclusion

Our results indicate that the overlap formula is not very well-suited since only the fraction of EIT pixels inside the reference shape is considered. Thus, a small EIT shape that lies completely within the reference shape, but only covers a small part of this shape, achieves very high overlap scores. Vice versa, a large EIT shape gets very low overlap scores if the reference shape is very small (as is the heart shape in our CT reference slice). We will investigate a formula that also incorporates the fraction of the reference shape that is covered by the EIT shape.

References

[1] Ferrario D, Grychtol B, Adler A, et al. *IEEE Trans Biomed Engineering* **59**(11-1):3000–3008, 2012

[2] Salz P, Reske A, Wrigge H, et al. In *Short Paper Proceedings of the EuroVis workshop on Visualization in Medicine and Life Sciences (VMLS 2013)*, 49–53. Eurographics Digital Library, 2013

[3] Deibele JM, Luepschen H, Leonhardt S. *Physiological Measurement* **29**(6):S1, 2008

Fast D-bar reconstructions of ventilation and perfusion on a pairwise current injection system

Melody Dodd[1] and Jennifer L. Mueller[2]

[1]Colorado State University, Fort Collins, CO USA 80523, dodd@math.colostate.edu
[2]Colorado State University, Fort Collins, CO USA 80523, mueller@math.colostate.edu

Abstract: A fast implementation of the D-bar method for reconstructing conductivity changes on a 2-D chest-shaped domain is described. Cross-sectional difference images of ventilation and perfusion in a healthy human subject are presented. The images constitute the first D-bar images from EIT data on a human subject collected on a pairwise current injection system.

1 Introduction

D-bar methods are a class of direct (noniterative) reconstruction algorithms that make use of complex geometrical optics (CGO) solutions to PDEs known as D-bar, or $\bar{\partial}$, equations. D-bar equations are of the form $\bar{\partial}u = f$, where f may depend on u, and the $\bar{\partial}$ operator is defined by $\bar{\partial} = 0.5\,(\partial_x + i\partial_y)$. The common threads in these methods are (1) a direct relationship between the CGO solutions and the unknown conductivity, (2) a nonlinear Fourier transform, also known as the scattering transform, providing a link between the data and the CGO solution, and (3) a D-bar equation to be solved for the CGO solutions with respect to a complex-frequency variable.

These steps have been generally regarded as computationally intensive, but through parallelization and careful optimization of the computational routines, we present a fast implementation capable of providing real-time images from the pairwise current injection system at CSU.

2 Methods

The D-bar method used here is based on the uniqueness proof [1] and subsequent results and implementations [2, 3].

2.1 Fast implementation

The first step of the method is to compute a matrix approximation to the current-to-voltage map. This can be accomplished efficiently with inner products, as explained in [4].

The fast algorithm uses the approximation to the scattering transform known as $\mathbf{t}^{\exp}$, which linearizes the scattering transform, but not the entire method, by replacing the CGO solution ψ that depends on the unknown conductivity σ by another CGO solution independent of σ representing the asymptotic behaviour of ψ. Introducing the function $\mu(z,k) = e^{-ikz}\psi(z,k)$, the conductivity can be determined directly from μ by solving

$$\frac{\partial \mu(z,k)}{\partial \bar{k}} = \frac{\mathbf{t}^{\exp}(k)}{4\pi\bar{k}} e^{-i(zk+\bar{z}\bar{k})}\overline{\mu(z,k)},$$

and computing, for each z in the domain, $\sigma(z) = \mu^2(z,0)$. The computational solution of this equation comprises by far the bulk of the run time. The equation is formulated as an integral equation and solved using a fast implementation of the method in [5]. This equation was solved in a truncated region of the k-plane in parallel using optimized Matlab code and multiple processors.

2.2 Results

To demonstrate the D-bar method on data from this EIT system and to time the algorithm, we consider data sets collected using pairwise current excitation on 32 electrodes evenly spaced around the chest of a healthy male subject sitting upright and holding his breath. 360 frames of data were collected at 16 frames/s at 125 kHz and current amplitude 0.823 mA. Runtimes on a 12 core Mac Pro with two 2.66 GHz 6 core Intel Xeon processors and Matlab's parallel computing toolbox are listed in Table 1. Utilizing 7 cores in parallel results in a runtime of 0.0621 s/frame, which is less than the data acquisition time of 0.0625 s/frame.

Two difference images in the sequence of 360 frames are presented in Figure 1.

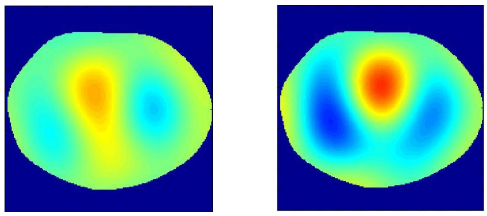

Figure 1: Changes due to perfusion in the chest of a healthy human subject. The heart is at the top, and red represents high conductivity and blue low conductivity. The images are displayed on the same scale.

Table 1: Runtimes on a 562 element grid with n cores in parallel

Number of cores	Total runtime (s)	s/frame
1	71.74	0.1998
2	49.02	0.1365
4	26.23	0.0731
7	19.27	0.0621
8	20.25	0.0647

3 Conclusions

The results presented here show for the first time the D-bar method applied to human chest data collected on a pairwise current injection system. Conductivity changes due to perfusion are clearly visible in the images. The fast implementation demonstrates the clinical potential of the D-bar algorithm as a reconstruction algorithm for real-time bedside imaging.

References

[1] Nachman AI, *Ann. of Math.*, 143:71–96, 1996.
[2] Siltanen S, Mueller JL, and Isaacson D, for the 2D inverse conductivity problem. *Inverse Problems*, 16:681–699, 2000.
[3] Murphy EK and Mueller JL, *IEEE Trans Med Im*, 28:1576–1584, 2009.
[4] Mueller JL and Siltanen S, *Linear and nonlinear inverse problems with practical applications*, SIAM, 2012.
[5] Knudsen K, Mueller JL, and Siltanen S, *J. Comp. Phys.*, 198:500-517, 2004.

Session 10

Reconstruction II

26 April 2014, 8:00 – 10:00

Solution of Inverse Problem by Infinite Boundary Elements and the Level Set Method

Tomasz Rymarczyk[1], Paweł Tchórzewski[1] and Jan Sikora[2]

[1]Net-Art, Lublin, Poland
[2]Electrotechnical Institute, Warsaw, Poland

Abstract: In this paper the inverse problem for the electric field is investigated. In order to solve the forward part of such problem we use the boundary element method coupled with infinite elements. The inverse problem is based on the gradient technique and the level set method. Such task can be considered as application of the electrical impedance tomography. Investigated structure is given in Fig. 1. We want to detect the closed curve localised on upper part of this plot.

1 Introduction

Boundary element method (BEM) is well known and effective numerical technique used to solve partial differential equations [3]. In literature we have a lot of extensions of BEM. For example a lot of effort has been put into combining BEM and finite element method. Another example is coupling BEM with infinite elements [1,2]. It gives us possibility to solve equations with boundaries described by open curves.

2 Theoretical Model

In the forward problem we start our considerations from following formula (proper for all boundary points) [3]:

$$\frac{1}{2}u(\vec{r}_i)+\sum_{j=1}^{N}\int_{\Gamma_j}u(\vec{r})\,q^*(\vec{r},\vec{r}_i)\,d\gamma_j=\sum_{j=1}^{N}\int_{\Gamma_j}q(\vec{r})\,u^*(\vec{r},\vec{r}_i)\,d\gamma_j. \quad (1)$$

Symbols u represents electrical potential, whereas q defines his normal derivative. The Green function and its normal derivative are denoted by u* and q* respectively. In equation (1) we have N finite boundary elements.
Next, we have introduced infinite boundary elements and the governing equation (2) has been derived. The derivation is quite long, and will be present in the full version of article. The governing integral equation is given by:

$$\begin{aligned}&\frac{1}{2}u(\vec{r}_i)+\sum_{j=2}^{N-1}u_j\int_{\xi=-1}^{\xi=+1}q^*(\vec{r}_j(\xi),\vec{r}_i)\,d\gamma_j+\\&+u_1\int_{\xi\to-\infty}^{\xi=+1}S_\infty(\xi)\,q^*(\vec{r}_1(\xi),\vec{r}_i)\,d\gamma_1+u_N\int_{\xi=-1}^{\xi\to+\infty}S_\infty(\xi)\,q^*(\vec{r}_N(\xi),\vec{r}_i)\,d\gamma_N\\&=\sum_{j=2}^{N-1}q_j\int_{\xi=-1}^{\xi=+1}u^*(\vec{r}_j(\xi),\vec{r}_i)\,d\gamma_j+\\&+q_1\int_{\xi\to-\infty}^{\xi=+1}S_\infty(\xi)\,u^*(\vec{r}_1(\xi),\vec{r}_i)\,d\gamma_1+q_N\int_{\xi=-1}^{\xi\to+\infty}S_\infty(\xi)\,u^*(\vec{r}_N(\xi),\vec{r}_i)\,d\gamma_N.\end{aligned} \quad (2)$$

Symbol S denotes the sum of the interpolation functions with exponential decay along infinite elements. One should notice that in our model there is only one open boundary curve. However generalisations of formula (2) can be easy done. In mathematical model we assume that in N – 2 nodes the normal derivatives q equal zero. Only in two nodes we set the electrical potential (see Fig. 1).

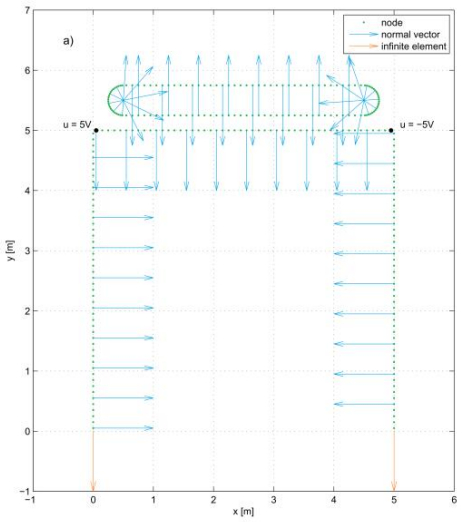

Figure 1: Geometrical model used in our calculations. Nodes, normal vectors and positions of infinite elements are indicated. The boundary of the domain is indicated by green dots.

Very important part of our research is the level set method. The equation of motion takes the form:

$$\frac{\partial\Phi}{\partial t}+\vec{V}\cdot\nabla\Phi=0, \quad (3)$$

where ϕ is the level set function. Function ϕ is transformed under influence of the velocity field $\vec{V}$. This field is given by the gradient technique [4].

3 Conclusions

Altogether during our studies three different geometrical models have been verified. It turns out that solving the forward problem through external approach is the best way in numerical analysis. Solutions of the inverse problem give us good results in all three cases.

References

[1] Beer G., Watson J.O.: *Infinite boundary elements*, International Journal for Numerical Methods in Engineering, 28 (1989), pp. 1233 - 1247.
[2] Beer G., Watson J.O., Swoboda G.: *Three-dimensional analysis of tunnels using infinite boundary elements*, Computers and Geotechnics 3, (1987), pp. 37 - 58.
[3] Kythe P.K.: *An introduction to Boundary Elements Methods*, CRC Press, (1995)
[4] Rymarczyk T., Sikora J., Waleska B.: *Coupled Boundary Element Method and Level Set Function for Solving Inverse Problem in EIT*, 7th World Congress on Industrial Process Tomography, WCIPT7, 2-5 September 2013, Kraków, Poland

Effective electrode positions and stimulation patterns for head EIT

Yasin Mamatjan[1,3], Bartłomiej Grychtol[2], Andy Adler[3]

[1]Zirve University, Gaziantep, Turkey
[2]German Cancer Research Center, Heidelberg, Germany
[3]Carleton University, Ottawa, Canada, mamatjan.yasin@zirve.edu.tr

Abstract: The objective of this study is to find an effective stimulation and measurement strategy to improve distinguishability for head EIT. To better understand the relationship between distinguishability and various strategies (stimulation/measurement patterns) for a set of electrodes, we evaluated a realistic head model and a range of common strategies.

1 Introduction

Electrical Impedance Tomography (EIT) of the head has the potential to image cerebral edema and stroke, and to assist the EEG inverse problem. To effectively utilize an EIT system for human head, there is a need for maximizing sensitivity and increasing detectability by choosing an appropriate stimulation pattern and electrode placement strategy. Fabrizi et al [1] conducted simulation study for brain imaging using a realistic finite element (FE) model of the head, but only a limited evaluation was carried out due to high computational cost, where only 14 protocols were tested for both homogeneous model and a realistic head model. The objective of this study is to find an effective strategy to use a given EIT system for head EIT by systematically assessing possible stimulation and measurement patterns.

2 Methods

This paper (i) implements a realistic head model with 73 electrodes in standard EEG positions, (ii) provides quantified values and demonstrates the specific relationship between distinguishability and target position for different stimulation / measurement strategies, and (iii) makes recommendations for 16, 32, 64 electrode systems using standard EEG caps. The results are analyzed using the distinguishability formulation proposed by [3].

A realistic FE mesh of an adult head with 73 electrodes in standard EEG positions was built based on the mesh SAH262 contributed to EIDORS by [2]. Using EIDORS's interfaces to Netgen and Gmsh, the scalp was re-meshed to include 73 circular electrodes with local mesh refinement [4]. After defining Nasion and Inion landmarks, the positions of the remaining 71 electrodes were calculated as an extension of the 10-20 standard.

We choose $N = 16$, 32 and 64 electrodes for simulations, numbering them front-to-back in a zig-zag fashion starting from the left-most electrode (Fp1). We denote the measurement strategy by Δs-m where the distance between the two stimulating electrodes is $s = 1,\ldots,N$ and that between measuring electrodes is $m = 1,\ldots,N$. Thus, the typical adjacent measurement and stimulation pattern is denoted by Δ1-1. For each total number of electrodes, we evaluate all strategies where $s = m$ for only 64 electrodes due to high computation time.

Distinguishability is defined as the ability to distinguish between a hypothesis H_1 (conductivity change) and the null hypothesis H_0 (no conductivity change) within a region of interest (ROI) according to measure m [3]. The maximum likelihood estimate [3] of the conductivity change $\arg\min ||\Delta\mathbf{d} - \mathbf{R}\Delta\sigma|| + P(\cdot)$ for the hypothesis m within an ROI of area A_R is $m = A_R\Delta\hat{\sigma}_R$. The probability that the null hypothesis is rejected is determined by the z-score [3]:

$$\bar{z} = \frac{\hat{m} - m_0}{\mathrm{std}(m)} = \frac{A_R\Delta\hat{\sigma}_R}{(\mathbf{R}_R\Sigma_n\mathbf{R}_R^\top)^{\frac{1}{2}}} = A_R\Delta\hat{\sigma}_R\sqrt{\mathbf{J}_R^\top\Sigma_n{}^{-1}\mathbf{J}_R} \quad (1)$$

where $\hat{m}$ is the maximum likelihood estimate for m, the null hypothesis is m_0 and $\mathrm{std}(m)$ is the standard deviation of m.

2.1 Results

Fig. 1 shows $\bar{z}$ distinguishability values for 16, 32 and 64 electrode systems and 8 different object positions from Nasion to Inion for the best and worst measurement strategies. Δ25-25 with 64 electrode model produced highest $\bar{z}$ values for different object positions, while the adjacent patterns Δ1-1 produced lowest $\bar{z}$ values for all 3 electrode configurations. For Δ1-1, 32 electrodes performed better than both 16 and even 64 electrodes.

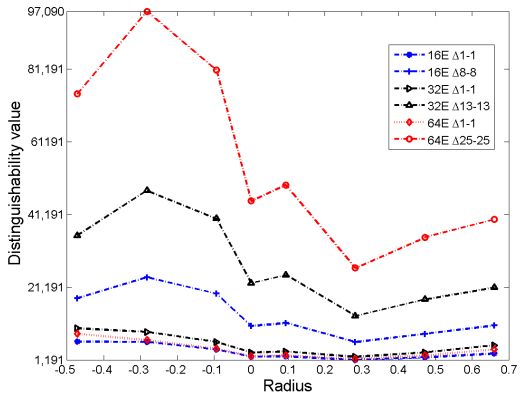

Figure 1: Distinguishability values for 16, 32 and 64 electrodes with 8 object positions for the stimulation and measurement patterns of Δ1-1 (adjacent) and Δs-m with maximum average $\bar{z}$ values.

3 Conclusions

Our results indicate that distinguishability increases throughout the model with average distance between the two stimulating/measuring electrodes. Future work will address the impact of changing electrode numbering and ways of finding optimum electrode positioning and measurement strategy to maximise distinguishability in a particular region of interest.

References

[1] Fabrizi L, McEwan A, et al. *Physiol Meas* 30 85–101, 2009
[2] Tizzard A and Bayford RH. *Physiol Meas* 28 163–182, 2007
[3] Adler A, Gaggero P, Maimaitijiang Y. *Physiol Meas* 32 731, 2011
[4] Grychtol B and Adler A. In *Proc IEEE EMBC 2013* 6429–32, 2013

Reconstruction of Conductivity Changes Using an Advanced Compensation Method in Electrical Impedance Tomography

Yang Pu and Tao Dai

Sealand Technology (Chengdu), Ltd., Chengdu, China. ypu@eitchina.net

Abstract: Element displacement and contact impedance changes are compensated in the reconstruction approach. Images have been reconstructed using the proposed method with the data from numerical simulation, saline phantom and *in vivo* human measurement.

1 Introduction

One of the key difficulties of Electrical impedance tomography (EIT) imaging is the modelling error, such as shape deformation and contact impedance changes. When a deformable medium is investigated, not only boundary elements (including electrodes) but also internal elements displace. Moreover, when the voltages are measured on the electrodes, the contact impedance that exists in the interface causes a voltage drop. If difference imaging techniques are involved, these difficulties can be partly solved [1-3], but in order to obtain a better imaging quality, element displacement and contact impedance changes have to be taken into account.

2 Methods

An augmented Jacobian $\mathbf{J} = [\mathbf{J_c}\ \mathbf{J_d}\ \mathbf{J_t}]$ is obtained by concatenating conductivity change Jacobian $\mathbf{J_c}$, element displacement Jacobian $\mathbf{J_d}$ and contact impedance changes Jacobian $\mathbf{J_t}$. A modified NOSER prior $[\mathbf{R}]_{i,i} = [\mathbf{J'}^T\ \mathbf{J'}]_{i,i}^p$ is established, where $\mathbf{J'} = [\mathbf{J_c}\ \mu^2\mathbf{J_d}\ \tau^2\mathbf{J_t}]$, we define μ and τ as the model hyperparameters to represent the different weights. The one-step linear Gauss-Newton (GN) method is implemented to solve the inverse problem.

2.1 Numerical Simulation

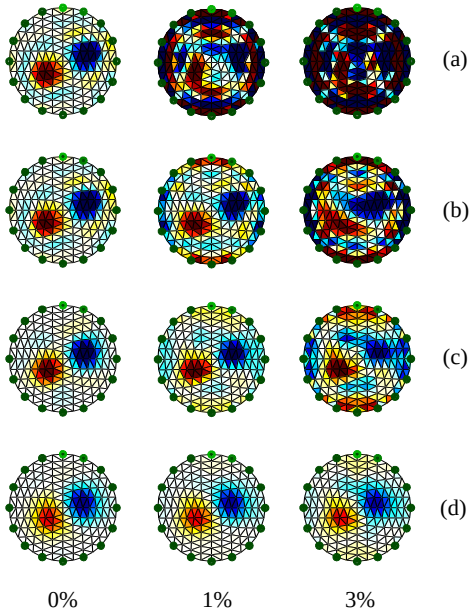

Figure 1: Image reconstructions. (a) Standard GN method; (b) Electrode movement model; (c) Proposed method with $\mu = 1$ and $\tau = 1$; (d) Proposed method with $\mu = \sqrt{0.1}$ and $\tau = 0.1$. From left to right, distortion amplitude increases from 0%, 1% to 3% of model diameter respectively.

2.2 Saline Phantom Measurement

The saline phantom is a plastic cylindrical tank with 14cm diameter and 12cm height, being filled with 0.9% saline solution. A small non-conductive spherical object of 1cm diameter was statically suspended. The proposed method successfully obtained the inhomogeneous target without introducing any artefacts.

2.3 *In vivo* Human Measurement

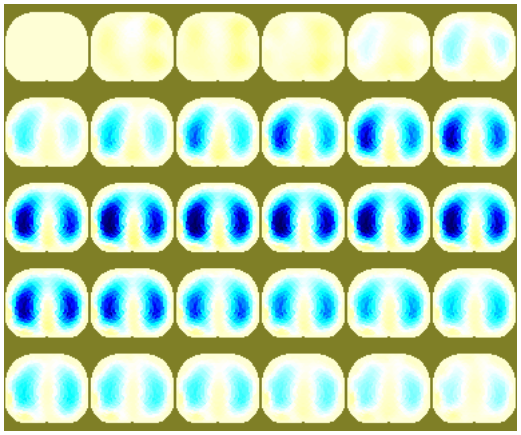

Figure 2: Images of lung ventilation. The breathing cycle from end inspiration to end expiration was approximately 5 seconds. Each second was shown in the same row.

3 Conclusions

An advanced compensation method which is more robust to shape distortion is proposed in this paper by an improved version of the electrode movement model [1]. The algorithm performed well and showed significant improvements of artefact resistance. One key advantage is that, once pre-calculations are completed, images can be reconstructed by a single regularized inverse, and it requires little additional time over traditional methods. Considering the reconstructed images from *in vivo* human measurement, this method shows potential to be applied in real time monitoring of lung ventilation and may be useful to increase the accuracy and reliability of EIT technique in routine clinical applications.

References

[1] M. Soleimani, *Physiol. Meas.* 27 S103-S13, 2006
[2] T. Dai, *Physiol. Meas.* 29 S77-S88, 2008
[3] A. Adler, *Physiol. Meas*. 32 823−834, 2011

Advances in EIT reconstruction through Simulated Annealing

Thiago C. Martins[1] and Marcos Sales Guerra Tsuzuki[1]

[1]Escola Politécnica, University of São Paulo, São Paulo, Brazil

Abstract: EIT reconstruction can be solved as an optimization problem through Simulated Annealing (SA), but often at a high computational cost. This paper presents new techniques of EIT reconstruction through SA, including partial evaluation of the objective function, alternate objective functions and multi-objective optimization. Reconstructions of experimental impedance data using the techniques exposed were successfully performed.

1 Introduction

EIT is a imaging technique for determining the electrical conductivity distribution inside an object from boundary measurements. A set of electrodes is attached to the object surface, electrical current is injected through these electrodes and electrical potentials are measured. This work is focused on the reconstruction of static conductivity images.

EIT image reconstruction can be performed by a Finite Element Model (FEM) parameter estimation and a maximum likelihood formulation. The resulting optimization problem may be solved using SA. It is a probabilistic optimization meta-heuristic of local exploration that requires only the variation of the objective function between two consecutive solutions [1]. As a drawback, it requires the evaluation of many solutions, thus making it problematic for objective problems with computationally expansive objective functions such as EIT.

2 SA Applied to EIT

This work presents some advances when SA is used to reconstruct conductivity distribution in EIT.

2.1 Partial Evaluation of the Objective Function

One objective function is the Euclidean distance between the measured electric potentials and the calculated potentials for all the applied current patterns for a given conductivity distribution. To reduce the reconstruction computational cost a *partial* evaluations of the objective function can be performed that is, at each SA iteration, an estimate $\tilde{E}$ and upper and lower boundaries E_{max} and E_{min} are obtained [2]. It can be shown that whenever the variation of those estimates $\Delta\tilde{E}$, ΔE_{max}, ΔE_{min}. satisfy

$$P_{err} \geq \min(e^{-\Delta\tilde{E}/kt}, 1) - \min(e^{-\Delta E_{max}/kt}, 1) \quad (1)$$

$$P_{err} \geq \min(e^{-\Delta E_{min}/kt}, 1) - \min(e^{-\Delta\tilde{E}/kt}, 1) \quad (2)$$

then the probability of SA at that iteration deviating of an SA with full objective function evaluation is less than P_{err}.

Those estimates may be determined by iteratively solving the FEM linear systems while obtaining an upper limit on the norm of the error at each iteration using a technique described in [3]. This error norm is pertinent to *all* equations of the FEM linear systems, while only the uncertainty on the electrode nodes really contribute to the uncertainty of the objective function. This leads to an overestimation of the required CG iterations to satisfy (1,2). This overestimation gets worse for denser FEM meshes.

2.2 Least squares error as an objective function

By taking the FEM linear systems of the simulated domain and imposing that the measured potentials are identical to the simulated ones, one obtains an overdetermined linear system whose total least squares error can be used as an objective function in EIT image reconstruction. This new objective function is quite suitable for the partial evaluation described in sec. 2.1, as a variation of the Lanczos Algorithm can be used to obtain increasingly better boundaries for its upper and lower values[4].

2.3 Multi-Objective

Regularization of inverse problems posed as optimization processes often appears as new terms in the objective function. The determination of the appropriate weight for those terms is difficult problem on itself.

An alternate approach is to consider both the original objective function and the regularization terms as concurrent objective functions to be minimized. This optimization category is called "multi-objective optimization". Multi-objective optimization problems do not admit a single solution, having instead a set of mutually non-dominating solutions.

3 Experimental Results

Experimental phantoms (Fig. 1a) were constructed with cucumeber slices. Impedance images were reconstructed using the methods proposed in sections 2.1 (Fig. 1b) 2.2 (Fig. 1c) and 2.3.

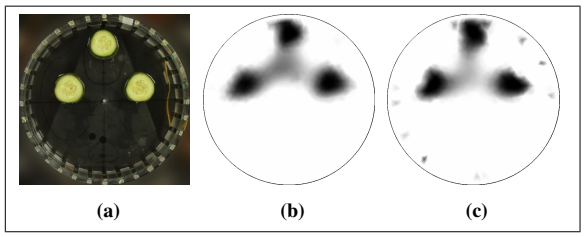

Figure 1: Experimental phantom and its reconstructions.

4 Conclusion

EIT images can be reconstructed using SA. The high computational cost of Simulated Annealing can be mitigated by the adoption of *partial* evaluation of the objective function. An alternative objective function, based on total least squares errors of overdetermined FEM linear systems, provide superior scalabiltiy with mesh density. Regularization with *a posteriori* weights can be obtained through multi-objective SA.

References

[1] Kirkpatrick S, Gellat CD, Vecchi MP. *Science* **220**:671–680, 1983

[2] Martins TC, Camargo EDLB, Lima RG, et al. *IEEE T Biomed Eng* (59):1867–1870, 2012

[3] Meurant G. *Numer Algorithms* **40**:157–169, 2005

[4] Golub GH, Meurant G. *Matrices, Moments and Quadrature with Applications*. Princeton University Press, 2010

MR-EPT Reconstruction Using an Inverse Formulation

Andrea Borsic[1], Irina Perreard[1, 2], and Ryan J. Halter[1]

[1]Thayer School of Engineering, Dartmouth College, Hanover, NH, USA

[2]Radiology Department, Geisel School of Medicine at Dartmouth College, Hanover, NH, USA

Abstract: The electrical conductivity of soft tissues can be reconstructed from imaging with MR Electrical Properties Tomography (MR-EPT). The reconstruction method used here is based on an inverse problem formulation, with two advantages over a direct inversion approach: a) no spatial differentiation is needed and b) the regularization term determines the resolution of the reconstructed data. The process is exemplified using phantom (gelatine and saline) data.

1 Introduction

Magnetic Resonance Electrical Property Tomography (MR-EPT) is a relatively new strategy for estimating a tissue's electrical conductivty and permittivity distribution. It offers the potential of high resolution admittance mapping as compared to electrical impedance tomography (EIT) without the need for electrodes as are needed for magnetic resonance EIT (MR-EIT). The general approach for conductivty imaging with MR-EPT is to obtain a phase image and/or B1 map image of the RF field produced using specific pulse sequences. This image can be manipulated to estimate the conductivity distribution. Typically, this manipulation requires second derivatives be computed from the phase data. This is an undesirable process that is prone to amplify noise. Other approaches have included algorithms that lower this requirement to first derivatives, reducing sensitivity to noise. Here we describe an alternative method that solves the MR-EPT problem using an inverse problem formulation that does not require differentiating the input image.

2 Methods

2.1 Inverse approach formulation

In MR-EPT, the electrical conductivity σ can be shown to be proportional to the Laplacian of the phase of the transmit B1 field:

$$\sigma(r) \approx \frac{1}{\omega\mu}\Delta\phi\left(H^{+}(r)\right). \quad (1)$$

The inverse is true as well: if $\sigma(r)$ is known, the phase can be obtained by solving $\Delta\phi = \omega\mu\sigma(r)$. Using an iterative inverse formulation approach, the updated value of σ is given by $\sigma_{new} = \sigma + \delta\sigma$ where

$$\delta\sigma = (J^T J + \alpha L^T L)^{-1}\left(J^T\left(\phi\left(H^{+}(r)\right) - \phi + \alpha L^T L\sigma\right)\right). \quad (2)$$

Here J is the Jacobian of the conductivity to phase mapping, L is a regularization matrix, and α is a regularization parameter used to stabilize the inversion. We have implemented this inversion using two different regularization terms: a) a quadratic/Laplacian approach and b) a Total Variation functional approach [1,2]. A Primal Dual Interior Point Method optimization scheme is used for the Total Variation approach, which produces images with sharper contrasts at boundaries.

2.2 Data acquisition

A custom gelatin phantom (10% gelatin, 1% NaCl) was constructed with three rows of circular wells with increasing diameters (5, 10, 15mm). Each series of wells was filled with saline solutions with increasing conductivities (~3, 5, 8 S/m). Cupric sulphate was added for MR contrast (Figure 1). Data was acquired on a Philips Achieva 3T platform, with a standard 3D SE sequence; phase images were used for reconstructing the conductivity. Two-dimensional reconstructions of the electric conductivity based on our inverse approach are presented in Figure 2.

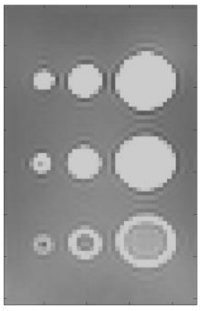

Figure 1: Phantom geometry (MR magnitude).

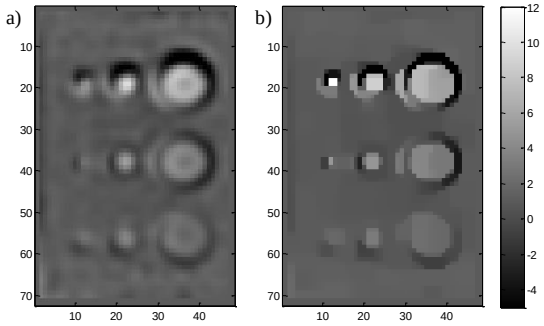

Figure 2: MR-EPT reconstruction with the inverse formulation approach: a) with quadratic regularization; b) with Total Variation regularization.

Conclusions

Reconstruction of MR-EPT conductivity data based on an inverse formulation approach is demonstrated here. The primary advantage of this approach is that is does not require differentiation of the phase data. An additional advantage is that custom regularization approaches can be considered for enahncing image quality. For instance, a priori anatomical information obtained from other MR variants (i.e. T2-weigted imaging) might be used as spatial priors.

References

[1] Borsic A, Graham BM, Adler A, Lionheart WRB, *IEEE Transactions on Medical Imaging*, 29, 1, 44-54, 2010.

[2] Borsic A, Adler A, *Inverse Problems*, 28, 095011, 2012.

Inequality Constrained EIT Modelling and Inversion

Nick Polydorides[1], Taweechai Ouypornkochagorn[1], Hugh McCann[1]

[1]University of Edinburgh, Edinburgh, UK. N.Polydorides@ed.ac.uk

Abstract: We consider modelling and imaging in EIT under some a priori inequality constraints on conductivity. Instead of constrained optimisation, we reformulate the model equations with respect to some monotone functions that encompass these constraints. We address the cases of positivity and boundness, posing the inverse problem using regularised nonlinear least squares. The results demonstrate significant spatial resolution improvements.

1 Introduction

The motivation for this work is to introduce a robust and simple to implement computational scheme appropriate for the cases where inequality constraints on the electrical conductivity are available a priori. Although several constrained optimisation algorithms are readily available [1] the methods presented here are appealing for their implementation simplicity. In the medical EIT setting, this type of prior information is likely attained through the literature on the targeted physiological phenomenon [2].

2 Methods

The scalar conductivity function $\sigma : B \to \Re$, is related to a finite set of real valued observations $\zeta \in \Re^m$ through the model

$$\zeta = M(\sigma) + n, \tag{1}$$

where $M : \sigma \mapsto \zeta$ is the nonlinear forward EIT mapping and n is some additive noise corrupting the data. Suppose further that σ is a priori known to belong within a subspace S. To enforce this assumption we introduce the injective mapping $\nu : \Re(B) \to S(B)$ from the space of real functions over the domain onto a subspace $S(B) \subseteq \Re(B)$, such that

$$\sigma(\mathbf{x}) \doteq \nu[\gamma(\mathbf{x})], \tag{2}$$

and conversely $\gamma(\mathbf{x}) = \nu^{-1}[\sigma(\mathbf{x})]$, where $\nu^{-1} : \sigma \mapsto \gamma$ always exists and it is continuous. Based on this one may formulate another forward model $F : \gamma \mapsto \zeta$, such as

$$\zeta = F(\gamma) + n, \quad \text{where} \quad F(\gamma) = (M \circ \nu)(\gamma). \tag{3}$$

2.1 Positivity

To impose positivity prompts to consider the subspace $S \doteq \{\sigma(\mathbf{x}) \in B | 0 < \sigma \leq \infty\}$ where a suitable choice for ν is the exponential function scaled by a relaxation factor $\kappa \neq 0$

$$\nu[\gamma(\mathbf{x})] \doteq e^{\gamma(\mathbf{x})/\kappa}, \quad \mathbf{x} \in B, \tag{4}$$

Under this transformation notice that the perturbations in the original and surrogate unknown functions, from reference points σ_*, γ_* are related by

$$\delta\sigma \doteq e^{\gamma/\kappa}(e^{\delta\gamma/\kappa} - 1). \tag{5}$$

To linearise the model (3) at (σ_*, γ_*), we appeal to the chain differentiation rule,

$$\partial_\gamma F(\gamma_*)\,\delta\gamma = \partial_\gamma (M \circ \nu)(\gamma_*)\,\delta\gamma = \partial_\sigma M(\sigma_*)\,\sigma_*\kappa^{-1}\,\delta\gamma, \tag{6}$$

where $\partial_\sigma M(\sigma_*)$ is the Jacobian of M. In this way, the linear approximation of the inverse problem for γ becomes

$$\delta\zeta = \partial_\sigma M(\sigma_*)\,\sigma_*\kappa^{-1}\,\delta\gamma + n. \tag{7}$$

2.2 Boundness

As an extension of the above scheme we consider mapping the conductivity into the subspace $S \doteq \{\sigma(\mathbf{x}) \in B | 0 < p \leq \sigma \leq t < \infty\}$ for some a priori known bounds $p < t$, using the scaled logistic regression function

$$\nu[\gamma(\mathbf{x})] \doteq p + \frac{t-p}{1+e^{-\gamma(\mathbf{x})/\kappa}}. \tag{8}$$

In this instance the perturbations $\delta\sigma$ and $\delta\gamma$ from a fixed reference are related via

$$\delta\sigma = \nu(\gamma + \delta\gamma) - \nu(\gamma) = w(\gamma, \delta\gamma)\nu_1(-\gamma), \tag{9}$$

where $w(\gamma, \delta\gamma) \doteq \frac{(t-p)(1-e^{-\delta\gamma/\kappa})}{(1+e^{-(\gamma+\delta\gamma)/\kappa})}$, and $\nu_1(\gamma) \doteq \frac{1}{1+e^{-\gamma/\kappa}}$. Appealing to the chain differentiation now yields the linearised problem for $\delta\gamma$ as

$$\delta\zeta = \partial_\sigma M(\sigma_*)\,\big(\nu(\gamma_*) - p\big)\nu_1(-\gamma_*)\kappa^{-1}\,\delta\gamma + n. \tag{10}$$

3 Results

To test the performance of our scheme we formulate the inverse problems as least squares problems based on (1) and (3) respectively. We then apply the Gauss-Newton algorithm for a few iterations while we regularise the linear problems using smoothness imposing regularisation.

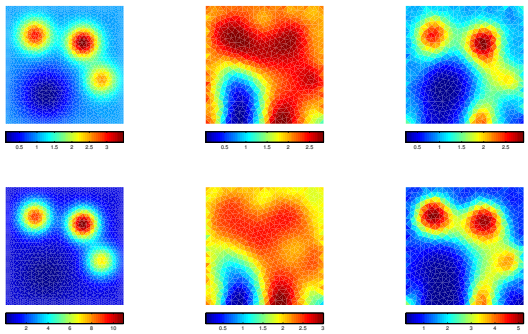

Figure 1: Top row, the target σ and the reconstructions using two Gauss-Newton iterations with smooth priors [2] on the original (middle) and positivity preserving model (right). Below, the corresponding images for a different target by implementing two iterations on the bound preserving model. Regularisation matrices and parameters are kept fixed to aid comparison of the results.

4 Conclusions

This work demonstrates how to obtain a constrained solution of the inverse problem in EIT using unconstrained optimisation. The proposed framework is computationally simple and can be used in conjunction with various inversion algorithms.

References

[1] D. P. Bertsekas, Constrained optimization and Lagrange multiplier methods, Athena Scientific, 1996.

[2] D. S. Holder (ed), Electrical Impedance Tomography: methods, history and applications, Institute of Physics, 2004.

EIT of the Human Body with Optimal Current Patterns and Skin-Electrode Impedance Compensation

Gregory Boverman[1], Tzu-Jen Kao[1], Jeffrey M. Ashe[1], Bruce C. Amm[1], David M. Davenport[1]

[1]GE Global Research Center, Niskayuna, NY (email: boverman@ge.com)

Abstract: Following the lead of the EIT research group at Rensselaer Polytechnic Institute, we have designed and implemented a system comprising 32 independent current sources, in which it is possible to apply current patterns optimizing distinguishability. One potential technical problem is that we are measuring voltages on current-carrying electrodes, giving some sensitivity to time varying skin-electrode impedances. We demonstrate here an algorithm to estimate simultaneously changes in the medium and time-varying skin-electrode impedances.

1 Introduction

Most of the electrical impedance tomography systems developed to date, with the notable exception of the group at Rensselaer Polytechnic Institute (RPI) [1, 2], have been based upon pairwise current patterns utilizing a single current source. These systems have the advantage of relative simplicity, but a significant disadvantage is that the current patterns utilized are not optimal with respect to maximizing distinguishability [3].

One technical issue involved in utilizing the optimal patterns and multiple-electrode excitation is that voltage changes are induced by time-varying skin-electrode impedances. We have developed algorithms, similiar to those described previously [4], but with significantly reduced computational complexity, to simultaneously estimate time-varying skin-electrode impedances and changes within the body.

2 Methods

2.1 Estimation and compensation of skin-electrode impedances

We assumed that electrode skin-electrode impedances could be modeled as being due to a discrete complex circuit element coupling the electrode to the body. Given this model, the Jacobian of voltage changes with respect to time-varying changes in the value of this discrete element could be computed explicitly for a given pattern set. We could then compute the skin-electrode impedance changes responsible for a set of voltage changes directly using least-squares methods.

2.2 Experimental protocol

Under institutional review board (IRB) supervision, we collected free respiration data from several human subjects measuring with 32 adhesive AgCl electrodes equally spaced in a single ring around the circumference of the chest. We utilized the GE-built GENESIS EIT system, currently an investigational prototype, and for each of the cases applied the optimal current patterns, as generated by a geometry-specific finite-element model and EIDORS [5].

3 Results

We computed the standard deviations of the changes in voltages vs. a reference data frame, in mV, for the optimal pattern set, with and without compensation for changes in skin-electrode impedances. We also synthesized the voltages that would have resulted from application of adjacent current patterns, measuring voltage differences between pairs of electrodes not carrying currents. We found that the preponderance of the voltage differences for the optimal patterns was due to changes in skin-electrode impedance, but that these changes could be estimated and compensated. The adjacent patterns were largely immune to skin-electrode impedance changes, but, for the same maximal current, smaller changes in voltage were induced, thus a larger SNR would be required for imaging. The results are summarized in Fig. 1.

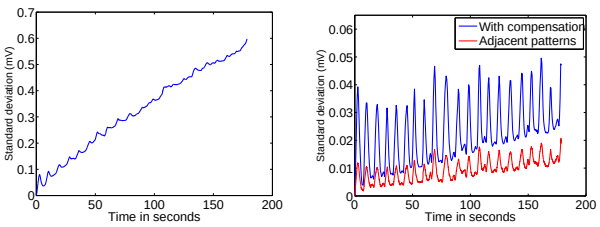

Figure 1: Standard deviations of difference in voltages of a given frame from a reference frame, in mV, for optimal patterns without compensation (a), with compensation, and adjacent current patterns (b).

4 Conclusions

In conclusion, it is possible to probe the body with "optimal" current patterns and to measure on current-carrying electrodes, but careful consideration needs to be taken of changes in skin-electrode impedances.

References

[1] Liu N, Saulnier GJ, Newell JC, et al. In *Proc. 6th Conf. on Biomedical Applications of Electrical Impedance Tomography, University College London, London, UK*. 2005

[2] Saulnier G, Liu N, Tamma CP, et al. In *Proc. IEEE EMBC*. 2007

[3] Isaacson D. *IEEE Trans Med Imag* **5**:92–95, 1986

[4] Boverman G, Isaacson D, Saulnier GJ, et al. *Biomedical Engineering, IEEE Transactions on* **56**(12):2762–2772, 2009

[5] Polydorides N, Lionheart WR. *Measurement Science and Technology* **13**(12):1871, 2002

Session 11

Applications III

26 April 2014, 10:45 – 12:00

Localized frequency difference EIT for lung tumour monitoring

Chuan Li Yang[1] Manuchehr Soleimani[1]

[1]Engineering Tomography Laboratory (ETL),
Department of electronic and electrical engineering, University of Bath, UK

Abstract: This paper presents a localized frequency difference EIT (fdEIT) algorithm for lung tumour monitoring. A simulated fdEIT is used to provide tomographic images of lung tumour by assuming local area of tumour is known. Limited region technique is applied to extract important information out of region of interest. Further experimental phantom based tests will be carried out to validate the proposed method.

1 Introduction

Electrical impedance tomography (EIT) is a fast and cost-effective technique to provide tomographic conductivity image of a subject from boundary current-voltage data. EIT has various potential applications in medical area, such function monitoring in lung EIT imaging. In traditional lung EIT imaging dynamical images of entire lung is generated to clinically investigate aspects of respiratory functions.

In this paper we present hypothesis of using lung EIT imaging for lung tumour monitoring. The lung tumour imaging using EIT is proposed during cancer treatment process such as radiation therapy. This poses some major challenges including: spatial resolution for lung tumour imaging is far more challenging than imaging entire lung itself; time difference imaging may not work as the reference image of the patient without lung tumour may not exist. Additionally imaging lung interior may become very challenging due to its low electrical conductivity, so a complex impedance imaging may be needed. Traditional EIT reconstruction uses time difference imaging technique. However, time difference EIT may not be useful for monitoring lung tumour behaviour as it is difficult to obtain background data of lung while the tumour has already consisted in the region. This problem may be solved by using frequency difference reconstruction [1] as it only requires measurement data in two different frequencies. This will work only if we can find two frequencies that the lung tumour has different electrical conductivity (or permittivity) compare to normal tissues. The difficulty is that lung itself has different frequency response compared to chest tissues [3]. In this case, both data from thorax and lung are treated as background data. When lung tumour is moving or changing, conductivity changes due to frequency change can produce conductivity image of lung tumour. EIT for lung tumour monitoring can take advantage of a priori information from diagnostic X-Ray CT images, so a localised EIT can be used to further enhance the spatial resolution.

2 Methods

In this paper, we use a frequency difference EIT (fdEIT) algorithm to produce lung tumour image. Using a weighted fdEIT algorithm [2] is essential to produce satisfying fdEIT images. Patients specify model can be developed using diagnostic CT images which can have the tumour position located. Limited region tomography (LRT) method is added for extracting the useful information out of the whole boundary. An FEM model of 16 electrodes EIT human chest model is created and image of lung is reconstructed (Figure 1). Figure 2 shows a simulation of lung tumour using a human lung mesh model. Reconstructions are done using adjacent current pattern. Background data includes thorax and two lungs with tumour in one single frequency, secondary data includes the same tumour but assuming with different frequency response. Reconstruction shows tumour images under fdEIT and LRT assumptions.

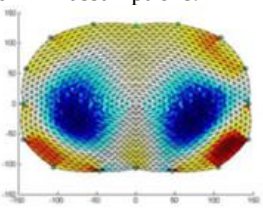

Figure 1: Reconstruction of simulated lung with 16 electrodes chest model.

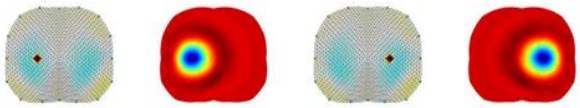

Figure 2: True images of lung tumour and simulation results of reconstructing tumour in a human lung structure.

The idea of localising the image is that assuming the tumour position can be obtained by CT scan, a specific region of interest (ROI) can be created by resizing the Jacobian matrix and resolving the inverse problem only on limited region.

3 Conclusions

This paper proposes a localized weighted frequency difference EIT technique for lung tumour imaging. Localize technique is employed for extracting useful information out of the region of interest. Phantom based experimental results will be presented in conference presentation. Although, this is an extremely challenging imaging tasks, but we hope that we will take advantage of recent momentum in conventional EIT lung imaging to make progress.

References

[1] J K Seo, J Lee, S W Kim, H Zribi, E J Woo, Physiol. Meas, 29, 929-944, 2008.
[2] S C Jun, J Kuen, J Lee, E J Woo, D Holder, J K Seo, Physiol. Meas, 30, 1087-1099, 2009.
[3] C Gabriel, S Gabriel, E Corthout, Phys. Med. Biol., 41, 2231-2249, 1996.

Assessment of EIT/CT Fusion Imaging using a Biological Phantom

Kalpagam Krishnan, Jeff Liu, Kirpal Kohli
BC Cancer Agency, Fraser Valley Centre, Surrey, Canada, kkohli@bccancer.bc.ca

Abstract: A cylindrical slice of seeded winter melon with an air-cavity was imaged using CT and EIT imaging systems. The structural regions were extracted from the CT image using morphological image processing algorithms and fused with the functional information of its EIT image. Fusion performance showed a detectability increase of 67% along with a structural similarity increase of 26%.

1 Introduction

Conductivities of biological tissues provide useful functional information in many areas clinical applications. Conductivity images are acquired using EIT but limited by poor spatial resolution. The limitation can be overcome by fusing the functional information of EIT with the morphological features of a CT image. Earlier, we demonstrated the potential of fusion by imaging a phantom with radiotherapy bolus as medium [1]. In the present study, we use winter melon based biological phantom. For simplicity we measure conductivity part of the impedance using 2D approach along with an assumption that the winter melon shape is circular.

2 Methods

A cylindrical slice of winter melon was cut from the whole vegetable and a cavity of 4.5 cm diameter was made as shown in Fig. 1.

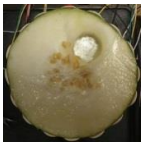

Fig.1. Winter melon Phantom

EIT data was acquired using sixteen electrodes around the phantom, injecting a current of 0.4mA at 66 KHz . Images were reconstructed in differential imaging mode using one-step Gaussian Newton minimization solver [2]. CT image of the melon was obtained using a Phillips CT Scanner. A binary mask image was generated from the CT-image using automatic thresholding. The mask and the EIT images were resized based on the reference electrode position and the CT image dimensions. The mask image was then segmented for different regions of interest and labelled for the user to specify. The region selected by the user was fused with the CT image through logical indexing. The CT, EIT and EIT/CT imaging performance was evaluated using detectability and structural similartity measures. Detectability is measured as

$$D = \frac{\mu_{roi}}{SD_{background}} (1)$$

μ_{roi} is the mean of the ROI pixels and $SD_{background}$ is the standard deviation of the background pixels of the image [3].The structural similarity index is a widely used measure in signal and image processing applications, derived from the visual impact of changes in luminance, contrast and structure in an image [4]. It is calculated as a single metric using

$$SSIM = \frac{(2\mu_x\mu_y+C_1)(2\sigma_{xy}+C_2)}{(\mu_x{}^2+\mu_y{}^2+C_1)(\sigma_x{}^2+\sigma_y{}^2+C_2)} (2)$$

Where, μ_x and σ_x are the mean and standard deviation of the CT image μ_y and σ_y are the mean and standard deviation of the EIT image. σ_{xy} is the Correlation coefficient between the CT and EIT image under assessment and C_1, C_2 are computational constants..

3 Results

Fig. 2 shows the images obtained before and after fusion for the circular inhomogeneity. Detectability and structural similarity evaluations of the CT, EIT and the EIT/CT images, evaluated using (1) and (2) show an increase in structural similarity by 26% along with a detectability increase of 67%.

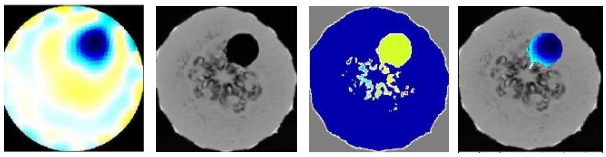

Fig.2. EIT/CT Fusion Imaging of seeded winter melon. From left to right: EIT Image, CT Image, Image with labelled ROIs, and Fused EIT/CT image

4 Conclusions

Imaging winter melon phantom through co-registration and fusion of functional Electrical Impedance Tomography (EIT) and Computed Tomography (CT) improved detectability by 67% and structural similarity by 26%, thereby showing enhanced potential to use in radiation therapy treatment planning.

References

[1] Krishnan K, Liu J, Thomas. S, Kohli K. 55th Annual Meeting & Exhibition, Med. Phys. 2013.

[2] Andy Adler, William R.B. Lionheart . *Physiol. Meas. , 27*, S25-S42, 2006.

[3] Yasheng Maimaitijiang, Stephan Böhm, Obaydah Jaber, Andy Adler, Int. Conf. Electrical Bio-Impedance & Electrical ImpedanceTomography .2010.

[4] Wang Z,Bovik A.C, Sheikh H.R, and Simoncelli E.P" IEEE Trans on Image Processing **13** (4), 600-612,(Apr 2004).

Anomaly depth detection in trans-admittance mammography: a formula independent of anomaly size or admittivity contrast

Tingting Zhang[1], Eunjung Lee[1], Jinkeun Seo[1]
[1]Yonsei University, Seoul, Korea,zttouc@hotmail.com

Abstract: TAM(trans-admittance mammography) aims to determine the location and size of any anomaly from the multi-frequency. A formula is proposed here that can estimate the depth of an anomaly independent of its size and the admittivity contrast. This depth estimation can also be used to derive an estimation of the size of the anomaly. Numerical simulation shows that the proposed method also works well in general settings.

1 Introduction

Bioimpedance techniques such as electrical impedance tomography (EIT) are potential supplemental tools for breast cancer detection [1–5]. This paper considers a TAM system [6, 7] in which the breast is compressed between two electrical plates (see Figure 3). One plate is a large solid voltage driving electrode, and the other is composed of current-sensing point electrodes. The system employs constant sinusoidal voltage at frequencies of 50 Hz-500 kHz. The voltage is applied through the voltage driving electrical plate; a grounded voltage is maintained on the other plate. The voltage difference induces time harmonic electrical current that is determined by the conductivity distribution in the breast. The current-sensing electrodes can be used to measure exit currents to obtain two-dimensional transadmittance maps at multiple frequencies. The corresponding inverse problem is to detect the conductivity anomalies that denote breast tumor tissue from the multiple-frequency trans-admittance maps.

2 Methods

When a sinusoidal voltage $V_0 \sin \omega t$ with an angular frequency $\frac{\omega}{2\pi}$ is applied through Υ(see Figure 3), potential u_ω satisfies:

$$\begin{cases} \nabla \cdot (\gamma_\omega(\mathbf{r}) \nabla u_\omega(\mathbf{r})) = 0, & \mathbf{r} \in \Omega \\ u_\omega(\mathbf{r}) = V_0, & \mathbf{r} \in \Upsilon \\ u_\omega(\mathbf{r}) = 0, & \mathbf{r} \in \Gamma \\ \mathbf{n} \cdot (\gamma_\omega(\mathbf{r}) \nabla u_\omega(\mathbf{r})) = 0, & \mathbf{r} \in \partial\Omega \backslash (\Upsilon \cup \Gamma), \end{cases} \tag{1}$$

where $\gamma_\omega(\mathbf{r}) = \begin{cases} \gamma^n_\omega(\mathbf{r}) := \sigma^n_\omega(\mathbf{r}) + i\omega\varepsilon^n_\omega(\mathbf{r}), & \mathbf{r} \in \Omega \backslash \overline{D} \\ \gamma^a_\omega(\mathbf{r}) := \sigma^a_\omega(\mathbf{r}) + i\omega\varepsilon^a_\omega(\mathbf{r}), & \mathbf{r} \in D \end{cases}$.

Theorem 2.1 *Let $g_{\omega_j} = -(\sigma_{\omega_j} + i\omega_j\varepsilon_{\omega_j})\frac{\partial u_{\omega_j}}{\partial \mathbf{n}}$ be the measured Neumann data at frequency ω_j for $j = 1,2$ and let $\alpha = \gamma^n_{\omega_1}/\gamma^n_{\omega_2}$. Then we have depth formula:*

$$z_D = 2\sqrt{3}\left|\frac{(g_{\omega_1} - \alpha g_{\omega_2})(\mathbf{r}^*)}{(\partial_x^2 + \partial_y^2)(g_{\omega_1} - \alpha g_{\omega_2})(\mathbf{r}^*)}\right|^{\frac{1}{2}} \left|\frac{1 + r_1(\mathbf{r}^*)}{1 + r_2(\mathbf{r}^*)}\right|^{\frac{1}{2}}, \tag{2}$$

where C_{k1}, C_{k2} are depending only on $\rho, \delta, d_0/V_0, |D|, |\Omega|, \gamma^n_{\omega_1}$, $\gamma^a_{\omega_1}, \gamma^n_{\omega_2}$ and $\gamma^a_{\omega_2}$, $\mathbf{r}^* = (x_D, y_D)$ and u_0 is the solution of (1) in the absence of anomaly.

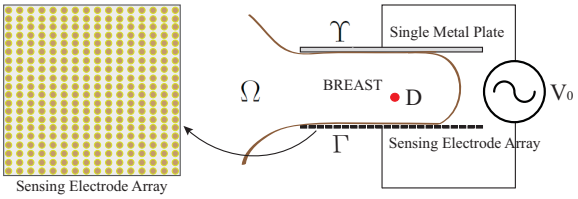

Figure 1: Trans-admittance mammography (TAM). (L): the sensor electrode array. (R):Schematic cross-section

Observation 2.2 *Under the same assumption given in theorem 2.1, we define a connected set S containing $(x_D, y_D, 0)$ such that*

$$S := \{\, (x,y,0) \in \Gamma : \nabla^2_{xy} G(x,y) \cdot \nabla^2_{xy} G(x_D, y_D) > 0 \,\}, \tag{3}$$

where $\nabla^2_{xy} = \partial_x^2 + \partial_y^2$ and $G(x,y) = [Real(g_{\omega_1} - \alpha g_{\omega_2})](\mathbf{r}), \mathbf{r} \in \Gamma$. Then we have

(1) the set S is independent on the size of anomaly D and the admittivity contrast

(2) depth z_D can be determined by $z_D \approx 1.6938 \cdot$ (the radius of S).

3 Numerical simulations

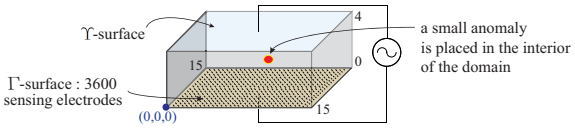

Figure 2: Numerical simulation domain

depth	z_D (theorem 2.1)	z_D (observation 2.2)
0.5 cm	0.87	0.63
1 cm	1.17	1.08
1.5 cm	1.61	1.55
2 cm	2.12	2.04

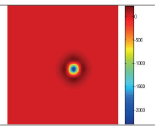

Figure 3: Anomaly depth estimated by using theorem 2.1 and observation 2.2

4 Conclusions

Throughout this paper, we gave a rigorous mathematical analysis for the proposed algorithms to estimate the size and position of anomaly and presented a successful numerical simulation results supporting the theories. In the future, we plan to make use of the suggested algorithm in experiments.

References

[1] Assenheimer M, Moskovitz O, Malonek D, et al. *Physiological Measurement* **22**:1–8, 2001
[2] Mueller JL, Isaacson D, Newell JC. *IEEE Trans BiomedEngrg* **46**:1379–1386, 1999
[3] Cherepenin V, Karpov A, Korjenevsky A, et al. *Physiol Meas* **22**:9–18, 2001
[4] Kim S, Lee J, Seo JK, et al. *SIAM J Appl Math* **69**:22–36, 2008
[5] Ammari H, Kwon O, Seo JK, et al. *SIAM J Appl Math* **65**:252–266, 2004
[6] Zhao MK, Liu Q, Woo EJ, et al. In *J. Phys.: Conf. Ser.* 2010
[7] Zhao MK, Wi H, Kamal AHM, et al. *BioMedical Engineering Online* **11**:751, 2012

A feasibility study for High Resolution EIT imaging

Wei Wang[1], Gerald Sze[1], Xiaolin Zhang[1] and David Barber[2]

[1]Micro Image UK Ltd, Cambridgeshire, UK w97wang@yahoo.co.uk

[2]University of Sheffield, Sheffield UK

Abstract: EIT is a new imaging technology that is open to many applications with its advanced natures with no ionising radiation, relatively low cost. The main disadvantage of EIT is the low spatial resolution that limits its application areas. This paper presents a new methodology that has achieved a significant improvement of the spatial resolution, enabling "high resolution" EIT imaging.

1 Introduction

The Electrical Impedance Mammography (EIM) is a 3D EIT based system for breast cancer detection. The ability to detect a suspicious lesion of less than 20mm in diameter and down to pathological Grade-1 is clinically very advantageous. Being able to do so is a current major challenge of the EIM technology. This study proposes a new novelty method to have increased the spatial resolution of EIM for meeting the clinical requirement.

2 Methods

Cambridge EIM systems have been designed to use either 85 or 89 planar electrodes deployed in hexagonal and squared pattern respectively (Fig. 1a,1c). The distance between the adjacent electrodes is 17mm. The current excitation and voltage measurements are achieved in a small hexagonal area (Fig.1 b) with up to 1416 measurements made [1] at each frequency. In all illustrations in this paper, the yellow dots indicate the excitation pair electrodes while blue dots connected by red arrows indicate measuring pairs of electrodes..

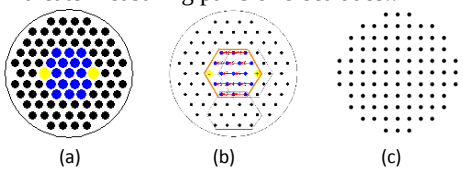

Fig 1. The planar electrodes system of Cambridge EIM (a) the hexagonal electrodes. (b) the electrode drive and receive hexagon.(c) squared based electrode configuration

The concept of this novelty method is to reconstruct an high-resolution (HR) image, based on obtaining very HR frames data, to be achieved by shifting the electrode plate of the scan-head via a group of digital stepper motors, where the planar electrodes are implanted into any option proposed (Fig 2,3). All measurement frames are combined together as one set of data and processed by the image reconstruction algorithm on an HR mesh. To avoid moving artefact during multi-frame shifting data collection, patient breast is held by a rigid holder on the top of the electrode planar in the tank, which is made of a matched conductivity materials. The following figures relating to 3 options as examples to show how to achieve an HR EIT images, based on "squared-shaped electrode" configuration. As shown in Fig 2-3, each movement is represented by an arrow, Fig 2 represents 4 shifted frames resulting one HR "virtual" electrode arrays (Fig 2 (right)).

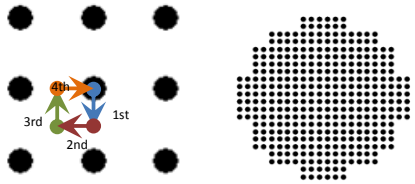

Fig 2. Option 1: Electrodes array with 4-shift HR frames with 1 interpolation, to achieve the combined numbers of all the electrodes: 89*4 = 356 (right)

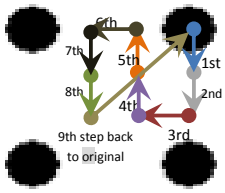

Fig 3. Option 2,3 and Option N: Electrodes with 9 or 16-shift HR frames (2 or 3-interpolation) will achieve total 801 or 1424 combined virtual electrodes respectively. Similarly, electrodes with N-interpolation would generate $(N+1)^2$ shifting to achieve total $(N+1)^2$ x89 combined electrode effect.

The preliminary results of HR image is shown in Fig 4.

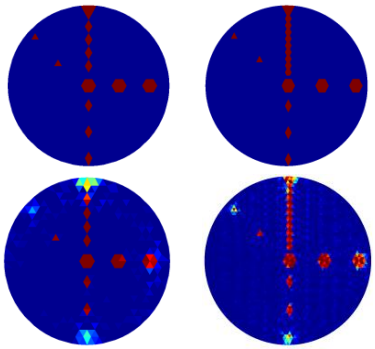

Fig 4. Result of 85-electrode EIM simulation. Original model: hexagonal mesh (top left) and 4-shit based HREIM mesh (top right). The results of reconstructed noise-free images: hexagonal mesh (bottom left) and the HREIM mesh (bottom right)

3 Conclusions

The preliminary results have shown that the HR EIT is feasible and significant improvement has been made.

References

[1] Xiaolin Zhang, Wei Wang and Chris Chatwin, "The Data Acquisition Method of the Sussex MK4 EIM System", EIT2014 conference, Canada 2014

Author Index